Computational Analysis of Energy Exchange Mechanisms in Turbulent Flows with Thermal Nonequilibrium

A THESIS
SUBMITTED TO THE FACULTY OF THE GRADUATE SCHOOL
OF THE UNIVERSITY OF MINNESOTA
BY

Aaron George Neville

IN PARTIAL FULFILLMENT OF THE REQUIREMENTS
FOR THE DEGREE OF
Doctor of Philosophy

Graham V. Candler

January, 2018

Acknowledgements

Quite simply put, this work would not have been possible without the support from I've been given from some incredible individuals. That they have given me such support and time is truly amazing. First and foremost, I want to thank my advisor Professor Graham Candler, whose support, encouragement, and patience never faltered, and who made graduate school a success for me. The knowledge and wisdom he has shared in a wide variety of areas within the hypersonic field is truly astounding. Additionally, I would like to thank the entire Candler research group for sharing knowledge, experience, and fun throughout the years. Several people deserve more credit than I can give them here. Dr. Ioannis Nompelis has been a great help from the very beginning, from explaining molecular dynamics using keyboards and oranges, to helping my understanding of numerical techniques, and assisting with some of the post-processing tools used in this work. Dr. Pramod Subbareddy has also been a great mentor, helping me understand the numerical requirements of these simulations, and advancing my knowlege of turbulent flows. Additionally, Dr. Ross Wagnild provided a great resource for my questions on acoustic damping, and Ross Chaudhry provided helpful advice on US3D and on analysis of these flows. Dr. Anand Khartha and Siddarth GS served as great resources on turbulent flows, and always had excellent suggestions during brainstorming sessions.

Dr. Alan Schwing and Major Jeffrey Komives have been great colleagues and friends, providing ideas and inspiration, and keeping me grounded with perspective. I would also like to thank: Dr. Sriram Doraiswamy, Dr. Travis Drayna, Dr. Heath Johnson, Dr. Dave Peterson, Dr. Erik Tylzcak, Dr. Eric Stern, Dr. Joe Brock, Dr. Pietro Fererro, Steph Jenson, and Lindsay Kirk. Without your support, encouragement, dedication to success, and friendship, none of this would have been possible. To the current members

of the research group, I thank you for your support as I finished this work, and I wish you all good luck with your research and in the future.

Finally, I must thank my family: Julie, Gerry, Tyler, and Jayce for providing me with a platform to succeed upon, and always believing in me. My wife Christina has always thought better of me than I deserve, and without her patience and support, and listening to more aerospace talk than she ever thought possible, this would not have come to fruition. I also want to thank my extended family for always supporting me and being there whenever I needed.

And to you, reader, for taking interest in my work, thank you. I hope you find inspiration and useful knowledge contained within.

This work was sponsored by the Air Force Office of Scientific Research under grants FA9550-12-1-0064 and FA9550-12-1-0461. The views and conclusions contained herein are those of the author and should not be interpreted as necessarily representing the official policies or endorsements, either expressed or implied, of the AFOSR or the U.S. Government.

Dedication

For Christina, my parents, the past, and to the future

Abstract

The design of hypersonic vehicles is significantly affected by the state of boundary layer. Hypersonic boundary layers can be laminar or turbulent, and in chemical and vibrational nonequilibrium, each with different length and time scales. In turbulent boundary layers, heating augmentation can be an order of magnitude or higher above laminar heating rates. The scales of the internal energy relaxation processes can be of the same order or greater than the turbulent flow scales, and can interact with turbulent motion. Understanding how turbulent motion and internal energy relaxation interact is relevant to flow control.

Fundamental flows are studied to understand how energy is exchanged between turbulent motion and internal energy relaxation. Specifically, high-fidelity DNS of vibrational energy relaxation effects in compressible isotropic and temporally evolving shear layers are presented. The energy exchange mechanisms are analyzed by decomposing the flow into incompressible and compressible energy modes. By varying the vibrational relaxation rate, the tuning of the relaxation rate to the turbulent flow is studied.

Vibrational energy relaxation is demonstrated to be coupled to the turbulent flow through the compressible modes of the gas. Compressions and expansions generate fluctuations in the thermal state, and the vibrational energy lags behind these fluctuations. Energy is then transferred to or from the vibrational energy mode at a rate proportional to the relaxation time, and the fluctuations are damped. Damping of turbulent quantities are strongest when the vibrational relaxation rate is on the order of the turbulent large structure acoustic rate. Wavenumber specific damping is also observed in isotropic flows when the relaxation time is on the order of the acoustic frequency of the wave. The effects of vibrational relaxation are shown to increase with compressibility. However, the overall effect on turbulent kinetic energy is weak due to the incompressible mode containing significantly more energy than the compressible modes.

Contents

List of Tables

List of Figures

Chapter 1

Introduction

Maintaining a laminar boundary layer along the surface of a hypersonic flight vehicle can have significant impacts on the design and operation of the vehicle. As the boundary layer transitions from a laminar state to a fully turbulent state, the heating rates to the surface of the vehicle increase. Turbulent boundary layers can have heating levels that far exceed the laminar heating rates at similar flow conditions. The turbulent heating augmentation can be as high as an order of magnitude or more above laminar heating rates[2]. Turbulence may amplify or decay within a boundary layer that is formed on a vehicle's surface. Many factors contribute to the potential enhancement or decay of turbulent motion, and these may be environmental or may be intrinsic to the flow physics.

In high enthalpy flow environments typically seen by hypersonic flight vehicles, physical processes are triggered by elevated temperatures. Relevant examples of these physical processes include dissociation and recombination reactions as well as vibrational energy relaxation. As the temperature increases, these internal energy modes are excited, and a broader distribution of energies is available to the gas. These internal energy processes release or absorb energy and interact with turbulent motion[4]. The turbulent motion within a boundary layer span a broad range of length and time scales, while the internal energy modes have their own range of scales. While energy relaxation is a collisional process occurring on a molecular scale, the equilibration of energy between modes can occur on time scales which are similar to or greater than the scales of the flow. This means that energy relaxation is not a scale independent process. Turbulent

motion transports energy across the boundary layer while also exchanging energy with internal energy modes. The impact of these energy dynamics on the enhancement or decay of turbulent motion is not well understood.

An example of a flight environment with both turbulent flow and internal energy relaxation is entry of a vehicle into an atmosphere, such as the Space Shuttle reentering the Earth atmosphere, or capsules entering the Martian atmosphere. Figure 1.1 shows a thermal image taken during reentry of the STS-119 orbiter as part of the HYTHIRM experiment[1]. In this experiment, a small protuberance was placed in the thermal protection system (TPS) to study the effects of transition and turbulence on the boundary layer. Thermal images were then obtained by a low-flying plane. In addition to the small protuberance, the boundary layer transitioned to a turbulent state from an unknown source near the nose of the vehicle. These turbulent boundary layers are clearly visible in the image, demonstrated by the yellow/green and red regions. The surface of the vehicle is almost entirely covered by this turbulent region.

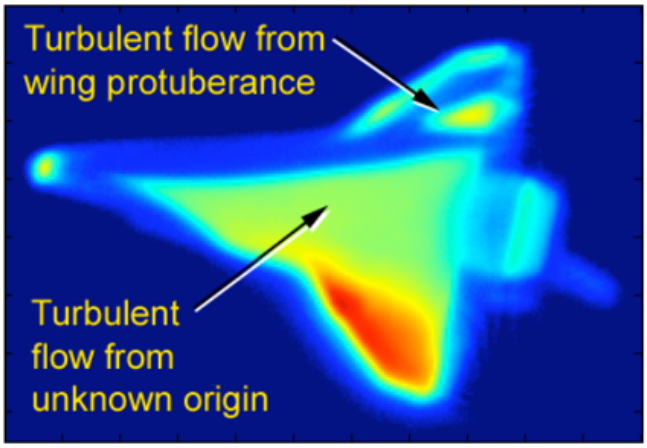

Figure 1.1: Thermal image of STS-119 from HYTHIRM experiment; the turbulent boundary layer is clearly visible in the non-blue regions[1]. Contour colors correspond to regions of increased heat flux, indicating turbulence. Image was taken with orbiter at an altitude of 49 km and $M = 8.4$ ($V = 2772$ m/s).

The image from the HYTHIRM experiment was taken at an altitude of 49 km and a Mach number of 8.4. Figure 1.2 shows the flight corridor of a typical orbiter reentry

as a function of altitude and velocity. Also shown are regions where relevant internal energy excitation begin (energy excitation does not stop in the regions to the right, but continue to exchange energy as other internal energies are excited). The location the HYTHIRM image was taken is indicated with a circle in Fig. 1.2, and is observed to be in a region of significant vibrational excitation, with oxygen dissociation also likely.

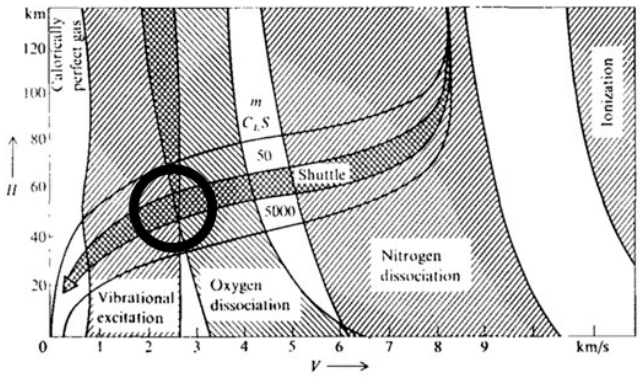

Figure 1.2: Trajectory corridor of orbiter through altitude and velocity showing regions of relevant energy excitation[2]. The circle indicates the region where imagery of STS-119 was taken[1]. Note that in regions to the right of the highlighted excitation mode, the availability of the mode to the gas does not cease, but continues to exchange energy as other mechanisms become important.

Interaction of turbulent flow fields and internal energy excitation, observed in the HYTHIRM experiment, can have significant consequences on vehicle design. Figure 1.3 compares the heat flux obtained from simulations of a spherical capsule at angle of attack in laminar and turbulent environments, where internal energy processes are excited. The stagnation region is located in the region of low heat flux near the top of the left (turbulent) capsule image. The heat flux on the surface of the capsule is significantly increased for the turbulent case compared to the laminar case. These simulations use an 11-species gas model of the Martian environment, with significant catalysis effects near the wall. The boundary layer is in nonequilibrium for both chemical and vibrational energies. The significant increase in heating for the turbulent boundary layer has severe consequences for the design of the TPS. Often, these systems are designed with much thicker materials than are actually needed, resulting in decreased payload size.

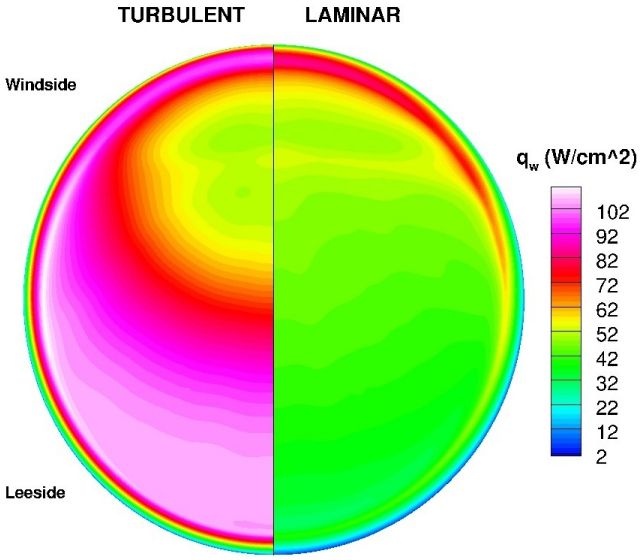

Figure 1.3: Spherical "Apollo-like" capsule in CO_2 dominated Martian atmosphere comparing heat flux. Image on the left is from a turbulent simulation, while the right image is laminar. The wall has catalysis and heating effects, and vibrational and chemical processes are excited.

Understanding how turbulent flows interact with internal energies is relevant to flow control. One potential example is designing a TPS to actively or passively alter the thermal environment of the boundary layer. Gas injection can potentially be used to alter the relaxation rates of the internal energies, such that the turbulent effects are reduced. Alternatively, flight trajectories could potentially be altered to flight environments which tune the relaxation processes to the turbulent flow. Several potential flow control mechanisms could be designed to modify the turbulence through internal energy relaxation, but these are beyond the scope of this work and are not discussed further.

Transition studies have demonstrated a reduction in acoustic waves by internal energy relaxation[5, 6, 7, 8]. The strongest effects were observed for waves propagating through CO_2. Gas injection has also been moderately successful in damping these waves, resulting in delayed transition of a hypersonic boundary layer[6]. However, gas injection is difficult to achieve, as the injected fluid can cause the boundary layer to transition if

not done carefully.

Turbulent flows, however, contain and broad range of length and time scales, with energies contained over a spectrum of frequencies. Understanding how energy is exchanged over these broadband scales between turbulent flow and internal energies is the focus of this work. This understanding can then be used to study how relaxation processes can be tuned to a turbulent flow. Tuning of the relaxation and turbulent scales occurs when turbulent fluctuations are optimally damped.

Few studies examining the relationship between turbulence and thermal non-equilibrium have been carried out. Osipov et al.[9] numerically studied a von Karman vortex street in significant thermal nonequilibrium and found evidence that vibrational relaxation has an effect on the structure of vorticity. The initial vibrational temperature was set to a significantly higher value than the translational-rotational temperature, meaning energy was transferred into the translational-rotational mode from the vibrational mode. In the slower moving fluid contained within the vortex street, more energy was deposited into the translational-rotational mode compared to the surrounding faster moving fluid, increasing the heating of the fluid within the street. This decreased the density of the fluid, and resulted in damped vortices. Donzis and Maqui[10] performed a more fundamental study by simulating vibrational energy relaxation in forced isotropic turbulence. They found that more energy is stored in the vibrational mode for turbulent flows than for laminar flows. Additionally, they showed that these effects were strongest for low excitation levels.

Martin and Candler[4] studied reactions in isotropic turbulence. They found that the incompressible energy modes were unaffected by the reactions, while the compressible energy modes were affected. Specifically, the compressible energy modes were enhanced by exothermic reactions and damped by endothermic reactions. The reactions generate fluctuations in the thermal state, resulting in fluctuations in pressure and acoustic waves. Martin and Candler showed that the kinetic energy was affected by acoustic waves through the pressure-strain term in the kinetic energy equation. Dissociation is an endothermic reaction, which absorbs energy, and takes energy away from the turbulent motion, while the reverse is true for recombination, which is an exothermic reaction. Duan and Martin[11, 12, 13] extended this study to reacting hypersonic boundary layers. They found that recombination reactions enhance turbulence, while the dissociation

reactions have a dampening effect. However, the reactions had no meaningful effect on the turbulent kinetic energy, or most other turbulent quantities. This was attributed to the low levels of heat release compared to the flow enthalpy. The tuning of the reaction time scales to time scales of the turbulent flow, such that turbulent fluctuations are optimally damped, was not considered in these works.

Experimental studies focusing on the interaction between relaxation processes and turbulent motion are scarce, partly due to the many challenges involved in performing such experiments. An experimental facility at Texas A&M University uses a capacitively-coupled radio-frequency plasma discharge to achieve vibrational non-equilibrium in a turbulent flow[14, 15]. The flow is passed through a passive grid, generating a decaying turbulent flow field. After the flow passes through the grid, the plasma discharge is used to increase the vibrational energy content of the N_2 molecules in the turbulent flow, while the translation-rotational energy remained the same and O_2 was mostly unaffected. The plasma discharge also increased the wall heating directly behind the discharge nodes, resulting in a thickening of the boundary layer and flow acceleration. Fuller et al.[16] report a clear coupling between vibrational non-equilibrium and turbulent transport. They observed reductions in the Reynolds stresses of approximately 15% for the lower plasma setting, and 30% for the higher plasma setting. This resulted in increased stabilization of the turbulent flow with vibrational nonequilibrium.

1.1 Scope of the Current Work

In previous studies, internal energy relaxation has been shown to damp acoustic waves and delay transition, both experimentally and computationally[17, 18, 6]. These studies have also demonstrated that an optimal damping point exists when the frequency of the wave is on the order of the inverse relaxation time[3, 19, 7]. However, the effects of internal energy relaxation in turbulent flows, and how relaxation scales tune to turbulent scales for optimal damping has not been fully quantified. Understanding the interaction of transitional and turbulent flows is relevant to flow control. The purpose of this work is to gain a fundamental understanding of how energy is exchanged between turbulent motion and internal energy.

Hypersonic boundary layer simulations with chemical and vibrational nonequilibrium effects have complex flow physics, and understanding the interaction between physical processes can be difficult to determine. Isolating these interactions, and varying the defining parameters to understand how the scales relate can be extremely difficult and prohibitively expensive. For these reasons, we study fundamental turbulent flows where parameters are more easily defined, and effects can be isolated. In addition, we limit the internal energy relaxation processes to vibrational energy relaxation. Chemical reactions have time scales which can be an order of magnitude larger than vibrational. Vibrational energy relaxation effects are therefore more relevant to boundary layer flows. The vibrational energy controlling parameters are also easier to vary and isolate effects.

Direct numerical simulations (DNS) of two fundamental turbulent flows with vibrational energy relaxation are studied: compressible isotropic turbulence and temporally evolving turbulent shear flow. The US3D[20] flow solver is used to obtain these high-fidelity turbulent flow simulations. Compressible isotropic turbulence is commonly used for understanding fundamental flow physics, and the defining parameters are easily varied to understand how turbulent and vibrational relaxation scales relate. The first objective of this study is to understand the physical energy exchange mechanisms between vibrational and kinetic energy modes. We then vary the vibrational relaxation time to examine how the turbulent motion and relaxation scales relate, or how the vibrational relaxation rate tunes to the turbulent motion such that fluctuations are damped. This relation of time scales has, to our knowledge, not been fully quantified in previous studies. Energy exchange mechanisms are then examined in greater detail by decomposing the velocity field into compressible and incompressible components. This allows us to examine how vibrational energy relaxation interacts with turbulence at different scales.

The conclusions gained from compressible isotropic turbulence are then generalized to a more complex turbulent shear flow. In isotropic turbulence, the turbulent fluctuations decay to zero, and length and time scales are independent of direction. Turbulent shear flows are more complex than isotropic flows, with direction-dependent scales and vorticity generation, but are still not as complicated as boundary layers. The results from these simulations are compared and contrasted with the results from the isotropic turbulent simulations. In both sets of flows, the effect of compressibility is studied

by varying the relevant Mach number. A vibrational Damköhler number relating the vibrational relaxation time to a turbulent time scale is defined in both cases as well.

In Chapter 2, the governing equations, including assumptions and models, are presented. We then describe the numerical techniques used to solve the governing equations in Chapter 3. The Navier-Stokes equations for a one-species continuum flow in vibrational nonequilibrium are solved with a finite-volume formulation. High-order numerics are used and all length and time scales are resolved; no turbulence models are included.

Chapter 4 contains a discussion on theoretical and computational absorption of acoustic waves by internal energy relaxation. This discussion provides a foundation on which the results from the isotropic and shear simulations are interpreted. A computational framework for propagation of acoustic waves is described, and results are presented showing how acoustic waves are damped by vibrational energy relaxation. This framework is used in later chapters to interpret results and quantify numerical stability requirements.

Chapters 5 and 6 contain the results for compressible isotropic turbulence and temporally evolving shear layers with vibrational energy relaxation, respectively. DNS simulations are described, and numerical requirements are discussed. In both chapters, the energy exchange mechanisms are discussed first by examining the effects of vibrational energy relaxation in the given flow. The vibrational Damköhler number is then varied to understand how the vibrational relaxation time tunes to a turbulent time scale, and what the relevant turbulent time scale is. Compressibility effects are studied, and the conclusions from each flow are compared.

Chapter 2

Governing Equations

The set of governing equations used to simulate the fluid flows studied in this work are outlined in this chapter. The equation set uses a one-species formulation, with a finite-rate conservation equation for vibrational energy relaxation. We assumed a thermally perfect fluid in continuum, such that the ideal gas law is obeyed. The specific heats of the gas contain a vibrational energy component, and are functions of temperature, precluding the assumption of a calorically perfect gas.

For high enthalpy flows, internal energy modelling is required as mode excitation increases the available energy distribution. The energy contained in the translational mode is reduced through molecular collisions which transfer energy to internal modes. These internal modes include rotational, vibrational, and chemical energy. Rotational energy typically equilibrates with translational energy in approximately ten collisions, whereas vibrational energy requires around 2000 collisions. The rotational and translational modes are assumed to be in equilibrium and represented by a single temperature due to this relatively small number of collisions. Chemical reactions, not considered in this work, often require an order of magnitude or more collisions to achieve equilibrium.

2.1 Conservation Equations

Unless otherwise noted, summation notation is used in the conservation equations below. The conservation of mass is

$$\frac{\partial \rho}{\partial t} + \frac{\partial}{\partial x_i}(\rho u_i) = 0, \tag{2.1}$$

where ρ is the density and u_i is the flow velocity. The conservation of momentum is given by

$$\frac{\partial \rho u_i}{\partial t} + \frac{\partial}{\partial x_j}(\rho u_i u_j) = -\frac{\partial p}{\partial x_i} + \frac{\partial \tau_{ij}}{\partial x_j}, \tag{2.2}$$

where p is the pressure of the fluid, and τ_{ij} is the viscous stress tensor. Body forces are assumed to be negligible.

Energy exchange between vibrational modes is assumed to occur sufficiently fast so that all vibrational modes are in equilibrium. This allows for the vibrational energy to be described by a single temperature, T_v, and a single conservation equation rather than separate equations for each mode. The conservation of total vibrational energy per unit volume is

$$\frac{\partial E_v}{\partial t} + \frac{\partial}{\partial x_i}(u_i E_v) = -\frac{\partial q_{v,i}}{\partial x_i} + w_v, \tag{2.3}$$

where $q_{v,i}$ is the vibrational heat flux in direction i, and w_v governs the transfer of energy between translation-rotational and vibrational energy. These terms are discussed in the next section.

The final conservation equation is for total energy per unit volume:

$$\frac{\partial E}{\partial t} + \frac{\partial}{\partial x_i}(u_i(E+p)) = \frac{\partial u_i \tau_{ij}}{\partial x_j} - \frac{\partial q_i}{\partial x_i} - \frac{\partial q_{v,i}}{\partial x_i}, \tag{2.4}$$

where q_i is the translation-rotational heat flux in direction i. A state equation is used to close the above equation set, and models or constitutive relations are required for several terms. These are the topic of the next section.

2.2 Equations of State and Constitutive Relations

The thermodynamic variables are related using the ideal gas law, thereby closing the equation set described in the previous section.

$$p = \rho \frac{R}{M} T \tag{2.5}$$

In this equation, R is the universal gas constant and M is the molecular weight of the species.

The total energy per unit volume is the sum all available energy pools.

$$E = \frac{1}{2}\rho u_i u_i + \rho c_v T + E_v + \rho h^\circ \tag{2.6}$$

The first term on the right of the above equation is the bulk kinetic energy of the gas. The second term is the translational-rotational energy, where c_v is the translational-rotational specific heat at constant volume. This specific heat is constructed using contributions from translational and rotational modes as

$$c_v = c_v^{(tr)} + c_v^{(rot)}, \tag{2.7}$$

with each component defined as

$$c_v^{(tr)} = \frac{3}{2}\frac{R}{M}, \tag{2.8}$$

$$c_v^{(rot)} = \frac{R}{M}. \tag{2.9}$$

The rotational specific heat formulation is defined assuming a linear molecule, such as CO_2. The enthalpy per unit mass is defined as

$$h = \rho c_v T + \frac{p}{\rho} + e_v = c_p T + e_v, \tag{2.10}$$

where c_p is the translational-rotational specific heat at constant pressure.

The third and final contribution to the total energy in Eq. 2.6 is the vibrational energy of the gas. Assuming a Boltzmann distribution of vibrational states, the simple

harmonic oscillator model is used to define the vibrational energy per unit mass.

$$e_v = \frac{R}{M} \sum_{m=1}^{nvm} \frac{\theta_{v,m}}{\exp(\theta_{v,m}/T_v) - 1} \tag{2.11}$$

In the above equation, $\theta_{v,m}$ is the characteristic vibrational temperature of mode m, and nvm is the number of vibrational modes of the gas. Specific values of $\theta_{v,m}$ are given in Appendix D. In general, this equation is not directly solvable for T_v for polyatomic molecules (e.g. CO_2 has four modes of vibration), and therefore iterative methods must be used.

The viscous stress tensor is given by

$$\tau_{ij} = \mu \left(\frac{\partial u_i}{\partial x_j} + \frac{\partial u_j}{\partial x_i} \right) + \lambda \frac{\partial u_k}{\partial x_k} \delta_{ij}, \tag{2.12}$$

where μ is the dynamic viscosity, λ is given below, and a Newtonian fluid has been assumed. The gas used in this work is at low enough density where the effect of intermolecular forces for non-colliding particles is negligible. Stokes hypothesis for bulk viscosity is therefore applied as,

$$2\mu + 3\lambda = 0, \tag{2.13}$$

and the bulk viscosity is zero.

Fourier's law is used to define the heat flux vectors,

$$q_i = -\kappa \frac{\partial T}{\partial x_i} = -(\kappa_{tr} + \kappa_{rot}) \frac{\partial T}{\partial x_i}, \tag{2.14}$$

$$q_{v,i} = -\kappa_v \frac{\partial T_v}{\partial x_i}, \tag{2.15}$$

where κ_i is the thermal conductivity for energy mode i (translational, rotational, or vibrational). The thermal conductivities are calculated for each mode using Eucken's relation[19].

$$\kappa_{tr} = \frac{5}{2} \mu c_v^{(tr)}, \qquad \kappa_{rot} = \mu c_v^{(rot)}, \qquad \kappa_v = \mu c_{vv} \tag{2.16}$$

The vibrational specific heat at constant volume is computed directly from definition.

$$c_v^{(vib)} = \frac{\partial e_v}{\partial T_v} \tag{2.17}$$

The viscosity is computed using the curve fit model given by Blottner[21]. The curve fits are given as a function of temperature, and are valid up to approximately 10,000 K.

$$\mu = 0.1 \exp((A \ln T + B) \ln T + C) \quad \text{kg/(m s)} \tag{2.18}$$

The constants A, B, and C have units of are given in the appendix.

2.3 Vibrational Energy Source Term

The last term on the right hand side of Eq. 2.3, w_v, represents the exchange of energy between translational-rotational and vibrational energy modes. Vibration-vibration energy exchanges are assumed to be very fast, such that all vibrational modes are in equilibrium. Energy exchanges are represented by a single energy exchange rate. The Landau-Teller model[22] is used to calculate the translational-vibrational energy exchange rate of mode m,

$$Q_{t-v,m} = \rho \frac{e^*_{v,m}(T) - e_{v,m}(T_v)}{\tau_m}, \tag{2.19}$$

where $e^*_{v,m}(T)$ is the local equilibrium vibrational energy, evaluated using the translation-rotational temperature, and τ_m is the relaxation time for the given vibrational mode. In the above equation, the rate of energy exchange is given by a measure of how far the vibrational mode is from equilibrium, and is driven towards equilibrium by the relaxation rate. The total exchange rate is then the sum of the contribution from each vibrational mode.

$$w_v = \sum_{m=1}^{nvm} Q_{t-v,m} \tag{2.20}$$

The relaxation time is determined using Millikan and White's semi-empirical curve fits[23].

$$\tau_m = \frac{1}{P} \exp[A_m(T^{-1/3} - B_m) - 18.42], \qquad (P \text{ in atm}) \tag{2.21}$$

In this equation, pressure has units of atmospheres and τ_m has units of seconds. The constants, A_m and B_m, are determined by

$$A_m = 1.16\times10^{-3}\mu_m^{1/2}\theta_{v,m}^{4/3}, \qquad B_m = 0.015\mu_m^{1/4}, \tag{2.22}$$

where μ_m is the reduced mass of the collision partner. In general, the reduced mass is given as

$$\mu_{ms} = \frac{M_m M_s}{M_m + M_s}, \tag{2.23}$$

where M_m is the molecular weight of the species with mode m, and M_s is the molecular weight of the collision partner. For single species flows, this reduces to $\mu = M/2$. These constants are sometimes modified for certain species interactions using empirical corrections[24, 25]. In particular, CO_2 relaxation uses the constants determined from Camac[25], and are given in Appendix D.

2.4 Energy Transfer

The total energy, given by Eq. 2.6, is comprised of the available energy pools (modes) of the gas. In this work, the energy is distributed over kinetic, translational-rotational, and vibrational energy pools. Governing equations can be derived for each energy mode and used to examine the flow of energy. The governing equation for kinetic energy, $E_k = \rho(u_i u_i)/2$, is obtained by multiplying the momentum equation with velocity (u_i·Eq. 2.2). An equation for translation-rotational energy, $E_{int} = \rho c_v T$, is obtained by subtracting the kinetic energy and vibrational energy equations from the governing equation for total energy. The equations for kinetic, translational-rotational, and vibrational energies are given, respectively, as

$$\frac{\partial E_k}{\partial t} + \frac{\partial}{\partial x_i}(u_i E_k) = -u_i\frac{\partial p}{\partial x_i} + u_i\frac{\partial \tau_{ij}}{x_j}, \tag{2.24}$$

$$\frac{\partial E_{int}}{\partial t} + \frac{\partial}{\partial x_i}(u_i E_{int}) = -p\frac{\partial u_i}{\partial x_i} + \tau_{ij}\frac{\partial u_i}{x_j} - w_v, \tag{2.25}$$

$$\frac{\partial E_v}{\partial t} + \frac{\partial}{\partial x_i}(u_i E_v) = -\frac{\partial q_{v,i}}{\partial x_i} + w_v. \tag{2.26}$$

Acoustic (inviscid) energy exchanges between kinetic and translational-rotational pools occur through imbalances in pressure and compressions or expansions in the gas. These are represented by the first terms in Eq. 2.24 and 2.25, respectively. Energy is exchanged through the source term w_v between translational-rotational and vibrational energy pools. As seen in the above equations, there is no direct mechanism of energy transfer between kinetic and vibrational pools; energy must first go through the translational-rotational energy pool and effects are second order. The flow of energy between the three pools is summarized in Fig. 2.1.

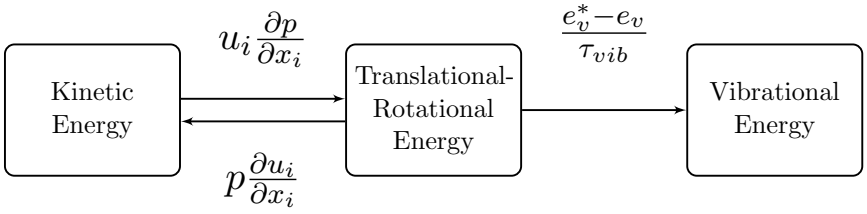

Figure 2.1: Flow of energy between kinetic, translational-rotational, and vibrational energy pools. Arrows show direction of positive energy transfer.

Chapter 3

Numerical Methods

The governing equations presented in the previous chapter are solved using a three-dimensional finite-volume framework. The flow solver used in this work is US3D[20]. US3D is a highly scalable parallel unstructured finite-volume code for solution of compressible gas flows in thermal and chemical non-equilibrium, although not all of these capabilities are used in this work. The basic fundamentals of the numerical solution to the governing equations is given below.

Direct numerical simulations (DNS) are used for all results obtained within this work. The basic principle of DNS is that all length and time scales are resolved. Timestep requirements are discussed at the end of the chapter, and grid convergence is presented in the following chapters. No additional models to the set of equations described in the previous chapter are used in these simulations.

3.1 Finite Volume Formulation

The weak form of the governing equations is discretized using the finite-volume method. The equations are written in terms of a vector of conserved variables, U, and in conservation form are given by

$$\frac{\partial U}{\partial t} + \frac{\partial F_i}{\partial x_i} = W, \tag{3.1}$$

where the vector of conserved variables is

$$U = (\rho, \rho u, \rho v, \rho w, E_v, E)^T. \tag{3.2}$$

F_i is the flux vector in direction i, and W is the source vector.

$$W = (0, 0, 0, 0, w_v, 0)^T \tag{3.3}$$

Integrating Eq. 3.1 over an arbitrary volume, V, and boundary, ∂V, and applying the Divergence theorem to transform the volume integral to a surface integral, we get

$$\frac{\partial \overline{U}}{\partial t} + \frac{1}{V} \oint_{\partial V} (F_i \hat{n_i})\, dS = \overline{W}, \tag{3.4}$$

where $\overline{U}$ and $\overline{W}$ are averaged quantities within the arbitrary volume, $\hat{n}$ is the outward-pointing normal to the surface, and S is the surface area. The arbitrary volume can be approximated as a polyhedral element with planar faces, resulting in the semi-discrete finite-volume expression of the conservation laws.

$$\frac{\partial \overline{U}}{\partial t} + \frac{1}{V_i} \sum_{faces} (F_i \hat{n_i})\, S_i = \overline{W} \tag{3.5}$$

The flow domain of interest is discretized with polyhedral elements, and the rate of change of state of the conserved variables is given by the sum of fluxes over each element face and the source vector. The conserved variables are stored at the centroid of each element.

3.2 Spatial Fluxes

The calculation of the spatial fluxes is described next. At this point, it is convenient to split the fluxes into inviscid and viscous components so that each may be treated separately.

$$F = F_I + F_V \tag{3.6}$$

The Euler equations are obtained by neglecting the viscous component, and have a hyperbolic character with wave-like solutions. The viscous component, when combined

with the transient terms, have a parabolic character. The inviscid and viscous fluxes are given, respectively, by

$$F_{Ij} = \begin{pmatrix} \rho u_j \\ \rho u u_j + p\delta_{1j} \\ \rho v u_j + p\delta_{2j} \\ \rho w u_j + p\delta_{3j} \\ E_v u_j \\ (E+p)u_j \end{pmatrix}, \qquad F_{Vj} = \begin{pmatrix} 0 \\ -\tau_{1j} \\ -\tau_{2j} \\ -\tau_{3j} \\ q_{vj} \\ q_j + q_{vj} - u_k \tau_{kj} \end{pmatrix}. \tag{3.7}$$

3.2.1 Inviscid Fluxes

The Euler equations, comprised of the transient terms and inviscid fluxes, are hyperbolic in character. This means that information propagates along characteristics, and numerical schemes based on this property are used for the inviscid fluxes. The high-fidelity nature of the simulations in this work require high-order representations of the inviscid flux vector. The numerical scheme needs to be able to resolve turbulent eddies, requiring minimal dissipation which does not damp out the relevant physics. The scheme must also provide stable solutions near shocks, where large gradients are present, meaning shock capturing techniques are required. To start, the Steger-Warming flux vector splitting method is outlined. Following this, the method is modified to decrease numerical dissipation and increase resolution of turbulent flows.

Steger-Warming Flux Vector Splitting

The Steger-Warming characteristic-based flux vector splitting method is used for the inviscid fluxes. This method is built on the linear and homogeneous nature of the fluxes with respect to the conserved variables U:

$$F_I(\lambda U) = \lambda F_I(U) \tag{3.8}$$

where λ is an arbitrary scalar. Using this observation, the flux can be exactly represented with a Jacobian, A, as

$$F_I(U) = \frac{\partial F_I}{\partial U} U = AU. \tag{3.9}$$

The stability requirements dictate that an upwind-biased flux evaluation scheme be used. To accomplish this, the Steger-Warming method splits the flux into positive and negative running components. The direction of travel is determined by the characteristics of the flow, given by the eigenvalues of the Jacobian. The Jacobian is diagonalized, and the fluxes are split according to the sign of the eivenvalues of the Jacobian. The fluxes are evaluated in a coordinate system that is local to the given face,

$$F_{Ij}\hat{n_j} = \begin{pmatrix} \rho u' \\ \rho u u' + p s'_x \\ \rho v u' + p s'_y \\ \rho w u' + p s'_z \\ E_v u' \\ (E+p)u' \end{pmatrix} \tag{3.10}$$

where $\hat{n}_j = (s'_x, s'_y, s'_z)$ are the components of the orthonormal face vector, and $u' = us'_x + vs'_y + ws'_z$ is the component of velocity normal to the face.

Directly diagonalizing the Jacobian is difficult, but can be made easier by decomposing A into components,

$$A' = \frac{\partial U}{\partial V}\frac{\partial V}{\partial U}\frac{\partial F'_I}{\partial V}\frac{\partial V}{\partial U} \tag{3.11}$$

where V is a vector of primitive variables, chosen to be:

$$V = (\rho, u, v, w, e_v, p)^T. \tag{3.12}$$

The eigenvalue decomposition can now be given by

$$\frac{\partial V}{\partial U}\frac{\partial F'_I}{\partial V} = C^{-1}\Lambda C, \tag{3.13}$$

where Λ is a diagonal matrix containing the eigenvalues, and C is a matrix containing the eigenvectors. Eigenvalues represent characteristic speeds, and are u', corresponding to bulk velocity, and $u' \pm a$, corresponding to fast and slow acoustic waves.

Separating the positive and negative eigenvalues, the inviscid flux can be written in terms of forward and backward moving components,

$$F'_I = F'_+ + F'_-, \tag{3.14}$$

where

$$F'_{\pm} = \frac{\partial V}{\partial U} R^{-1} C^{-1} \Lambda_{\pm} C R \frac{\partial V}{\partial U} U = A'_{\pm} U, \tag{3.15}$$

and R is a rotation matrix included to avoid singularities by transforming the momentum components from a local face aligned coordinate system to the Cartesian system.

The flux is evaluated across a face, designated as $i+1/2$, for left (i) and right $(i+1)$ elements with the upwind method:

$$F'_{i+1/2} = A'_{+,i} U_i + A'_{-,i+1} U_{i+1} \tag{3.16}$$

This is the first-order Steger-Warming method, and is very stable in regions of shocks, but very dissipative as well. Less dissipative methods are needed so that relevant flow physics are not damped out of the solution. By evaluating the flux Jacobians at the face, the numerical dissipation is reduced, yet the form of the fluxes remains nearly the same[26].

$$F'_{i+1/2} = A'_{+,i+1/2} U_i + A'_{-,i+1/2} U_{i+1} \tag{3.17}$$

Here, $A'_{i+1/2}$ is evaluated using a state vector averaged from the left and right elements $((U_i + U_{i+1})/2)$. While less dissipative, this modified Steger-Warming (MSW) approach is less stable near shocks due to insufficient numerical dissipation. To increase stability, a pressure switch is used to transition between the first-order Steger-Warming method and the MSW method, such that the higher dissipative method is only used in regions where it is needed.

One other modification is often made to the MSW method to reduce error. Across shocks and in stagnation regions, where eigenvalues are nearly zero, numerical error has no way to convect away from the region. This error can accumulate and can generate non-physical solutions. An eigenvalue limiter, or "sonic glitch correction", can be applied to the eigenvalues to prevent this build up of error in the form of adding a small fraction of the speed of sound to the eigenvalues. However, in regions where the eigenvalues are not nearly zero, such as in regions of shear or boundary layers, this limiter adds dissipation and increases artificial mixing. The flows considered in this work do

not exhibit regions where the eigenvalues are nearly zero, and the sonic glitch correction is not used.

Higher-Order Inviscid Fluxes

While the MSW method reduces dissipation compared to the original Steger-Warming method, upwind methods in general contain large amounts of numerical dissipation which damp out small flow scales. This numerical dissipation, or artificial viscosity, can be orders of magnitude larger than the physical viscosity for high Reynolds number flows. Higher order solutions are obtained by using a more accurate approximation of the flow properties at a face. By splitting the flux into central and dissipative components, much less dissipative central schemes can be used, and the amount of dissipation can be controlled as needed. This increases the resolvable energy spectrum, and gives more accurate simulations.

The MSW flux scheme can be rewritten as

$$F'_{I,i+1/2} = A'_{i+1/2}(\Lambda)\frac{(U_{i+1}+U_i)}{2} - A'_{i+1/2}(|\Lambda|)\frac{(U_{i+1}-U_i)}{2}, \tag{3.18}$$

where $A'_{i+1/2}(\Lambda)$ and $A'_{i+1/2}(|\Lambda|)$ are the flux Jacobians evaluated with the specified eigenvalue vectors. The first term is the symmetric non-dissipative central portion of the flux, and the second term is the upwinded dissipative portion. Dissipation is controlled through a switch multiplying the dissipative component, resulting in the final form of the inviscid flux scheme,

$$F'_{I,i+1/2} = F'_{sym} + \alpha F'_{diss}. \tag{3.19}$$

Here, α ranges from zero to one, and should be active in regions of high gradients where large amounts of dissipation are needed, and zero elsewhere.

In the higher compressible temporally evolving shear layer simulations, shocklets are strong enough to require numerical dissipation for stability. Two different switches are used in these simulations. The first switch uses the expression suggested by Ducros[27],

$$\alpha = \min\left(\frac{\theta^2}{\theta^2+\omega^2+\epsilon}, 1\right), \tag{3.20}$$

where θ is the divergence of velocity, ω is the vorticity, and ϵ is a small parameter to avoid division by zero. The switch is based on the physics of the flow, tending to one in regions of large flow divergence, and to zero for vorticity dominated flows.

When the Ducros switch is used in regions where the vorticity is virtually zero, but acoustic waves are present, the switch tends to one as dilatation dominates. As the acoustic waves propagate, the switch may flip between low and high values repeatedly. This is commonly observed in free-stream regions of the flow, where turbulence has not developed but acoustic waves are propagating. The flipping can generate large amounts of dissipation, and induce non-physical vorticity and mixing. For this reason, a second switch is used where α is set to a constant value throughout the flow-field. The consequences and results of using either of these methods are discussed in later chapters.

Increased flow accuracy simulations are obtained by replacing the symmetric portion of Eq. 3.19 with higher-order approximations. The kinetic energy consistent flux scheme, developed by Subbareddy and Candler[28], is used for the symmetric portion of the flux. In this scheme, a secondary kinetic energy conservation equation is obeyed, and a central-based gradient reconstruction using neighboring elements is used to achieve higher-order fluxes. This flux scheme is less dissipative and provides better resolution of small-scale structures and broader energy spectra than MSW fluxes.

3.2.2 Viscous Fluxes

The viscous fluxes are comprised of the diffusive terms, and are evaluated using a central based scheme. Equation 3.7 contains gradients of local flow primitive quantities. The local flow variables are calculated by averaging values across neighboring elements. Gradients are computed at cell centers using a least-squares approximation, where flow variables are constructed with weights determined by the distance from the cell's centroid. The viscous fluxes require gradients in the face normal direction, and so simple averaging of the gradients to the face can results in a poor approximation in the face normal direction. The cell-centered gradients are interpolated to the face's surface normal vector using the deferred correction method. The viscous fluxes are then computed and summed over each face in similar fashion as the inviscid fluxes.

3.3 Time Integration

Recalling Eq. 3.5, and moving the flux scheme to the right-hand side,

$$\frac{\partial \overline{U}}{\partial t} = -\frac{1}{V_i} \sum_{faces} \left(F_i' S_i \right) + \overline{W}, \tag{3.21}$$

the left-hand side remains to be be discretized to advance the solution in time. Explicit and implicit methods can be used to advance the solution in time. The maximum allowable timestep in explicit schemes is limited by the cell size and the local speed of sound. Information cannot travel faster than the characteristic time of propagation between cells (based on the maximum eigenvalue of the system), referred to as the Courant Friedrichs Lewy (CFL) condition. Implicit methods are often used to overcome this restrictive (and oftentimes infeasible) time requirement. However, these schemes do not, in general, resolve all flow time scales.

The high-fidelity nature of the direct numerical simulations in this study require that all length and time scales be resolved. Implicit methods are therefore not applicable, and explicit methods are used for all simulations. The timestep requirements of the fundamental nature of the flows studied here are not infeasible; with most simulations taking on the order of days (1-2 usually). Resolution of the flow and relaxation time scales is discussed in the last part of this section.

3.3.1 Explicit Methods

The time derivative in Eq. 3.21 can be approximated with a simple first-order backwards finite difference method, known as a first-order explicit Euler method.

$$\frac{\overline{U}^{n+1} - \overline{U}^{n}}{\Delta t} = -\frac{1}{V_i} \sum_{faces} \left(F_i'^{n} S_i \right) + \overline{W} \tag{3.22}$$

where n is the current time level at which all terms on the right-hand side are evaluated. It is easy to extend this equation to multi-step methods, resulting in higher-order explicit schemes. One common family of methods of this type are the Runge-Kutta (RK) methods.

To extend Eq. 3.22 to multi-step methods, an operator is defined using the right-hand side as

$$L_i^{(k)} = -\frac{1}{V_i} \sum_{faces} \left(F_i'^k S_i \right) + \overline{W}, \tag{3.23}$$

where the superscript k refers to the current sub-step that L_i is being evaluated at. The explicit Euler method, for example, can be rewritten as

$$\overline{U}^{n+1} = \overline{U}^n + \Delta t L_i^{(n)}. \tag{3.24}$$

The three stage third order total variation diminishing (TVD) scheme, given by Gottlieb and Shu[29], is used in this work for time advancement. The three stages of the RK3 method are given by

$$\begin{aligned} \overline{U}^{(1)} &= \overline{U}^n + \Delta t L_i^{(n)}, \\ \overline{U}^{(2)} &= \frac{3}{4}\overline{U}^n + \frac{1}{4}\overline{U}^{(1)} + \frac{1}{4}\Delta t L_i^{(1)}, \\ \overline{U}^{(n+1)} &= \frac{1}{3}\overline{U}^n + \frac{2}{3}\overline{U}^{(2)} + \frac{2}{3}\Delta t L_i^{(2)}. \end{aligned} \tag{3.25}$$

The timestep, Δt, is determined by the flow time scales.

3.3.2 Resolution of Time Scales

The simulations in this work use a constant timestep in Eq. 3.25. This allowed for comparison of different flows at the same non-dimensional time. The timestep was set such that both the turbulent and the relaxation time scales are well resolved. Timestep convergence studies showed that a timestep of at least thirty times smaller than the fastest time scale was sufficient.

$$\Delta t = \frac{\min(\tau_{turb}, \tau_{vib})}{30} \tag{3.26}$$

In the cases considered here, τ_{vib} is varied, and the minimum time scale in Eq. 3.26 changed between turbulent and vibrational time scales.

Chapter 4

Acoustic Damping

Previous studies have shown a strong effect on acoustic waves by internal energy relaxation modes in transition related studies. These have included theoretical[3, 19, 17], experimental[5, 6, 30], and computational[31, 32, 8], to name a few. The theoretical and computational results have shown that acoustic damping is optimal when the inverse relaxation time is the same order as the frequency of the wave.

While few studies have looked at the interaction of turbulence and internal energy relaxation modes, the conclusions have hinted that this interaction is coupled through acoustic modes[4, 9]. However, tuning of gas properties to turbulent flow scales such that optimal damping of turbulent quantities is achieved was not considered. One of the primary goals of this work is to examine the tuning of internal energy relaxation to turbulent motion, and much can be learned from theoretical and computational analysis of acoustic damping. The chapter is organized as follows: theoretical derivations of acoustic absorption by internal energy relaxation are presented, followed by computational simulations of acoustic waves interacting with a relaxing gas. Finally, some brief comments are made on estimation of the optimal damping frequency for a given gas.

4.1 Theoretical Absorption of Acoustic Energy

Theoretical results have shed light on much of the underlying physics of acoustic absorption by internal energy mode relaxation. These results are outlined and discussed in this section. While these results have been extremely useful, other attempts to describe

absorption have been made using non-physical interpretations of physical quantities. Specifically, the role of bulk viscosity in internal energy relaxation is often cited as a mechanism of absorption. The role of bulk viscosity is discussed in this section, followed by theory on the correct way of describing acoustic absorption through finite-rate energy equations.

4.1.1 Role of Bulk Viscosity in Acoustic Energy Absorption

Few physical parameters have as interesting a history as the bulk viscosity parameter. Bulk viscosity has been interpreted in two fundamentally different ways. One interpretation modifies the stress tensor to account for the finite range of intermolecular forces in a dense gas. For dense gases, the intermolecular forces must be considered at all times due to the close proximity of the molecules. Bulk viscosity accounts for these effects, and is taken as physically meaningful and correct in this context[3, 19]. While the definition of a dense gas is not rigorously defined, Clarke and McChesney[3] state that a gas is dilute if its pressure is below 1-10 atm and its temperature is well above the critical value. We do not consider dense gases in this work, and therefore this interpretation is not discussed further.

The second interpretation attempts to describe the relaxation of internal energy modes towards equilibrium. Essentially, the parameter is used to "dissipate" energy between modes by modifying the pressure tensor. The pressure tensor, derived from kinetic theory[19], is given by

$$P_{i,j} = \left(p' - \mu_\beta \frac{\partial u_k}{\partial x_k}\right)\delta_{i,j} - \mu\left(\frac{\partial u_i}{\partial u_j} + \frac{\partial u_i}{\partial u_j} - \frac{2}{3}\frac{\partial u_k}{\partial u_k}\delta_{i,j}\right), \tag{4.1}$$

where p' is the equilibrium pressure which would exist if all internal energy modes were instantaneously equilibrated with the translational mode, and μ_β is the bulk viscosity.

A physical interpretation demonstrating how bulk viscosity can be used as a relaxation parameter for a gas in rotational nonequilibrium is given in Vincenti and Krueger[19]. When a gas is compressed or expanded, as in a shock wave or an acoustic wave propagation, the translational energy is modified. For a compression, energy is initially deposited into the translational mode. As the energy in the translational mode increases, the rotational mode equilibrates with the translational mode through

collisions over a finite time period. This generates an initial overshoot in translational energy, followed by a relaxation towards equilibrium with the rotational mode. Associated with this energy discrepancy is a kinetic pressure, determined solely from the translational energy, and the previously mentioned equilibrium pressure. The difference in pressures is controlled by the bulk viscosity, given by Vincenti and Krueger as

$$p = p^* - \mu_\beta \frac{\partial u_i}{\partial x_i}. \tag{4.2}$$

In this way, μ_β is interpreted as a relaxation parameter which is proportional to the finite time period. The presence of μ_β in the viscous stress tensor is used to account for acoustic absorption by modulating the dilatation, or put more simply it dissipates energy from a compression to the internal energy modes.

Wang Chan and Uhlenbeck[33], Monchick, Yun, and Mason[34], and Lighthill[35] derive expressions relating μ_β to the internal energy mode relaxation rate. Vincenti and Krueger[19] give a relation for rotational nonequilibrium as

$$\mu_\beta = (\gamma - 1)^2 \rho e \frac{c_{v,rot}}{c_v} \tau_{rot}. \tag{4.3}$$

In this framework, describing acoustic absorption seems simple and straightforward, and one has to question why computations are complicated with extra finite-rate energy equations for each mode when a much simpler form can be used. For rotational nonequilibrium, where the relaxation time is significantly faster than any flow time (approximately 10 collisions) and only small amounts of energy are transferred, the above theory provides reasonable results. However, for more complex flows where multiple internal energies are active with disparate relaxation scales, how well can one parameter resolve the system?

The short answer is that bulk viscosity as a relaxation parameter is not physically consistent, and therefore cannot resolve complex systems in a meaningful way. Equation 4.3 was derived under highly restrictive assumptions, such as short relaxation times with regard to the characteristic time of the system, meaning the internal energies are not in significant nonequilibrium. For an acoustic wave propagating through a gas, this requires

$$\omega\tau \ll 1, \tag{4.4}$$

where ω is the angular frequency of the perturbation. Meador et al.[36] develop a generalized version of this method, removing the restriction in Eq. 4.4. In doing so, they show that μ_β must be determined by comparison with other data. This is also true for the non-generalized method, as mentioned in Monchick, Yun, and Mason[34]. Equation 4.3 was derived by force-fitting the parameter to a separate model. In this way, bulk viscosity is force-fitted to describe a single aspect of internal energy relaxation. The above derivation was derived for acoustic absorption, but cannot describe dispersion. This can be seen by calculating the speed of sound with the generalized method. At both low and high frequencies, the method gives the equilibrium speed of sound, rather than the correct frozen speed of sound at high frequencies.

Bulk viscosity as a *non-physical adjustable parameter* to describe internal energy relaxation is not physically consistent, and should not, in general, be used. This is demonstrated[3, 36] as the parameter is defined by force-fitting to experimental data, and only able to describe a single aspect of relaxation. In select cases, bulk viscosity can be used to represent a single aspect of relaxation, but should be done so with extreme caution. Rather, finite-rate energy relaxation governing equations should be used for each energy mode to *confidently* describe physical relaxation processes.

4.1.2 Finite-Rate Energy Relaxation Damping of Acoustic Waves

While the bulk viscosity method can be used in select cases to describe acoustic absorption, more rigorous and physically consistent theory can be derived. These theories are outlined here, and references are given for more detail. Two theories for an acoustic wave interacting with a gas containing a single relaxation mode, developed in different ways, are presented which give identical results. A third method which is general to a gas with multiple internal energy relaxations is then presented.

Vincenti and Krueger[19] studied the effects of an acoustic wave propagating through a gas with a single internal energy relaxation mode. They reduced the acoustic disturbance equations to a single nonequilibrium form of the wave equation by introducing a potential function. In a similar analysis, Clarke and McChesney[3] theoretically examined the effect of a single chemical reaction on an acoustic wave. Both analysis revealed that internal energy relaxation has a damping effect on the acoustic wave, and that this damping is greatest when the inverse relaxation time is on the order of the frequency of

the wave. Figure 4.1, reproduced from Clarke and McChesney[3], shows how the damping per wavelength varies with frequency and relaxation rate for a typical relaxation process.

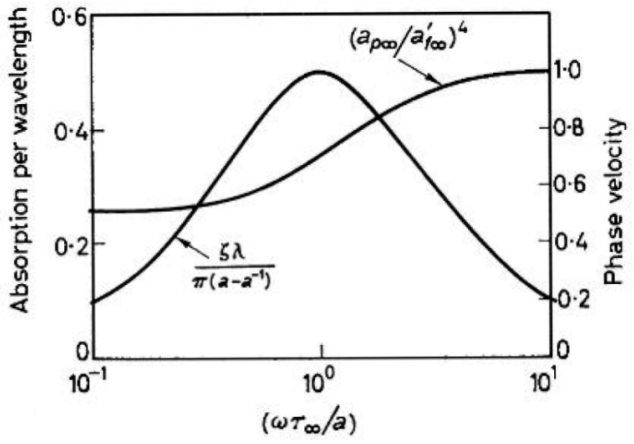

Figure 4.1: Absortion per wavelength and dispersion of an acoustic perturbation in an ideal dissociating gas[3].

Also shown in Fig. 4.1 is the phase velocity of the acoustic wave, normalized by the frozen speed of sound, and also describes dispersion. In flows with internal energy excitation, the wave speed varies as a function of its frequency and the response of the internal energy mode. For slow moving waves, the gas adjusts to the perturbation nearly instantly, and the wave propagates at the equilibrium speed of sound, shown on the far left of the figure. On the right side of the plot, waves propagate fast enough that the gas is not able to respond or transfer energy, and the gas is considered frozen to the acoustic mode, or as if the gas had no internal energy modes. The ratio of these two sound speeds, frozen and equilibrium, is a main factor in determining the maximum damping rate[3].

Meador et al[36] developed a method to describe absorption and dispersion using a different approach: by splitting the energy into two components. The first component is the energy of the mode that instantaneously equilibrates with the translational mode, and the second component is the energy of the relaxing mode. By solving the equations

for these energies, they developed expressions for dispersion and absorption of acoustic waves, respectively, as

$$a^2 = 2\left(\frac{a_{eq}}{\zeta}\right)^2 \left(\frac{1+\omega^2\tau_p^2}{1+\omega\tau_p\tau_v}\right)\left[(1+\zeta^2)^{1/2}-1\right], \tag{4.5}$$

$$\alpha = \frac{2\pi}{\zeta}\left[(1+\zeta^2)^{1/2}-1\right], \tag{4.6}$$

where

$$\zeta = \frac{\omega(\tau_p-\tau_v)}{1+\omega^2\tau_p\tau_v} \qquad \tau_p = \tau\frac{c_{p,e}}{c_p}, \quad \tau_v = \tau\frac{c_{v,e}}{c_v}. \tag{4.7}$$

The above methods were developed with different approaches, but yield similar results for acoustic waves propagating through a gas with a single mode of internal energy relation. While a lot can be learned from considering a single internal energy mode, practical applications demand a more general theory. Fujii and Hornung[17, 7] modelled an acoustic wave propagating through a gas with multiple internal energy relaxation modes by following the approach of Vincenti and Krueger[19]. They solved a general set of acoustic disturbance equations by introducing a potential function. Each mode is represented by a perturbation equation, and vibration and chemistry energies can be selectively activated. This form not only allows for solutions of realistic gas mixtures in equilibrium, but is also able to identify which energy modes are responsible for damping at particular frequencies.

Wagnild[18] used the approach developed by Fujii and Hornung to derive an expression for the damping per wavelength at the optimal frequency for a vibrational mode as

$$\epsilon_{\lambda,\max(f)} = 2\pi\frac{\sqrt{1+\frac{c_{vv}^*}{c_v}}-\sqrt{1+\frac{c_{vv}^*}{c_p}}}{\sqrt{1+\frac{c_{vv}^*}{c_v}}+\sqrt{1+\frac{c_{vv}^*}{c_p}}}. \tag{4.8}$$

Comparing this equation to Eq. 4.6, both forms have a strong dependence on the ratio of the nonequilibrium specific heat to the equilibrium specific heat. This means that the ability of a gas to damp an acoustic wave is dependent on the amount of energy that can be transferred and stored in an internal energy mode. This observation is consistent

with Fig. 4.1, that the damping rate is highly dependent on the ratio of the frozen and equilibrium wave speeds.

These observations are further quantified in Fig. 4.2, for rotational nonequilibrium calculated using the method developed by Meador et al[36]. Wagnild[18] showed that the maximum damping rate of vibrational relaxation for all diatomic molecules is 13.4%. The maximum damping for rotational relaxation is over twice as large. This makes sense, since $(c^*_{vv}/c_v$ is larger for rotation than vibration in a diatomic molecule, and energy is more easily transferred and stored in the rotational mode.

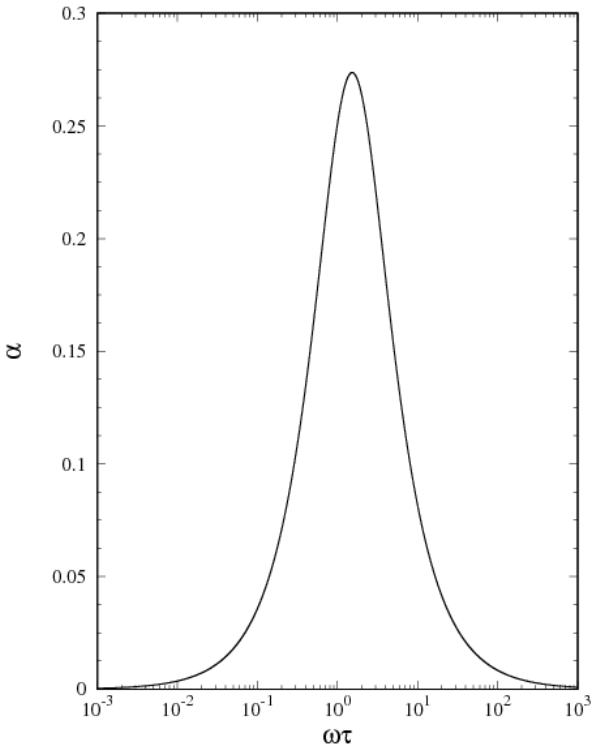

Figure 4.2: Dissipation per wavelength of a gas with active rotational energy relaxation, derived from theory.

The ratios of specific heats are plotted in Fig. 4.3 for different internal energies and gases. CO_2 is a polyatomic molecule and has two axes of rotation, the same as a diatomic

molecule, and therefore has the same rotational energy capacity. The accessibility of the bending modes to transfer and store energy at low T is evident in Fig. 4.3, and is consistent with previous observations[5, 6, 7]. While rotational energy is able to damp acoustic energy more than vibration, in realistic flows, the scales involved are either non-existent or violate continuum assumptions. Rotational energy usually equilibrates with translational energy in approximately ten collisions, or ten mean free paths. In the turbulent flows considered in the next chapter, the smallest length scales of the flow are the Kolmogorov scales, calculated to be at least six orders of magnitude larger than the rotational equilibration length.

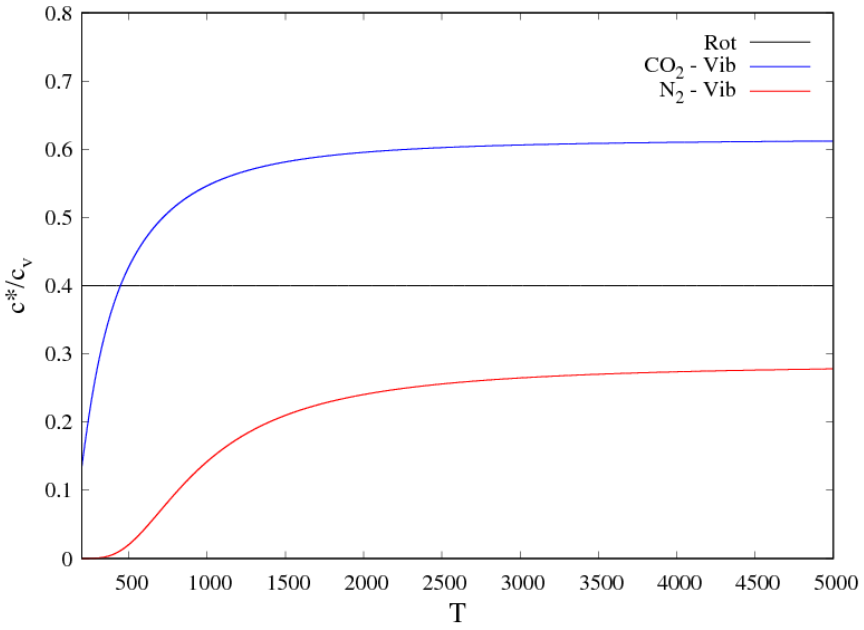

Figure 4.3: Ratio of relaxation to equilibrium heat capacity for rotational energy relaxation and vibrational energy relaxation in CO_2 and N_2. Note that because CO_2 is a polyatomic molecule with only two axes to rotate about, c_v^{rot} is the same as a diatomic molecule.

4.2 Simulations of Acoustic Wave Damping

DNS of acoustic wave propagation through a gas with internal energy relaxation can assist theory in understanding absorption mechanisms. Wagnild[18] and Wagnild and Candler[8] computed DNS of acoustic wave propagation in static and mean flow gases with chemical and vibrational internal energy modes. The results for vibrational energy relaxation compared well with Fujii, and less so but still reasonably well for chemical reactions. Differences in kinetic models are a likely cause for these differences.

In this work, DNS of acoustic wave propagations are analyzed following the methodology of Wangild[18]. An acoustic wave is propagated through a one-dimensional domain containing an inviscid static gas in thermal equilibrium with a density of $0.1\,\mathrm{kg/m^3}$ and a temperature of $1000\,\mathrm{K}$. The frequency of the wave is set to $100\,\mathrm{kHz}$. The domain is $30\,\mathrm{cm}$ long, and discretized with 30000 equally spaced cells. An additional $20\,\mathrm{cm}$ domain containing 50 grid cells is grown from the end of the domain, with cell sizing quickly increased to minimize wave reflections.

US3D[20] is used to simulate the propagating wave. The numerics, models, and governing equations were described in the previous chapters. Second-order kinetic energy consistent fluxes are used for the convective terms, and time integration uses a third-order Runge-Kutte method. A supersonic outflow boundary condition was applied to the end of the domain. The acoustic wave inflow conditions are obtained by solving the non-reacting Euler equations with a frozen wave form. This form is an approximation to vibrational non-equilibrium at the beginning of the domain, but is deemed acceptable for the purposes of analysis in this work. The inflow conditions are derived based on Balakumar[37], where an acoustic wave is driven by a pressure disturbance, The one-dimensional static form, relevant to this work, is given by

$$\begin{pmatrix} \rho' \\ u' \\ v' \\ w' \\ T' \end{pmatrix} = \begin{pmatrix} \frac{1}{a_f^2} \\ \frac{k}{\rho\omega} \\ 0 \\ 0 \\ \frac{(\gamma-1)T_0}{\rho_0 a_f^2} \end{pmatrix} p_{ac} \exp(i(kx - \omega t)) \tag{4.9}$$

where the dispersion relation relating the wavenumber, k, and angular frequency, ω, is

$k = \omega / a_f$.

Damped acoustic waves are studied in gases with vibrational nonequilibrium. The damping rate has been shown to be exponential with distance[7], and is therefore calculated as the natural logarithm of the maximum amplitude of the wave at each half wavelength. Initial DNS using a fictitious diatomic molecule were analyzed to validate the numerics and provide understanding of the damping process. The simulations consisted of varying the vibrational excitation level of the gas and the relationship between frequency and relaxation time $\omega\tau_{vib}$. These values were varied by changing the characteristic vibrational temperature and relaxation time of the gas. This allowed for consistency of grid spacing and timesteps between simulations.

DNS results of an acoustic wave propagating through a diatomic gas in vibrational nonequilibrium are compared with the theory developed by Meador et al.[36] in Fig. 4.4. Results obtained using the theory developed by Fujii and Hornung[17] were found to be identical to Meador et al. Excellent agreement between theory and DNS is demonstrated for all conditions tested.

Figure 4.4 also shows the effect of the excitation level (T/θ_v) on the damping process. The strongest rates of damping are shown to be around $\omega\tau_{vib} \approx 1$ and significant excitation of the vibrational mode. The damping rate also has a broadband effect over the range of frequencies as the excitation level is increased. Low levels of excitation result in no meaningful damping, as energy is not transferred into the vibrational modes.

Insight into the energy exchange mechanism between translation-rotational and vibrational modes, as well as acoustic wave propagation is observed in Figs. 4.5 - 4.7 for three different conditions. The first figure is for an acoustic wave propagating through a frozen gas. The frequency of the gas is sufficiently fast that the gas has no time to respond, and very little energy can be transferred into the translational mode. In the second figure, the frequency of the wave is slow enough that the gas nearly instantaneously responds to the perturbation. Because the gas is almost fully equilibrated, the energy transfer between modes is nearly zero. The final case demonstrates a wave with frequency equal to the vibrational relaxation rate. In this case, the damping is near the optimal point, and significant damping occurs relative to the first two cases. The energy transfer between translation-rotational and vibrational modes is also apparent, in the form of the phase shift between the temperatures. As the translational

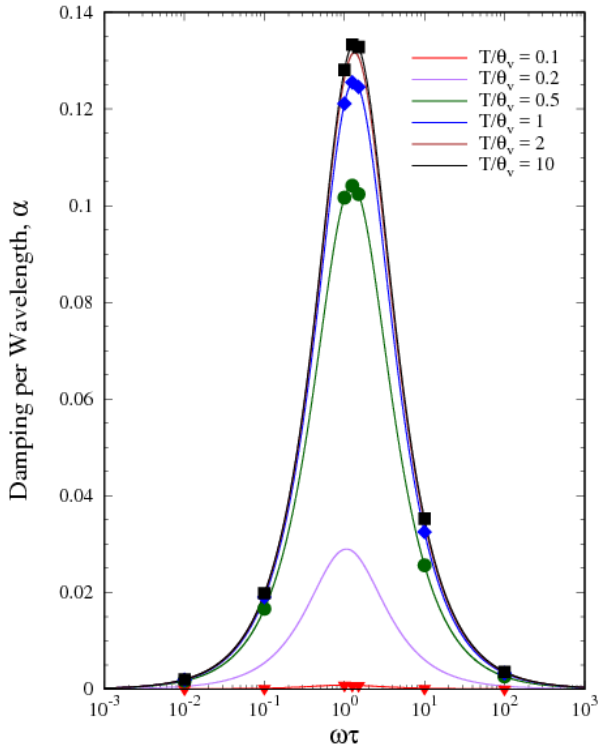

Figure 4.4: Dissipation per wavelength of a diatomic gas with vibrational energy relaxation at different excitation levels. Solid lines are given from theory, and symbols are obtained from DNS.

energy increases in response to the acoustic perturbation, the vibrational temperature lags behind. Energy is then transferred from the vibrational to the translational modes, resulting in a reduced load on the thermal temperature. As the translational energy is reduced, the process is eventually reversed, and energy is transferred from vibrational to translational modes.

4.3 Estimation of Optimal Damping Frequency

One final note is made on the estimation of the optimal damping frequency for a given gas mixture. Through kinetic theory relations, the optimal damping frequency can be

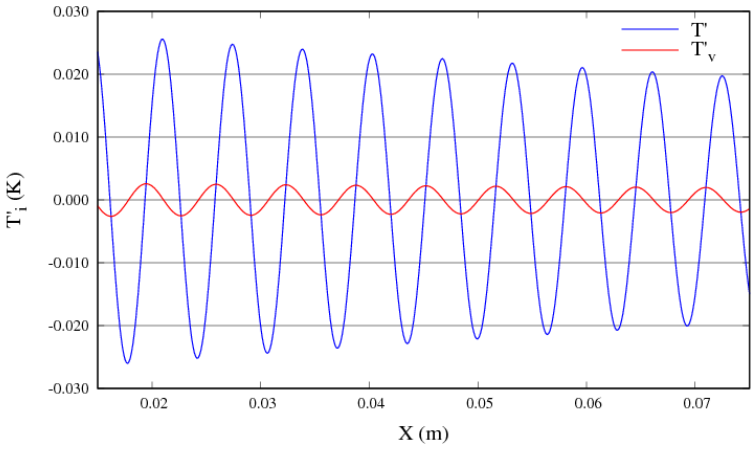

Figure 4.5: Temperature perturbations from an acoustic wave propagating through a fictitious diatomic gas near the frozen regime ($\omega\tau_{vib} = 10$).

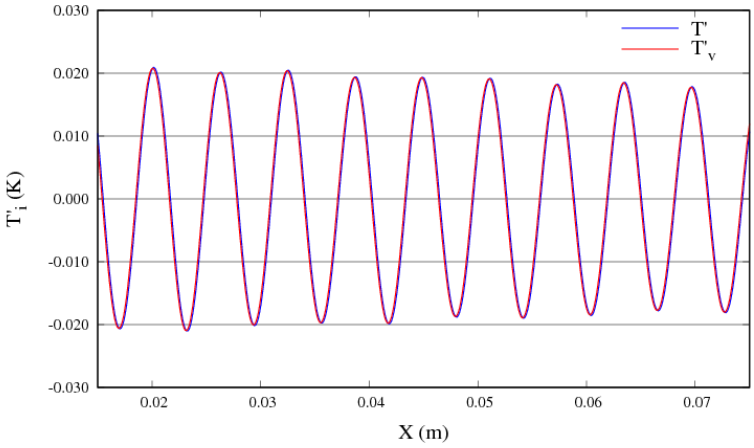

Figure 4.6: Temperature perturbations from an acoustic wave propagating through a fictitious diatomic gas near the equilibrium regime ($\omega\tau_{vib} = 0.1$).

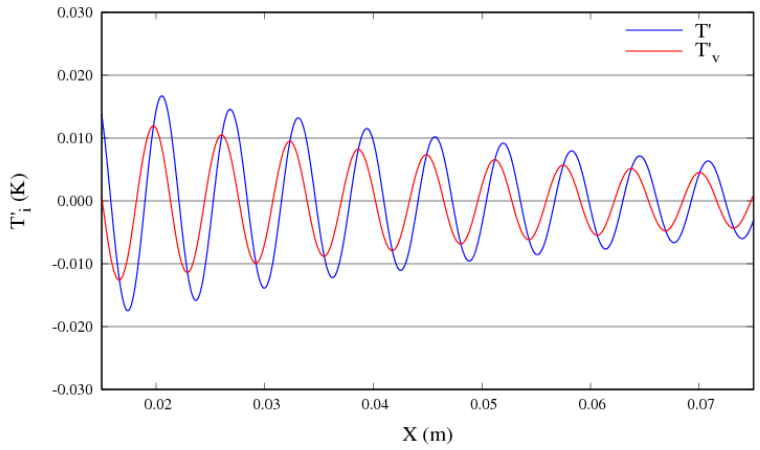

Figure 4.7: Temperature perturbations from an acoustic wave propagating through a fictitious diatomic gas near the location of optimal damping ($\omega\tau_{vib} = 1$).

related to the relaxation time of the gas. In this way, relaxation time can be used to easily predict the optimal damping frequency. Alternatively, given a frequency, one can determine the vibrational relaxation rate (i.e. gas state) that provides optimal damping.

The relation is derived using the mean free path, λ, defined as,

$$\lambda = 2\frac{\mu}{\rho\overline{C}}. \tag{4.10}$$

Substituting the definition of the mean free path into the definition of the collision time,

$$\tau_c = \frac{\lambda}{\overline{C}} = \frac{\pi}{4}\frac{\mu}{p} \quad \rightarrow \quad p\tau_c = \frac{\pi}{4}\mu, \tag{4.11}$$

where $\overline{C}$ is the mean molecular speed, the collision time is related to the gas. Using this relation, and defining the number of collisions required for equilibrium as $\tau_{relax} = N_c\tau_c$, the optimal damping frequency is related to the relaxation time using $\omega\tau_{relax} \approx 1$ by

$$f_{opt} = \frac{2p}{N_c\mu\pi^2}\text{Hz}. \tag{4.12}$$

Chapter 5

Compressible Isotropic Turbulence

Turbulent flows contain a broadband spectrum of acoustic waves, with a wide range of length and time scales. In hypersonic turbulent flows, internal energies can have relaxation scales which are on the same order of the turbulent scales. These internal energies can interact with the turbulent motion as energy is transferred into or out of the mode[4]. Understanding the fundamental energy exchange mechanisms and how these turbulent scales relate to internal energy mode relaxation is the focus of this chapter.

DNS of compressible isotropic turbulence with vibrational energy relaxation is studied. Isotropic turbulence is a simple turbulent flow commonly used for understanding fundamental flow phenomena. The universal small scales represented in isotropic turbulent simulations are found in all turbulent flows. Physical parameters can be varied to understand the relation of scales, and individual effects are more easily isolated.

This chapter describes the governing parameters of the flow and the initial conditions. Scales of motion are discussed, and a vibrational Damköhler number is introduced to relate the vibrational relaxation rate to a turbulent motion rate. Simulation details and numerical considerations are provided. The governing parameters, including the vibrational relaxation time, are varied to understand how the relaxation rate tunes to the turbulence. Results and conclusions are presented and discussed.

5.1 The Flow

5.1.1 Governing Parameters

The governing non-dimensional parameters which characterize compressible isotropic decaying turbulence are: the integral length scale (L_I), the Taylor microscale (λ), the Taylor Reynolds number (Re_λ), and the turbulent Mach number (M_t).

$$L_I = \frac{3\pi}{4}\frac{\int_0^\infty [E(k)/k]\mathrm{d}k}{\int_0^\infty E(k)\mathrm{d}k} \tag{5.1}$$

$$\lambda^2 = \frac{u'^2}{\langle(\partial u_1/\partial x_1)^2\rangle} \tag{5.2}$$

$$Re_\lambda = \frac{u'\lambda\langle\rho\rangle}{\langle\mu\rangle} \tag{5.3}$$

$$M_t = \frac{\langle u_1^2 + u_2^2 + u_3^2\rangle^{\frac{1}{2}}}{\langle c\rangle} \tag{5.4}$$

In the definitions above, $E(k)$ is the shell-integrated spectrum of the velocity, u' is the turbulent fluctuating velocity, μ is the viscosity, c is the speed of sound, and $\langle ...\rangle$ are volume averaged quantities over the domain at a fixed time. The turbulent fluctuating velocity is computed as

$$u' = \langle(u_1^2 + u_2^2 + u_3^2)/3\rangle^{1/2}. \tag{5.5}$$

The large-eddy-turnover time is used as the characteristic flow time, and is defined by

$$\tau_{LE} = \frac{L_I}{u'}. \tag{5.6}$$

Previous studies have indicated that internal energy relaxation is coupled to the turbulence through the compressible modes of the turbulence[4]. Dilatational fluctuations, or the root-mean-square of the velocity divergence, is defined as

$$\theta' = \langle(\frac{\partial u_i}{\partial x_i})^2\rangle^{1/2}. \tag{5.7}$$

Unless otherwise noted, root-mean-square quantities are computed as:

$$\phi' = \langle (\phi - \langle \phi \rangle)^2 \rangle^{\frac{1}{2}}, \tag{5.8}$$

where ϕ is a given quantity. For convenience, and because all quantities discussed in this paper are computed over a volume average, the root-mean-square term will be dropped from the text. Fluctuating quantities should therefore be assumed to be defined as Eq. 5.8.

5.1.2 Initial and Boundary Conditions

Re_λ	M_t	k_0	Da_v
72	0.1	8	0, 1, 7.2, 10, 20, 30
72	0.3	8	0, 0.5, 0.98, 3.3, 7, 15
72	0.5	8	0, 0.125, 0.25, 0.5, 1, 2, 4, 8, 16, 32, 64
175	0.5	4	0, 0.1, 0.5, 0.86, 2, 4, 8, 16, 32, 64

Table 5.1: Summary of isotropic turbulent parameters used in each simulation.

Compressible isotropic turbulence is initialized by specifying M_t, Re_λ, T, and ρ. The parameters used in these simulations are summarized in Table 5.1. Simulations were initialized with values of $Re_\lambda = 72$ and 175, and $M_t = 0.1$, 0.3, and 0.5. Temperature and density were set to 800 K, and $1\,\mathrm{kg/m^3}$, respectively, and CO_2 is used as the gas. CO_2 has four vibrational modes: two bending, one symmetric, and one antisymmetric. The characteristic temperatures of vibration are relatively low (particularly the two bending modes: $\theta_v = 960K$), and are therefore more easily excitable than a gas like O_2 ($\theta_v = 2239K$). As the vibrational temperature approaches the characteristic temperature the vibrational modes become more and more excited, and more energy is stored within each mode.

The initial velocity spectrum is obtained from the energy spectrum,

$$E(k) \sim k^4 \exp\left(-2\frac{k^2}{k_0^2}\right), \tag{5.9}$$

where k is the non-dimensional wavenumber and k_0 is the wavenumber containing the most energy. The values of k_0 are 4 ($Re_\lambda = 175$) and 8 ($Re_\lambda = 72$). Incompressible velocities are generated from Eq. 5.9 using the method developed by Rogallo[38]. The velocities are scaled to maintain the specified M_t and T. This is done to achieve temperatures which are high enough to excite the vibrational modes of the gas in a meaningful way.

The solution domain is a box with non-dimensional lengths of 2π. Viscosity is calculated using the Blottner fits described in Chapter 2, because we are using CO_2 and desire a realistic viscosity relation. The box is then scaled to dimensional lengths to maintain Re_λ and M_t. Boundary conditions are set to be periodic in all three Cartesian directions for all flow variables.

The velocity field obtained from Eq. 5.9 is initially divergence-free and the thermodynamics are not specified. Ristorcelli and Blaisdell[39] show there are finite density, temperature, and dilatational fluctuations in a physically consistent initialization of compressible isotropic turbulence. This method couples the initial underlying turbulent flow-field to the thermodynamic and divergence fields, and is used to initialize the turbulent flows in this chapter. Details of this initialization are provided in Appendix A. Vibrational energy is initially turned off and is not activated until after the initial transient time, described next.

The turbulent flow-field requires a short transient time to develop into a realistic turbulent flow. This transient time is determined by the mean values of the velocity derivative skewness $S_i = \langle(\partial u_i/\partial x_i)^3\rangle/\langle(\partial u_i/\partial x_i)^2\rangle^{3/2}$. Tavoularis et al.[40] and Orszag and Patterson Jr[41] show experimental data that S_i is in the range of $[-0.6 : -0.35]$ for $Re_\lambda \sim 50$. The flow is considered to be in a realistic turbulent state when S_i reaches an approximately constant value within this range. For the cases considered here, this state is achieved at a non-dimensional time of 0.75 for $Re_\lambda = 72$, and 1 for $Re_\lambda = 175$.

After the initial transient the grid is rescaled to match the initial Re_λ, allowing for longer decay times. Vibrational energy relaxation is activated at this time as well. The initial vibrational temperature is set equal to the translational temperature ($T_v = T$). This initialization was studied by setting T_v' to zero and to opposite T', and was found to have little effect on the conclusions. All results given below are offset such that $t/\tau_{LE} = 0$ corresponds to when vibrational energy relaxation is activated.

5.1.3 Scales of Motion

In Chapter 4, optimal damping for an acoustic wave was shown to occur when the frequency of the wave was on the order of the inverse vibrational relaxation time. Turbulent flows contain a broadband spectrum of frequencies, with a wide range of length and time scales. Some examples of these scales in isotropic turbulence are the length of the box (L), the integral length scale (L_I), the Taylor microscale (λ), the Kolmogorov scales (η, u_η, τ_η), the acoustic wave speed (c), the fluctuating velocity (u'), the bulk acoustic time scale (L/c), the large-eddy turnover time (τ_{LE}), and the turbulent Mach number (M_t). In order to relate the vibrational relaxation rate to a turbulent motion rate, a vibrational Damköhler number is defined as

$$Da_v = \frac{\tau_{LE}}{\tau_{vib}} \tag{5.10}$$

The choice of the large-eddy turnover time as the time scale of the turbulent motion is merely a matter of convenience at this point. Determining the relevant time scale is essential in determining how the vibrational relaxation rate tunes to the turbulent flow. For Da_v significantly greater than one, the equilibrium case is approached; this corresponds to the left side of Fig. 4.4 for a fixed τ_{vib}. As Da_v becomes significantly less than one, the frozen case is approached; corresponding to the right side of Fig. 4.4.

The tuning of the vibrational relaxation rate to the turbulent flow is studied by varying Da_v through τ_{vib} in Eq. 5.10. For the flows considered in this work, the vibrational relaxation time is essentially a constant. The vibrational relaxation time is set to match a given Da_v by modifying the constants A and B in Eq. 2.21. Camac[25] rates are typically used for CO_2 vibrational relaxation, where all modes are assumed to relax together. This means that each CO_2 mode uses the same A and B and has the same $\tau_m = \tau_{vib}$. The same assumption is used when modifying Da_v, and all modes use the same modified constants and relaxation time.

5.2 Simulation Details

5.2.1 Flow Solver

The governing equations, assumptions, and models used for these simulations are presented in detail in Chapter 2. The US3D flow solver is used to simulate compressible isotropic turbulence[20]. Convective fluxes are approximated using a sixth-order kinetic energy consistent low-dissipation numerical scheme[28]. The low turbulent Mach number cases presented in this chapter do not require any further dissipation to be added. Viscous fluxes are computed using a central-based deferred-correction approach. A third-order explicit Runge-Kutta method is used for time integration. These numerical methods are outlined in Chapter 3. The initialization procedure and numerics were validated using results from Samtaney et al[42].

5.2.2 Grid Requirements

For both Re_λ, grid sizes of 256^3 are used. Grid convergence was tested by doubling the number of points in each direction (512^3). The turbulent quantities, including fluctuating dilatational spectra, are sufficiently converged between the two grid sizes. The grid convergence studies were performed for both values of Re_λ, and for cases with and without vibrational relaxation. At all times, $k_{max}\eta > 1$, where k_{max} is the largest wave number, indicating that the smallest scales are resolved.

Results from the cases using the 256^3 grid were also compared using a smaller grid size of 128^3. Mean and fluctuating kinetic and thermodynamic quantities were converged between the two grids. However, quantities based on gradients, specifically the dilatation, did not converge when the grid size was doubled in each direction. These quantities are more sensitive to grid size, and have stricter grid requirements. The smaller 128^3 grid is not sufficient to resolve the quantities of interest in this study.

5.3 Isotropic Turbulence and Vibrational Energy Relaxation

The transfer of energy in Eq. 2.3 is modelled using Eq. 2.19, shown below in a simplified form.

$$w_v = \rho \frac{e_v^*(T) - e_v(T_v)}{\tau_{vib}}$$

The vibrational relaxation time, τ_{vib}, in the denominator is also used in Eq. 5.10. The rate of energy transfer is governed by this relaxation time, driving the transfer of energy between translational and vibrational modes. This energy exchange acts as a damping process for both mean and fluctuating quantities as the translational and vibrational modes relax towards equilibrium.

Viscous dissipation transfers kinetic energy into the translational energy modes, increasing the mean energy content of the translational mode. Mean energy is then transferred to the vibrational mode, reducing the energy contained in the translational mode. This is quantitatively seen in Fig. 5.1 for the evolution of mean temperature with and without vibrational relaxation in decaying isotropic turbulence. In the case with vibrational relaxation, an extra energy pool is available and a broader distribution of energies is possible. This broader distribution results in a decrease of T, and an increase in T_v. As the turbulence decays and viscous dissipation decreases, an equilibrium state is approached at a rate proportional to τ_{vib}.

The turbulence also generates fluctuations in the thermal state, with compressions and expansions generating acoustic waves. The vibrational energy lags these fluctuations and acts to damp the thermal fluctuations and absorb acoustic energy. This is shown qualitatively in Fig. 5.2, where the difference in translation and vibrational temperatures is shown at three different times. Near the beginning of the simulation, the turbulence is intense with a wide range of length and time scales, and large fluctuations in temperature occur. The vibrational energy lags behind at a rate proportional to τ_{vib}, as seen in the simplified source term given above, and the difference in temperatures is large. At a later time, shown in the middle plot, the turbulence intensity is reduced and the length and time scales are changing. The vibrational energy is starting to equilibrate with the translational energy as the fluctuations in the thermal state are reduced. Near the end

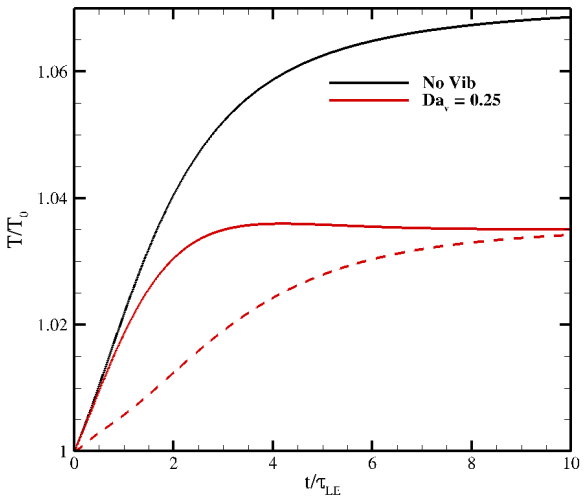

Figure 5.1: Evolution of mean temperatures with and without vibrational relaxation. T is shown with solid lines, and T_v with dashed lines. $Re_\lambda = 72$, $M_t = 0.5$.

of the simulation, the turbulence has decayed substantially and the vibrational energy is nearly in equilibrium with the translational energy.

This dynamic energy exchange can also quantitatively be seen in Fig. 5.3. The fluctuating temperatures and dilatation are compared between the cases with and without vibrational relaxation. Translational temperature fluctuations are reduced as energy is transferred to the vibrational mode. Dilatational fluctuations are also damped, indicating acoustic energy is absorbed into the vibrational mode (through the translational mode).

The kinetic energy (not shown) is virtually unaffected by vibrational energy relaxation. This was observed for all cases studied here. There is no direct mechanism of energy transfer between kinetic and vibrational modes (Eqs. 2.24 - 2.26). Energy must go through the translational mode, and then to the vibrational energy mode. This happens through viscous dissipation and acoustic compressions and expansions. The effect of the vibrational energy mode on these energy exchanges is too weak to be noticeable in the kinetic mode. This is evidenced further below, when compressible and

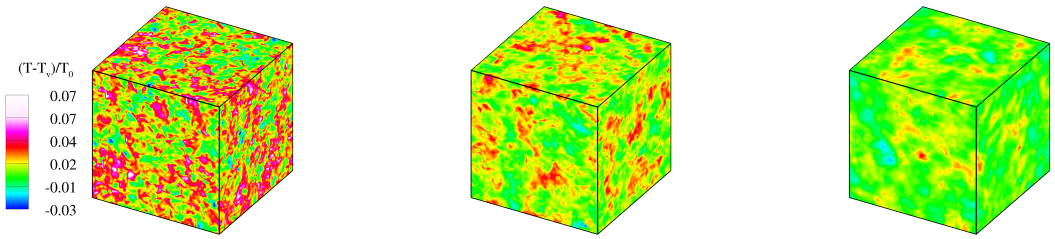

(a) Near early time. (b) Middle time. (c) Near ending time.

Figure 5.2: Difference of translational and vibrational temperature normalized by the initial temperature at various times. Note that the scale is the same between the three contour plots.

incompressible energy modes are examined.

5.4 Investigation of Turbulent Tuning Parameter

The effect of Da_v on the fluctuating quantities was examined by varying the vibrational relaxation time. Several Da_v were simulated, ranging from 0.125 to 64 for $M_t = 0.5$; the specific Da_v and associated relaxation time constants are given in Appendix D. As Da_v increases, the computational cost of the simulation increases as well, as resolving τ_{vib} requires smaller and smaller timesteps. All cases presented in this section have $Re_\lambda = 72$ and $M_t = 0.5$. The case of $Da_v = 0.25$ is the original, unmodified Camac rates.

In the previous section, results were presented comparing cases with and without vibrational energy relaxation. This comparison is between two cases with different total energies. A more appropriate comparison would be between cases which all have the same total energy. For this reason, a case with $Da_v = 0$ is used as the reference instead of a case without vibrational energy relaxation. A Da_v of zero is achieved by setting τ_{vib} to an extremely large value (order years). The results from $Da_v = 0$ are identical to the case without vibrational relaxation, as the vibrational energy pool is isolated from the other energy pools. Vibrational energy essentially behaves as a conserved scalar in this case.

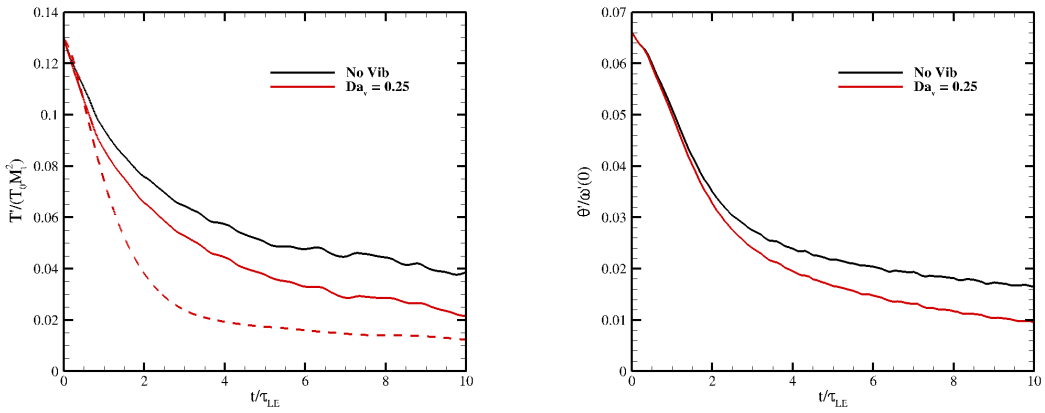

(a) Temperature fluctuations.

(b) Dilatational fluctuations.

Figure 5.3: Time histories of temperature and dilatational fluctuations with and without vibrational relaxation. $Re_\lambda = 72$, $M_t = 0.5$.

At this Re_λ and M_t, eleven different Da_v were simulated, including the zero case. In order to reduce clutter on the plots and clearly see the trends, only four representative cases are shown. The remaining cases lie within the bounds set by the optimally damped case and the zero case.

Temperature and pressure fluctuations are shown in Fig. 5.4 for four different Da_v. At low Da_v, the frozen case is approached and very little energy is transferred between vibrational and translational modes, and the interaction between modes is minimal. As Da_v increases, more energy is transferred and the fluctuations are damped. For high Da_v, the equilibrium case is approached as the translational and vibrational energy modes transfer energy at faster rates. This is seen in the fluctuating temperatures for $Da_v = 33$, where the solid (T') and dashed (T'_v) lie nearly on top of each other. Minimal damping, although not entirely obvious in the temperature fluctuations, appears to occur for $Da_v = 2$, especially at later times. At early times, energy is transferred into the vibrational mode at a faster rate for higher Da_v, and the temperature fluctuations are smaller.

While the minimal damping point of the temperature fluctuations is not clearly

obvious, the minimal damping point in pressure fluctuations is. As Da_v increases from 0.25 to 2, the pressure fluctuations are damped. Further increase from 2 to 32 results in an increase in fluctuating pressure, clearly indicating an optimal damping point. For $Da_v = 32$, the pressure fluctuations have nearly the same values as the $Da_v = 0$ case.

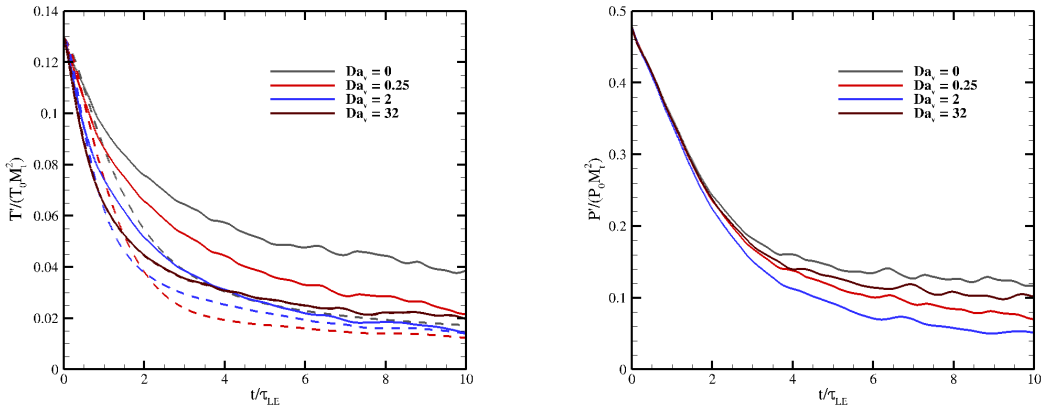

(a) Temperature fluctuations.

(b) Pressure fluctuations.

Figure 5.4: Time histories of temperature and pressure fluctuations with four different Da_v.

The fluctuation dilatation is shown on the left in Fig. 5.5 for the four Da_v cases. Shown on the right is the dilatational values for a non-dimensional time of five as a function of Da_v. In this image, all ten Da_v cases ($Da_v = 0$ not included) are given by the line, with colored symbols corresponding to the cases shown on the left. As with the pressure fluctuations, the dilatational fluctuations are damped from $Da_v = 0.25$ to 2, and increase from 2 to 32. This is expected, as pressure fluctuations are driven by acoustic fluctuations. This optimal damping point is clearly evident in the image on the right over all Da_v cases.

5.4.1 Turbulent Mach Number

The effect of M_t on this optimal damping point is examined for $M_t = 0.1$ and 0.3. Pressure fluctuations are shown in Fig. 5.6 for each case at various Da_v. The effect of

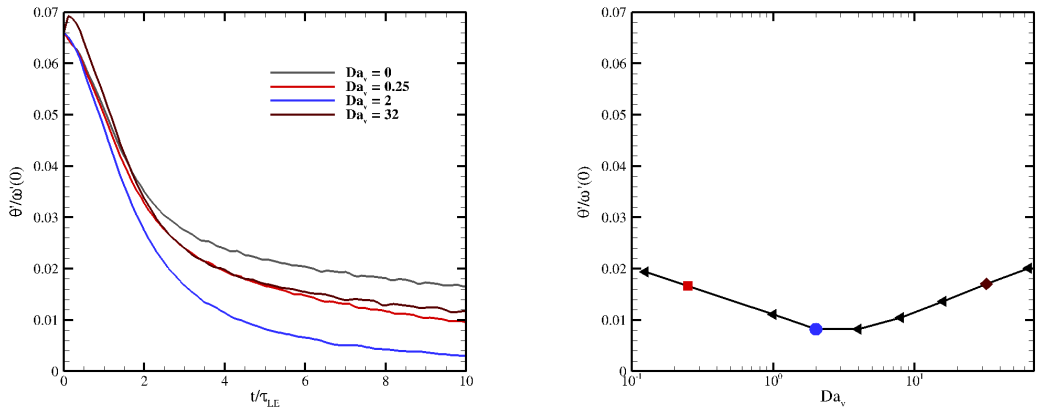

(a) Dilatational fluctuations.

(b) Dilatational fluctuations at $t/\tau_{LE} = 5$.

Figure 5.5: Time history of dilatational fluctuations on the left for four different Da_v. Dilatational fluctuation vs Da_v for a specific time showing all Da_v cases (colored symbols correspond to cases in left image).

vibrational relaxation is clearly reduced as the compressibility (M_t) is reduced. This indicates that energy is primarily transferred through compressible actions. At $M_t = 0.3$, the optimally damped case is $Da_v = 3.33$. While not clearly visible, the optimally damped case is $Da_v = 10$ for $M_t = 0.1$.

One further observation can be made at this point. For the higher M_t cases (0.3 and 0.5), waves are observed in the fluctuating quantities, driven by acoustic propagation. As Da_v increases to the optimal damping point, the waves decrease in magnitude, indicated by smoother lines. The waves increase in magnitude again as Da_v is further increased. This provides further evidence that the energy exchange is coupled with an acoustic process.

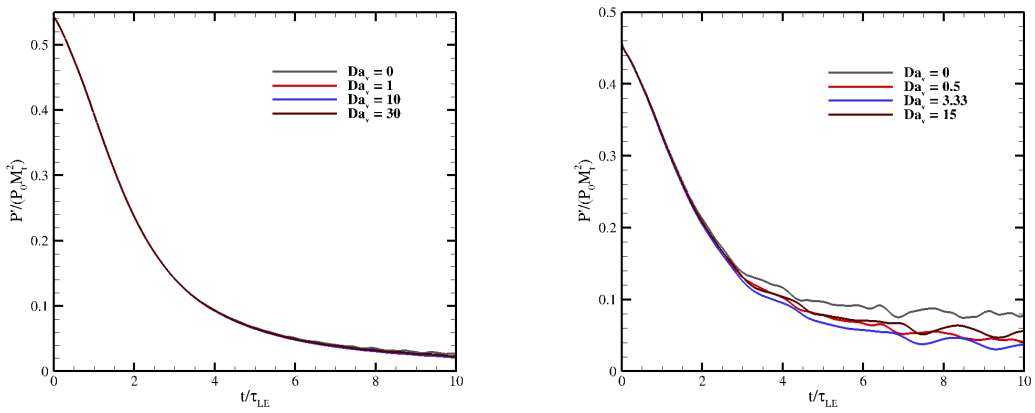

(a) $M_t = 0.1$. (b) $M_t = 0.3$.

Figure 5.6: Time histories of pressure fluctuations at different Da_v for $M_t = 0.1$ and 0.3.

5.4.2 Optimal Damping

In all three M_t cases presented above, optimal damping points occur when Da_v is on the order of the inverse M_t. We can define an acoustic time scale, τ_c, as

$$\tau_c = \frac{L_I}{c}. \tag{5.11}$$

Recalling the definitions of τ_{LE} and M_t, Eqs. 5.6 and 5.4 respectively, we can cast M_t as the ratio of τ_{LE} and τ_c ($M_t = \tau_{LE}/\tau_c$). Using this definition of M_t, taking the optimal Da_v to be order M_t^{-1}, we find damping is greatest when $\tau_{vib} \simeq L_I/c = \tau_c$. In other words, the vibrational relaxation rate is tuned to the turbulent flow-field when the vibrational relaxation time is of the order of the large scale acoustic time, and is an acoustic or dilatational process. The slower frequencies containing the most energy are optimally damped.

One interpretation of the underlying physics of this tuning process is given by considering acoustic wave simulations using the formulation from Chapter 4. Acoustic waves in a static gas, CO_2, are simulated at various frequencies. The simulations fixed $T = 1000\,\mathrm{K}$ and $\rho = 0.1\,\mathrm{kg/m^3}$, and varied the frequency. The numerical setup and grid

is retained from the previously described simulations.

Figure 5.7 shows the fluctuating temperatures for a frequency which is optimally tuned with the vibrational relaxation time ($f \simeq \tau_{vib}^{-1}$), a lower frequency, and a higher frequency. Interestingly, the higher frequency is damped more quickly than the optimal frequency. This seems to contradict the kinetic theory results from the previous chapter. However, these results are given in terms of damping *per wavelength*, and not total integrated damping over a domain. The damping rate is reduced for the higher frequency case, but the shorter wavelength increases the number of peaks in the domain to the point where the total integrated damping over the domain is increased. The lower frequency is damped significantly more slowly compared to the optimal and higher frequencies.

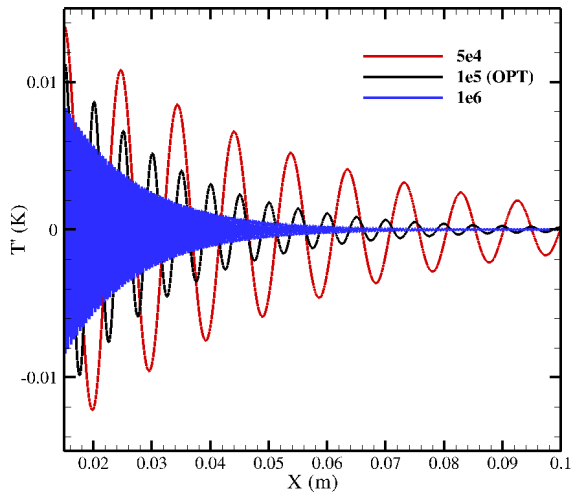

Figure 5.7: Acoustic wave in CO_2 for three different frequencies. The frequencies corresponds to an optimally damped wave, a slower wave, and a faster wave. Thermodynamic properties are maintained between simulations and the frequencies are varied.

In turbulent flows, the tuning parameter was related to the integral length scale of the flow, indicative of the lower frequencies. These lower and more energetic frequencies are optimally damped, and the higher frequencies are still damped, just not optimally.

As the relaxation time moves away from the large-scale acoustic times, the lower and more energetic frequencies are less damped, and much less energy is absorbed from the fluctuations. This is further examined by looking at the components of the kinetic energy, and is discussed in the next section.

5.5 Spectral Interaction of Energy Modes

5.5.1 Velocity Decomposition

Further insight into the tuning of the vibrational relaxation rate to the turbulent flow-field is gained by decomposing the velocity field into incompressible and compressible components. This is done via a Helmholtz decomposition, described in full detail in Appendix C. For the isotropic turbulence cases studied here, we can use the spectral equations developed by Moyal[43] for the decomposition as periodic boundaries are used in all directions. The results presented in this section are for $M_t = 0.5$ and $Re_\lambda = 72$.

5.5.2 Decomposed Kinetic Energy Spectra

The decomposed shell-averaged components of the kinetic energy spectra are given in Fig. 5.8 for three different times. The incompressible energy spectra are approximately two orders of magnitude larger than the compressible spectra, containing most of the turbulent kinetic energy. Vortical motion is contained within the incompressible energy mode, and compressions and expansions are contained within the compressible mode. The increase in compressible energy at the highest wavenumbers can be attributed to aliasing errors. At all times, the incompressible energy spectra are indistinguishable between all Da_v cases.

The compressible energy spectra, however, are affected by Da_v. The magnitudes and the shape are changed by varying the vibrational relaxation rate. For the early time, only the $Da_v = 2$ case shows any significant change from $Da_v = 0$. At later times, the compressible energy for the slower vibrational case, $Da_v = 0.25$, is reduced in magnitude while maintaining a similar shape compared to the zero case. The vibrational relaxation time is not tuned to any frequency of the turbulent flow-field; the frequency which would be in tune to this relaxation time would be off the plot on the left side.

As the vibrational relaxation rate increases and becomes tuned with the frequencies on the plot, the magnitude and the shape of the compressible spectra are altered.

The underlying physical mechanism discussed in Fig. 5.7 is evident in the shape change of the spectra for all three cases. The slowest relaxation time is lower than the frequencies of the turbulence, and the higher frequencies are all damped equally. For the fastest relaxation time, the lower frequencies are not damped at all, and the frequencies which are higher than the inverse relaxation time are damped. At the optimally damped condition, the relaxation time is in tune with the largest wavelength and the portion of the compressible energy containing the most energy is damped the most. The higher frequencies are also damped, so that the entire compressible energy spectrum is reduced.

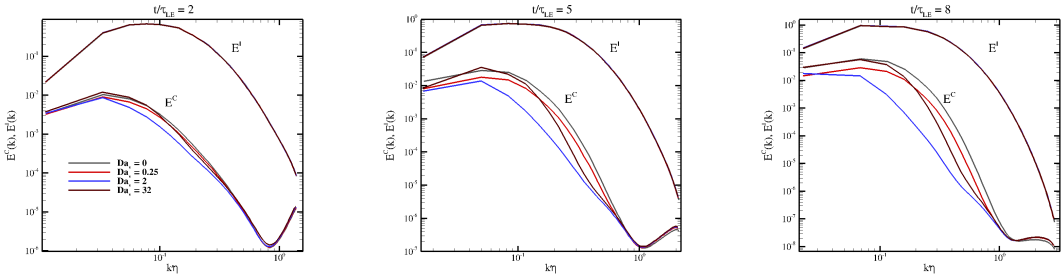

(a) $t/\tau_{LE} = 2$. (b) $t/\tau_{LE} = 5$. (c) $t/\tau_{LE} = 8$.

Figure 5.8: Decomposed kinetic energy spectra at 3 different times.

The relative compressible energy ratio, χ, defined as

$$\chi = \frac{\int E^C(k)dk}{\int (E^I(k) + E^C(k))dk} \tag{5.12}$$

is shown in Fig. 5.9. Small values of χ indicate low amounts of compressibility, and show that the kinetic energy is virtually unchanged due to vibrational energy relaxation absorbing energy from only the compressible energy component. The optimally damped case is again clearly evident, as χ is approximately constant throughout the entire simulation. As the turbulence decays, vorticity is dissipated while acoustic motion is only dissipated through absorption of energy into the vibrational mode. For cases with low vibrational energy transfer, the compressible energy portion increases relative to

the incompressible component, indicated by increasing values of χ in Fig. 5.9. In the optimally damped case, χ is constant, meaning the ratio is maintained, and indicates the rate of absorption of the acoustic energy is similar to the dissipation of vorticity.

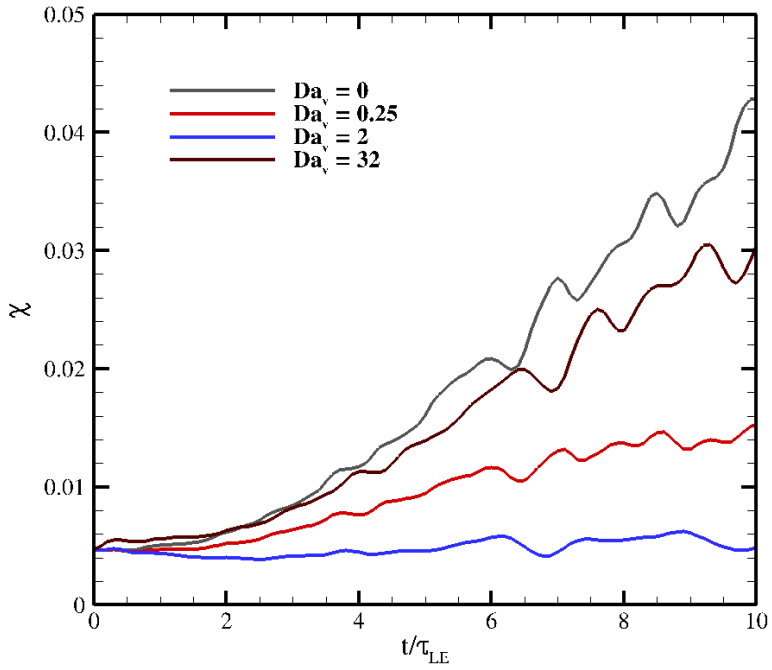

Figure 5.9: Time history of the compressible energy ratio.

5.5.3 Spectral Damping of Compressible Energy

The shape change of the compressible energy spectra in Fig. 5.8 is examined further by extracting data at five different wavenumbers. A measure of the damping compared to the reference Da_v case is computed as $1 - E^C(k)/E^I(k)$; values near zero represent no damping and as values near one, damping increases. These values are plotted as a function of Da_v in Fig. 5.10, for all Da_v cases, with each case represented as a symbol. Each wavenumber peaks at a different location of Da_v, with the peaks shifting towards

higher Da_v in time.

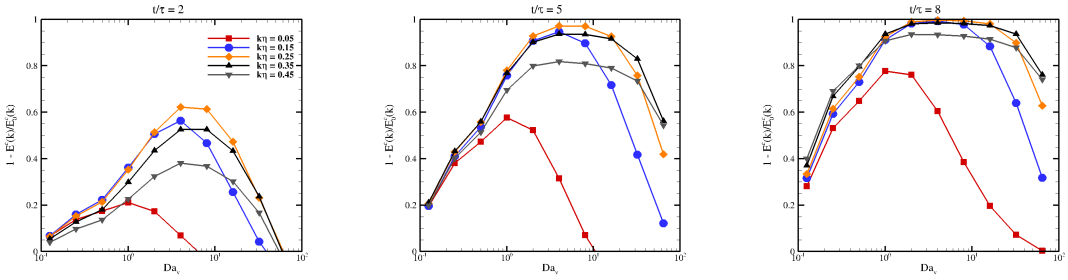

(a) $t/\tau_{LE} = 2$. (b) $t/\tau_{LE} = 5$. (c) $t/\tau_{LE} = 8$.

Figure 5.10: Compressible energy spectra values at specific wavenumbers vs Da_v for 3 different times. Each Da_v case is represented by a symbol.

The plots in Fig. 5.10 are collapsed by relating the vibrational relaxation time to an acoustic time scale of the given frequency. This relation is computed as

$$\omega\tau_{vib} = ka\tau_{vib}, \tag{5.13}$$

where ω is an angular frequency and k is a dimensional wavenumber. Figure 5.11 shows the results of the data from the specific wavenumbers as a function of $\omega\tau_{vib}$. The peaks for each wavenumber all collapse around one, and wavenumber specific damping is evident when the vibrational relaxation time is in tune with the acoustic time scale associated with the frequency.

5.6 Effects of Re_λ

The final section of this chapter is concerned with determining the effects of Re_λ on the conclusions obtained earlier. Simulations using $Re_\lambda = 175$ and $M_t = 0.5$ are presented here. Temperature, pressure, and dilatational fluctuations at four different Da_v are shown in Fig. 5.12. As observed in the lower Re_λ cases, optimal damping occurs when Da_v is on the order of the inverse M_t.

Decomposed spectra for the higher Re_λ case are shown in Fig. 5.13 at a given time. Again, similar conclusions are drawn from the lower Re_λ case. A Re_λ effect on the

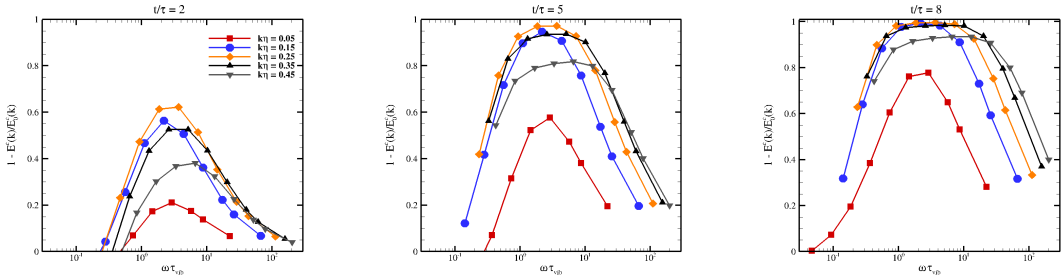

(a) $t/\tau_{LE} = 2$. (b) $t/\tau_{LE} = 5$. (c) $t/\tau_{LE} = 8$.

Figure 5.11: Compressible energy spectra values at specific wavenumbers vs $\omega\tau_{vib}$ for 3 different times. Here, ω is defined using an acoustic time scale.

exchange of energy between turbulent and vibrational modes has not been observed for the cases considered here.

5.7 Conclusion

DNS of compressible isotropic turbulence with vibrational energy relaxation were studied in this chapter. A vibrational Dahmköhler number was defined to relate the vibrational time scale to a turbulent time scale. The controlling parameters for isotropic flow were defined and varied, along with Da_v to understand how vibrational energy interacts with the turbulent flow.

Energy exchange mechanisms between kinetic and vibrational energies were discussed. There is no direct mechanism of energy transfer; energy must be exchanged through the translational-rotational mode. Viscous dissipation transfers turbulent kinetic energy into the translational-rotational mode, which is then transferred into the vibrational mode through w_v in Eq. 2.3. In addition, turbulence generates fluctuations in the thermal state, and acoustic waves are generated through compressions and expansions. These fluctuations result in an imbalance of energy between the translational-rotation and vibrational modes, and energy is again transferred through w_v. Vibrational energy has a damping effect on fluctuating quantities, as energy is distributed over a broader spectrum of energy states.

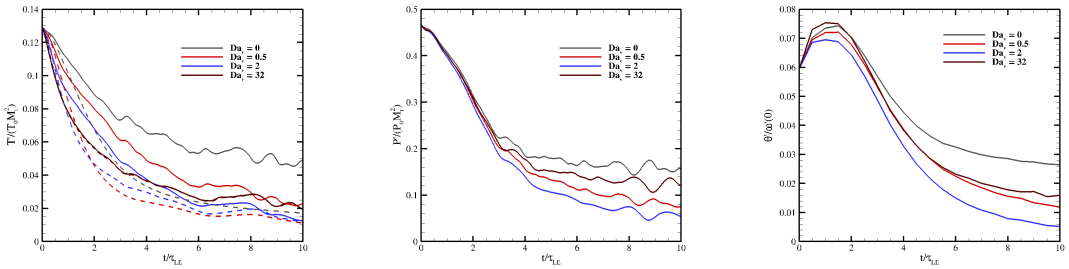

(a) Temperature fluctuations. (b) Pressure fluctuations. (c) Dilatational fluctuations.

Figure 5.12: Thermodynamic and dilatational fluctuations for various Da_v. $Re_\lambda = 175$, $M_t = 0.5$.

The tuning of the vibrational relaxation rate to the turbulent flow-field was investigated by varying Da_v. Optimal damping was observed when the vibrational relaxation time was on the order of the large-scale acoustic time scale. These results were consistent as M_t was varied, and were more pronounced for higher M_t, where compressibility is higher. The velocity field was decomposed into compressible and incompressible energy components. The incompressible energies were unaffected by vibrational energy, and were much larger than the compressible components. Vibrational energy absorbs energy from the compressible component, and wavenumber specific damping was observed when the acoustic time scale of the frequency was on the order of the relaxation time. Since vibrational energy acts on the turbulent kinetic energy through the compressible component, the effect on turbulence is weak due to the energy disparity between the incompressible and compressible components.

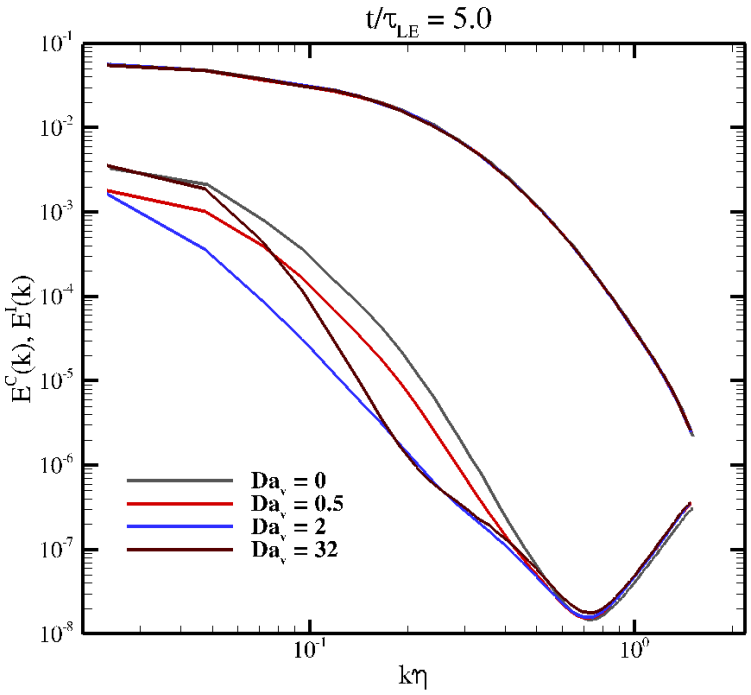

Figure 5.13: Compressible and incompressible spectra at $t/\tau_{LE} = 5$. $Re_\lambda = 175$, $M_t = 0.5$.

Chapter 6

Turbulent Shear Layer

Isotropic flows are ideally suited to fundamentally study the energy exchange mechanisms between turbulent and vibrational energies. However, the nature of isotropic turbulence means all turbulent fluctuations decay to zero. In addition, direction dependent length and time scales are non-existent. The findings of the previous chapter are generalized to a more complex turbulent shear flow.

Specifically, DNS of turbulent shear flows in a temporally evolving mixing layer are presented. Low compressibility simulations of isotropic turbulence, characterized by M_t, showed relatively small effect of vibrational relaxation on turbulence. This makes sense, as vibrational relaxation was observed to act on the turbulent flow through the compressible component of the velocity. Highly compressible (high-speed) turbulent shear flows are therefore simulated.

A description of the shear flow initialization is outlined, and the characteristic features of the turbulent flow are presented. The simulation methodology is given, and numerical requirements are addressed. In particular, at high M_c numerical dissipation is required, and must be added in a careful manner to avoid increased artificial mixing. Results are then presented for two different high-speed flows, and conclusions are discussed. Tuning of the vibrational relaxation rate to the turbulent shear flow is investigated by varying a defined Da_v. Energy exchange mechanisms are examined by decomposing the flow into compressible and incompressible energy modes. Finally, the conclusions are compared and contrasted to the results of the previous chapter.

6.1 Flow Initialization

The initialization of the turbulent shear flow simulations is based on the methodology used by Pantano and Sarkar[44]. Evolution of the turbulent flow-field is highly dependent on the initial conditions. Careful consideration and calculation of the initial quantities is required to ensure meaningful results are obtained. The framework of the initialization methodology is provided here, and further details can be found in Appendix B.

6.1.1 Initial Conditions

Temporally evolving shear layers are initialized with equal and opposite velocity streams in the top and bottom of the domain, drawn schematically in Fig. 6.1. The initial mean velocities were set to a hyperbolic profile in the streamwise direction, and to zero in the spanwise and transverse directions.

$$\overline{u}(z) = \frac{\Delta u}{2} \tanh\left(-\frac{z}{2\delta_\theta}\right), \quad \overline{v} = \overline{w} = 0 \tag{6.1}$$

where Δu is the velocity difference between the top and bottom streams. The gas is CO_2, the temperature is set to 800 K, and the density is $1\,\mathrm{kg/m^3}$. The mean thermodynamics are initially constant throughout the domain.

The compressibility of the flow is characterized by the convective Mach number, M_c, as

$$M_c = \frac{\Delta u}{c_1 + c_2} \tag{6.2}$$

where c_1 and c_2 are the mean speeds of sound for the two streams. This definition is valid only for streams with the same specific heat ratio[45, 46], as is the case in this work. Two different M_c values were used to study vibrational relaxation effects: 0.7 and 1.1. These represent flows with high levels of compressibility; a third case using $M_c = 0.3$ was used in validating the initialization and simulation methodologies, but was not considered for flows with vibrational non-equilibrium due to low compressibility.

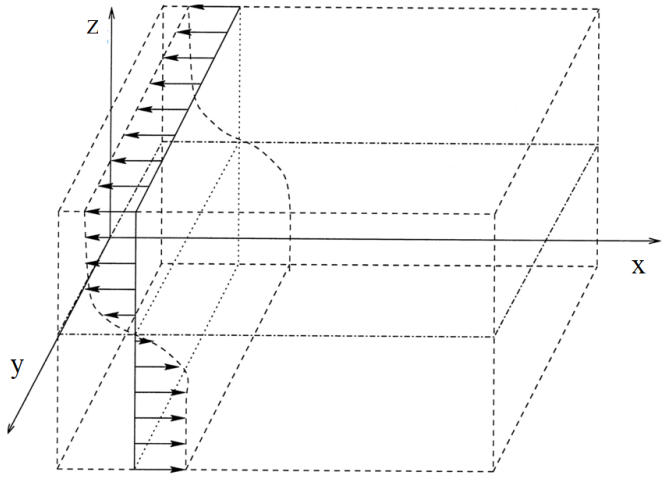

Figure 6.1: Flow schematic of the temporally evolving shear layer.

The Reynolds number characterizing the flow was specified using the initial momentum thickness (δ_θ) as

$$Re_{\theta,0} = \frac{\Delta u \overline{\rho} \delta_{\theta,0}}{\overline{\mu}} \tag{6.3}$$

where the initial mean values are used for density and viscosity. The viscosity is computed using Blottner curve fits. The initial Re_θ was set to 160 for all simulations.

The transition to turbulence is accelerated by introducing broadband fluctuations in velocity and thermodynamic quantities to the mean fields. Random velocity fluctuations are generated with an imposed isotropic turbulent energy spectrum,

$$E(k) = \frac{k}{k_0}^4 \exp\left[-2\left(\frac{k}{k_0}\right)^2\right], \tag{6.4}$$

where k_0 is the peak wavenumber, specified to have 48 peak wavelengths in the streamwise direction. These fluctuations are limited to the extent of the initial shear layer thickness by an exponential decay. Limiting the fluctuations in this way introduces compressibility in the flow-field. Erlebacher et al.[47] demonstrated that quasi-incompressible fluctuations minimized compressibility transients. The compressible component of the initial velocity field is therefore removed. The initial turbulent intensity was set to 10%.

Thermodynamics are then specified by obtaining pressure fluctuations from the Poisson equation. Density is then determined assuming an isentropic equation of state. Finally, the temperature is set from the ideal gas law. Vibrational energies are initially turned off. Full details on calculating these fluctuations are given in Appendix B.

6.1.2 Shear Layer Characteristics

The characteristic turbulent flow time is determined from the velocity difference and momentum thickness as,

$$\tau_\theta = \frac{\delta_\theta}{\Delta u}. \tag{6.5}$$

The momentum thickness is computed from

$$\delta_\theta = \frac{1}{\rho_0 \Delta u^2} \int_{-L_z/2}^{L_z/2} \overline{\rho}(\frac{1}{4}\Delta u^2 - \tilde{u}^2) dz. \tag{6.6}$$

Favre-averaged quantities are denoted with a tilde, with the form

$$\tilde{\phi} = \frac{\overline{\rho\phi}}{\overline{\rho}} \tag{6.7}$$

and Reynolds quantities are denoted with a bar. Quantities are plane-averaged in the homogeneous directions (x and y).

Experimental studies have shown that turbulent shear layers achieve a self-similar state after an initial transient[46, 48, 49]. This self-similar state is characterized by a constant growth rate and a collapse of averaged flow quantity profiles in the homogeneous directions. Achieving self-similar states in DNS has often been difficult in the past due to the limitations of computational resources on grid requirements. However, as computational resources improve, these limitations have decreased and more accurate DNS results are obtained[50, 51, 44].

In these simulations, an initial transient time is observed as the initial shear layer becomes unstable and breaks down. An approximate self-similar state is achieved, and the simulation is stopped. This time was $t/\tau_{\theta(0)} = 420$ for $M_c = 0.7$, and 510 for $M_c = 1.1$. At this time, vibrational energy relaxation was introduced by setting $T_v = T$.

The vibrational Dahmköhler number was defined in the previous chapter relating a turbulent motion rate to the vibrational relaxation rate. For isotropic turbulence,

the large-eddy-turnover was used (Eq. 5.10). In shear flows, the universal small-scale energy range is still contained within the turbulent energy, but the range is extended by larger structures containing more energy. These turbulent structures are defined by the shearing action of the flow, and are functions of spatial direction.

Tuning was observed in isotropic turbulence when the acoustic time scale ($\tau_c = L_I/c$) was on the order of the vibrational relaxation time. Energy exchange was shown to be coupled to the acoustic modes, and as we expect a similar mechanism in shear flow, the acoustic wave speed is used to define a turbulent motion rate. The choice of length scale used to define the turbulent rate is less obvious, but is expected to be related to a large-scale structure. This is based on the discussion in Section 5.5.2, where the largest energy containing wavelength was optimally damped.

Several large-scale and integral length scales can be defined for shear turbulence. The two most commonly used parameters to measure the thickness of a shear layer, and therefore a measure of the largest scales, are the momentum and vorticity thicknesses. The momentum thickness was previously defined in Eq. 6.6, and the vorticity thickness is defined as

$$\delta_\omega = \frac{\Delta u}{(\partial \tilde{u})/\partial z)_{\max}} \tag{6.8}$$

In addition to these thicknesses, integral length scales can also be defined as

$$l_x = \frac{1}{\overline{u^2}} \int_0^{L_x/2} \overline{u(x,y,z,t)u(x+r,y,z,t)} dr, \tag{6.9}$$

$$l_y = \frac{1}{\overline{u^2}} \int_0^{L_y/2} \overline{u(x,y,z,t)u(x,y+r,z,t)} dr. \tag{6.10}$$

After varying τ_{vib} and relating the relaxation time to the different scales, the momentum thickness was determined as the relevant length scale. These results are discussed below, but the definition of Da_v is given here as

$$Da_v = \frac{\delta_\theta/\overline{c}}{\tau_{vib}}, \tag{6.11}$$

where $\overline{c}$ is the average speed of sound in the volume of the shear layer bounded by the momentum thickness. In the cases presented below, Da_v is given by the conditions when vibrational energy is activated. The vibrational relaxation time is modified in the

same way as in the isotropic turbulent cases, and is described in Appendix D along with the constants used in these cases. Across the turbulent core of the shear layer, τ_{vib} is approximately constant, as seen in Fig. 6.2, and is taken as the average in the region bounded by the momentum thickness.

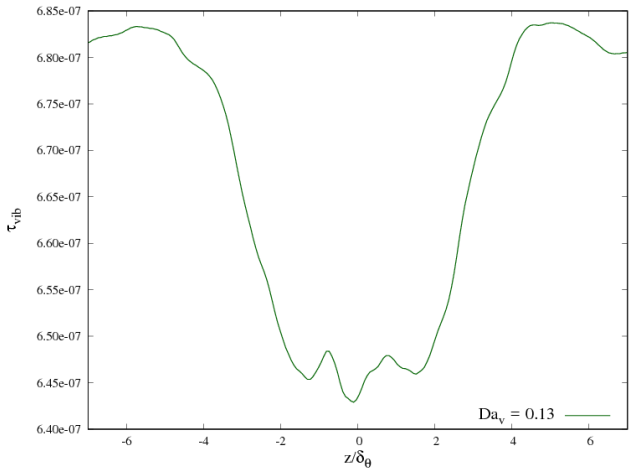

Figure 6.2: Averaged profile of instantaneous τ_{vib} for the unmodified Da_v case.

6.2 Simulation Details

The simulation methodology is presented below, and is mostly similar to the simulation details presented in the previous chapter with a few key differences. First, the numerics and the flow solver are described. The flow domain and boundary conditions are then provided. Table 6.1 lists the flow and domain parameters. Validation of the initial conditions and numerics is provided in Appendix B.

6.2.1 Numerics

DNS of compressible turbulent shear layers are obtained using the US3D flow solver[20]. The sixth-order kinetic energy consistent numerical scheme developed by Subbareddy

M_c	L_x, L_y, L_z	N_x, N_y, N_z	Da_v	l_x/L_x	l_x/L_x	η_{min}/Δ_x
0.7	$316.2, 79.0, 158.1$	$512, 128, 256$	0, 0.004, 0.07, 0.2, 0.6, 0.7, 1, 10	0.038	0.037	0.37
1.1	$318.7, 79.7, 159.4$	$512, 128, 256$	0, 0.13, 0.38, 0.53, 0.8, 1, 6.35, 25	0.036	0.029	0.43

Table 6.1: Summary of flow and domain parameters. The domain lengths are given in terms of the initial momentum thickness ($L_i/\delta_{\theta,0}$). Final length scale parameters are also given, where η_{min} is the minimum Kolmogorov scale across the shear layer.

and Candler[28] is used to approximate the convective fluxes. A central-based deferred-correction approach is used to evaluate the viscous fluxes. The solutions are advanced in time using a third-order Runge-Kutta method[29].

The flow parameters are summarized in Table 6.1. Two M_c cases are presented below: 0.7 and 1.1. In the lower compressibility case, $M_c = 0.7$, numerical dissipation is not required for stability. However, in the higher compressible case, $M_c = 1.1$, sufficiently strong shocks and gradients exist in the flow that dissipation is required. Dissipation is introduced to the central-based convective fluxes by adding a scaled upwinded portion of the flux (Eq. 3.19).

Ideally, dissipation is added only where needed, and so the Ducros switch was initially used. The switch values are determined by the local dilatation and vorticity, and range between zero and one. Within the turbulent core of the shear layer, where vorticity is large and the flow is mostly smooth, the switch works well. However, this is not the case in regions of high dilatation and low vorticity. Compressions and expansions generate acoustic waves, which propagate into the free-stream (defined in the top and bottom streams as zero vorticity). The location of the edge of the mixing layer also fluctuates in time, and a region of the grid contained within the shear layer at one time may not be at the next timestep. This leads to pockets and flipping of the Ducros switch between zero and one for successive timesteps in regions very near the edge of the shear layer, shown in Fig. 6.3. Adding dissipation in this fashion introduces large amounts of numerical dissipation and vorticity, and induces increased non-physical entrainment and growth rates. To avoid this, a constant value of $\alpha = 0.01$ is used in Eq. 3.19 for all cases where $M_c = 1.1$.

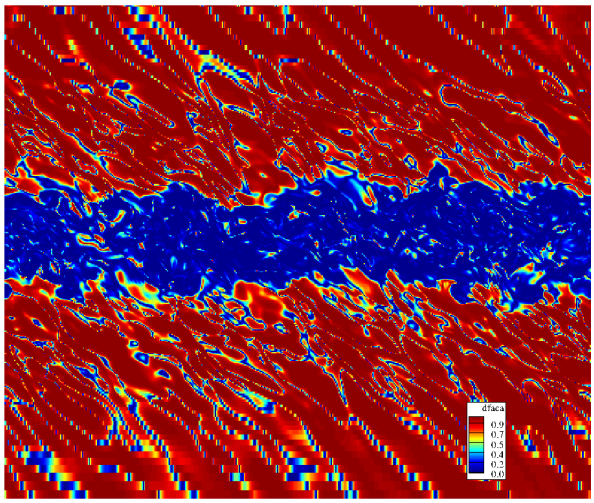

Figure 6.3: Contour plot of the Ducros switch for a turbulent shear flow. The turbulent core is in the center of the image, mostly represented by the blue region.

While using a constant α introduces numerical dissipation everywhere, the small value required to maintain stability should minimize non-physical effects. The effect of α on the solution was investigated using DNS of acoustic wave propagation and with simulations at $M_c = 0.7$. Using the acoustic wave propagation formulation described in Chapter 4, α was varied between 0 and 1. Figure 6.4 shows the translation-rotational temperature from cases without vibrational energy relaxation activated. The fluctuations are shown for $alpha = 0, 0.01, 1$ using second-order kinetic energy fluxes. An additional simulation using the modified Steger-Warming (MSW) scheme is also shown. Fourth and sixth-order fluxes were also used in these simulations, with no difference observed from the second-order case, and are therefore not shown. Very little difference is seen between the four cases, with some minor damping of the fluctuations for the $\alpha = 1$ and MSW case at the wave peaks. The $\alpha = 0.01$ case and the reference case ($\alpha = 0$) are virtually identical. Additional simulations with vibrational energy relaxation are not shown, as the damping of the fluctuations by vibration was significantly greater than the numerical dissipation. No difference in the acoustic damping rate was observed between values of α for the vibrationally active simulations.

To further quantify the effects of adding numerical dissipation, α was varied in DNS

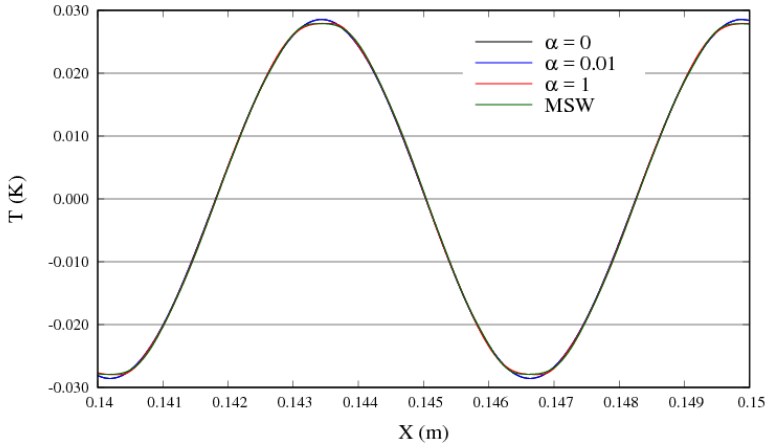

Figure 6.4: Comparison of translational-rotational temperature fluctuations from a propagating acoustic wave for different levels of dissipation and numerical scheme. Vibrational energy relaxation is turned off.

of temporally evolving shear layers without vibrational energy relaxation at $M_c = 0.7$. This lower compressible case does not require dissipation for stability, and therefore a reference case of $\alpha = 0$ can be used. Figure 6.5 shows the evolution of the momentum thickness for three different values of α: 0, 0.01, and 0.1. The difference between the reference case and $\alpha = 0.01$ is small, especially when compared with the 0.1 case. In the higher dissipation case, non-physical effects from the numerics clearly influence the solution as the shear layer grows at a faster rate. At $M_c = 1.3$, the minimum value of α required for stability was 0.1. Based on these investigations, we determined an α of 0.01 will provide acceptable solutions for $M_c = 1.1$, but higher M_c values were not studied due to the large amounts of dissipation required.

6.2.2 Flow Domain and Boundary Conditions

The flow domain used in all simulations is rectangular, with large lengths required to allow the turbulence to reach a self-similar state. Uniform grid spacing is applied in all directions. Grid convergence was checked by doubling the number of points in each direction. Periodic boundary conditions are applied in the streamwise and spanwise

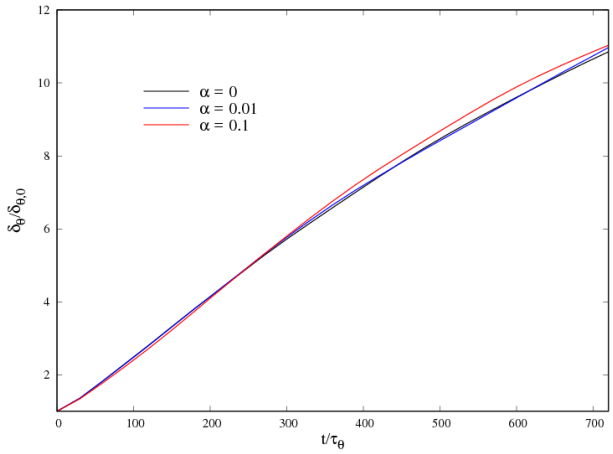

Figure 6.5: Momentum thickness history for three different values of dissipation at $M_c = 0.7$.

directions. The domain parameters are given in Table 6.1 with the flow parameters. Table 6.1 also gives final domain lengths. The integral length scales are much smaller than the total domain size, indicating the domain is large enough to not influence the shear layer at the end of the simulation. Additionally, velocity correlations converged to zero before the separation distance reached the half-domain size, reaffirming the adequate size of the domain.

Reflecting waves from boundaries can influence the growth rate of turbulent shear layers. Grids are grown at the top and bottom of the domain, with grid sizes quickly stretched in order to minimize wave reflections. The number of added grid points was fifty and the stretching ratio was 1.08 for all cases. Supersonic outflow boundary conditions are applied in the transverse direction. In addition, the dissipative portion of the convective fluxes are turned fully on ($\alpha = 1$ in Eq. 3.19) in the top and bottom stretched grids. The value of α is ramped up from the value within the domain to one over ten cells using a hyperbolic tangent profile. This is done to prevent a sharp increase in α between the domain containing constant cells and the cells grown at the top and bottom.

6.3 Results

Two sets of temporally evolving shear layer DNS were performed, $M_c = 0.7$ and $M_c = 1.1$. The main focus is on the higher compressible case, $M_c = 1.1$, based on the M_t study from isotropic turbulence, and most of the results presented are from these cases. At the end of the chapter, comparisons are made with the $M_c = 0.7$ case. The initial flow was simulated without vibrational energy relaxation, to allow the turbulence to reach a self-similar state. The momentum thickness is shown for each simulation in Fig. 6.6 as a reference. Validation cases comparing momentum thickness growth rate with previous studies are provided in Appendix B. Increasing the compressibility of the flow reduces the growth rate of the shear layer, and this is reflected in Fig. 6.6.

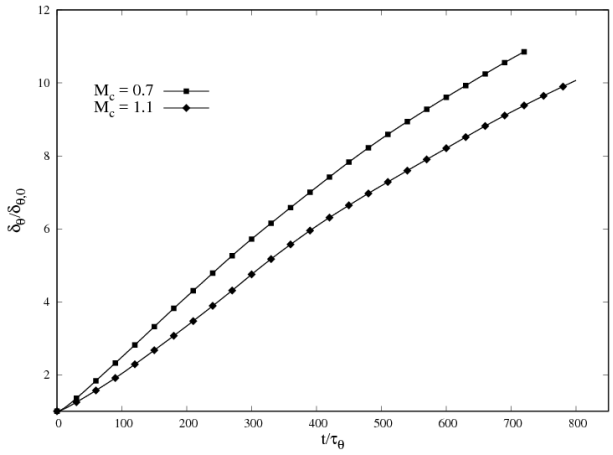

Figure 6.6: Evolution of momentum thickness with time for $M_c = 0.7$ and 1.1.

In the remaining sections of this chapter, the reference case is $Da_v = 0$. This allows us to compare simulations which have the same total energy, as we did in the previous chapter. The reference case matched the case vibrational energy relaxation turned off, as the vibrational energy cannot be exchanged and essentially acts as a conserved scalar.

6.3.1 Vibrational Relaxation

An instantaneous image showing isosurfaces of vorticity, contours of the difference in translation-rotational and vibrational temperatures, and the divergence of velocity is shown in Fig. 6.7. Initially, the vibrational temperatures are set equal to the translation-rotational temperatures, and any difference is generated by the turbulence. The flow consists of two regions, the turbulent core and the free-stream, beyond the edge of the shear layer where the vorticity is virtually zero. As seen in the exit plane on the right of Fig. 6.7, non-equilibrium exists in both the core and the freestream. The turbulence generates compressions and expansions, generating fluctuations in the thermal state. The vibrational energy lags behind these fluctuations, and energy exchange is driven by τ_{vib}. In the freestream, nonequilibrium is generated by acoustic waves, generated in the turbulent core, propagating away from the shear layer, seen in the divergence of velocity shown on the back plane of Fig. 6.7. While the focus here is on the turbulence, some interesting observations can be made about trends in the freestream, and are discussed in later sections.

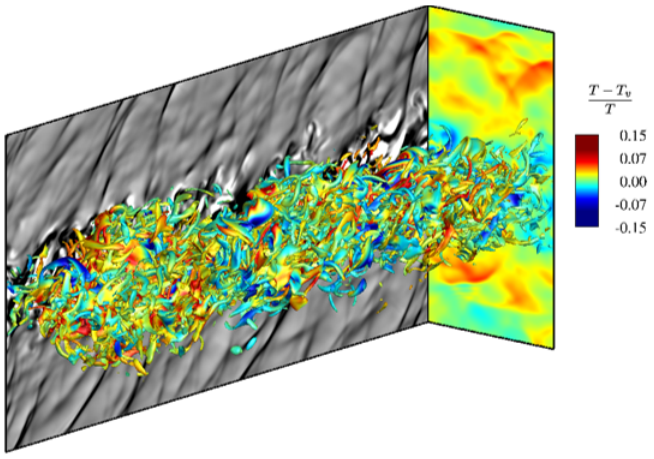

Figure 6.7: Instantaneous isosurface of vorticity ($\omega = 0.25\omega_{max}$) at $t/\tau_\theta = 600$ for $M_c = 1.1$. The isosurfaces and exit plane (right side of image) are colored by contours of the normalized difference in translational-rotational and vibrational temperatures. The back plane shows the instantaneous divergence of velocity. The flow is from right to left in the top half, and left to right in the bottom.

The flow is periodic in two directions, and flow quantities are averaged in these directions. Figure 6.8 gives mean temperature profiles at two different times for various Da_v. Not all Da_v cases are shown to keep plot clutter to a minimum and highlight trends; the full list of Da_v cases is given in Table 6.1. Initially, the flow is in equilibrium, and the mean translational and vibrational temperatures are equal. As viscous dissipation heats the flow, energy is transferred to the translational mode, and the vibrational energy lags behind. The largest difference between T and T_v occurs near the center of the shear layer. When Da_v is increased, the energies are driven towards equilibrium at a faster rate, and the mean temperature is reduced as energy is spread over a broader distribution.

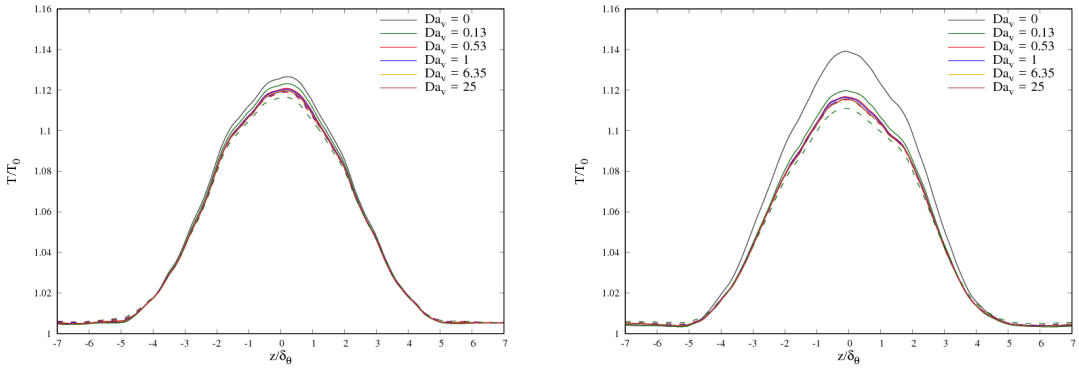

(a) $t/\tau_\theta = 570$. (b) $t/\tau_\theta = 780$.

Figure 6.8: Mean temperature profiles at two different times for $M_c = 1.1$ and varying Da_v. Solid lines represent T, and dashed T_v.

Fluctuating vibrational and translational temperatures are given in Fig. 6.9. The difference in fluctuating temperatures is generated through compressions and expansions of the gas. This is also observed in the freestream portion of the flow (beyond $z/\delta_\theta \approx \pm 5$, where the fluctuations are significantly reduced), where there is no viscous dissipation. The only driving force in this region is acoustic wave propagation. As with the mean flow, the largest region of nonequilibrium is at the center of the turbulent core, where the turbulence is the most intense, as expected. Increasing Da_v transfers energy into the vibrational mode faster (seen by increasing magnitudes of the dashed lines), and

has a damping effect on the fluctuating translation temperatures.

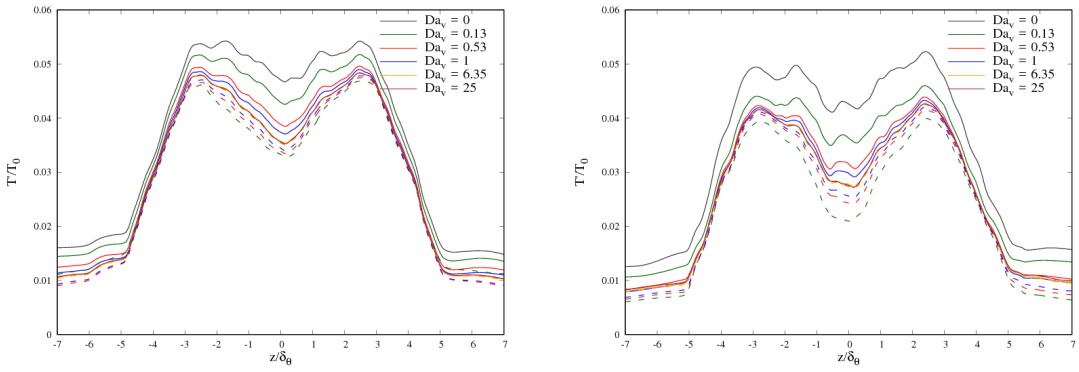

(a) $t/\tau_\theta = 570$. (b) $t/\tau_\theta = 780$.

Figure 6.9: Rms fluctuating temperature profiles at two different times for $M_c = 1.1$ and varying Da_v. Solid lines represent T', and dashed T'_v.

Figure 6.10 shows fluctuating dilatation profiles. The profiles are slightly damped in the turbulent core, but show significant increase as Da_v increases past one. This is not expected, based on the results from the isotropic turbulent simulations, where θ' was always damped from the reference case ($Da_v = 0$). The reasons for this are not fully quantified, but the vibrational time scale evidently interacts with the time scale of the dilatation in a positive (non-damping) way. Again, the freestream shows the acoustic waves propagating from the shear layer. The dilatation in the freestream is optimally damped for $Da_v = 1$ throughout the simulation.

The turbulent kinetic energy, k, is computed as

$$k = \frac{1}{2}\frac{\overline{\rho u_i'' u_i''}}{\overline{\rho}} \tag{6.12}$$

where u_i'' refers to the Favre averaged fluctuating velocity. For these cases, no meaningful difference is observed between Favre and Reynolds averaged quantities.

Turbulent kinetic energy profiles at a single time are given in Fig. 6.11. The difference between Da_v cases is non-existent, and does not change over the course of the simulations. This is expected, as previously discussed, there is no direct mechanism of

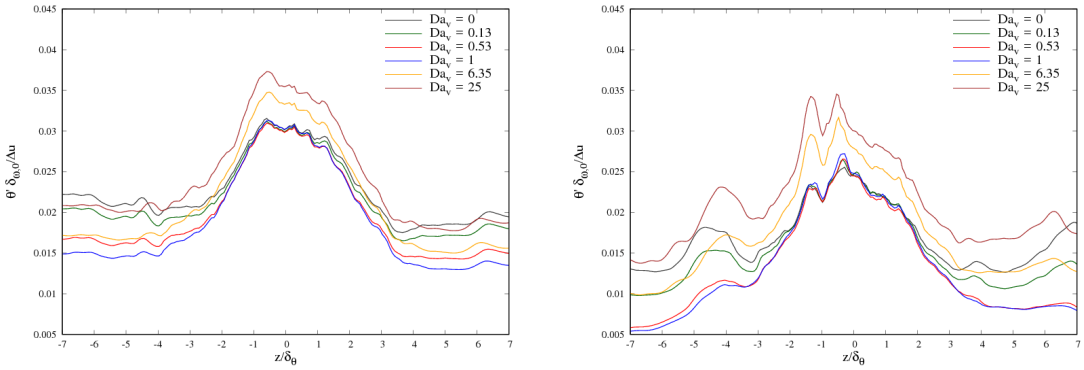

(a) $t/\tau_\theta = 570$. (b) $t/\tau_\theta = 780$.

Figure 6.10: Rms fluctuating dilatational profiles at two different times for $M_c = 1.1$ and varying Da_v.

energy exchange between kinetic and vibrational modes. Energy transfer occurs through compressible energy modes, and is quantified in the next section.

The momentum thickness is compared between Da_v cases in Fig. 6.12, and is largely unaffected by vibrational energy relaxation. This is consistent with the turbulent kinetic energy profiles. The momentum thickness is a measure of the large scale turbulent structures within the flow. Most of the kinetic energy is contained within the incompressible component of the velocity, and is largely unaffected by the vibrational energy. Unless the compressible energy is comparable in magnitude to the incompressible energy, we do not expect the growth of the shear layer to be significantly affected. Compressible energy can reach and even exceed the energy content of the incompressible mode in flows with large amounts of heat release (i.e. chemical reactions), and has been shown to influence the kinetic energy[4]. In vibrationally excited flows, heat release occurs when the mean vibrational and translational temperatures are in significant nonequilibrium. These types of flows are beyond the scope of this work.

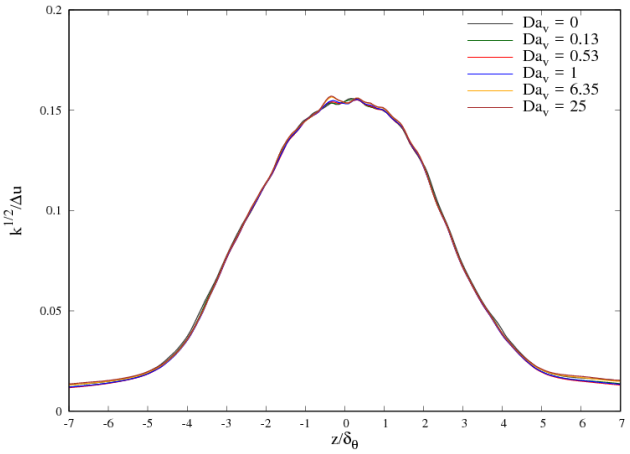

Figure 6.11: Turbulent kinetic energy profile at $t/\tau_\theta = 780$ for $M_c = 1.1$ and varying Da_v.

6.3.2 Optimal Damping

In isotropic turbulent flows, defining optimal damping is easier due to the isotropic nature of the flow, where all quantities are volume-averaged. For shear flow, two regions exist, where damping of quantities is different. This is seen in Fig. 6.10, where the freestream quantities are clearly tuned, but the tuning in the turbulent core is less obvious. Additionally, as the turbulence mixes the quantities, tuning may appear different for different regions of the flow. Examining quantities at the centerline gives mixed results in terms of tuning, and peak values change physical location between Da_v cases.

These issues are mitigated by taking volume averages of quantities only within the turbulent core. The bounds of these volume averages are set by the momentum thickness and the center of the shear layer is determined based on the mean velocity profile switching signs. Figure 6.11 shows the evolution of the volume averaged dilatational fluctuations. A clear trend is observed, with optimal damping occurring when Da_v is on the order of one. Da_v was previously defined using the momentum thickness and volume averaged speed of sound. These results indicate that the vibrational relaxation rate is tuned to the turbulent motion when τ_{vib} is on the order of the large-scale acoustic

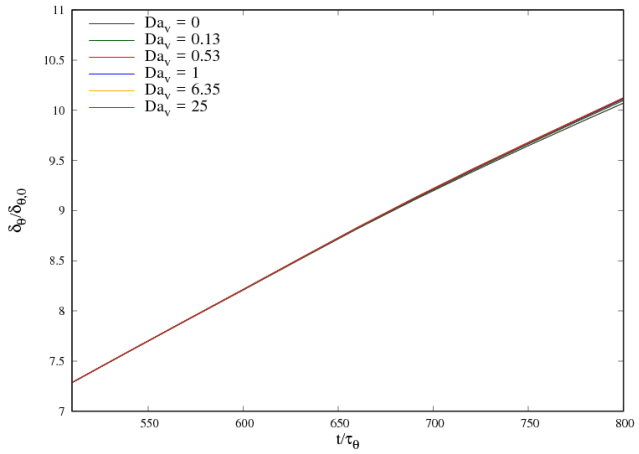

Figure 6.12: Time history of the evolution of momentum thickness for various Da_v and $M_c = 1.1$.

time scale. This is consistent with the tuning parameter observed in isotropic flow.

6.4 Compressible Mode Interaction

The kinetic energy of the flow was decomposed into compressible and incompressible components as described in Appendix C. The boundary conditions are periodic in only two directions. Poisson equations are used with eighth order methods to solve for the incompressible velocity, and the compressible velocity is obtained by subtracting the incompressible field from the full field. The quantities in the portion of the stretched grid at the top and bottom of the domain is neglected, and the boundary conditions of the Poisson solver are applied at the edge of the domain containing the constant cells. Figures 6.14 and 6.15 show streamwise and spanwise spectra at two different times. As expected based on the previous results, the incompressible energies are unaffected by vibrational energy relaxation. All of the action occurs in the compressible modes, which are significantly smaller than the incompressible modes, meaning the total kinetic energy of the flow is unaffected.

The compressible energy spectra display a dependence on Da_v. While some damping

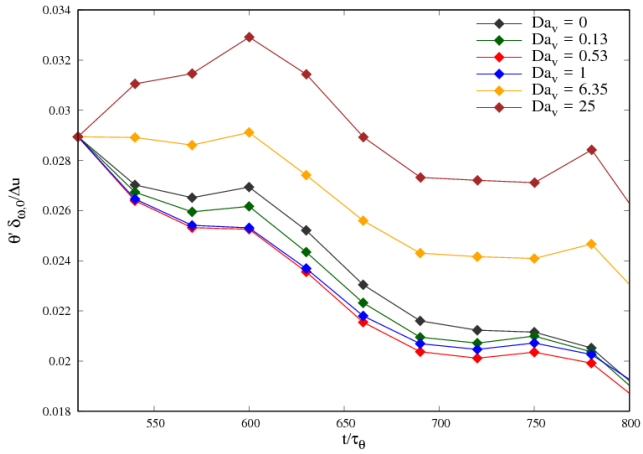

Figure 6.13: Evolution of fluctuating dilatation averaged in volume bounded by δ_θ in time, for various Da_v and $M_c = 1.1$.

occurs when Da_v is order one, the spectra are more significantly altered when Da_v is large. These alterations increase in time, and are consistent between streamwise and spanwise directions.

The wavenumber dependence clearly observed in isotropic flows is not as obvious in these cases. This dependence is examined by extracting data at different wavenumbers. The compressible values at each wavenumber are divided by the reference value at that wavenumber, and subtracted from 1. Additionally, the values are plotted as a function of $\omega\tau_{vib}$, defined as

$$\omega\tau_{vib} = \hat{k}\overline{a}\tau_{vib}, \tag{6.13}$$

where ω is the angular frequency, $\hat{k}$ is the dimensional wavenumber, and $\overline{a}$ is the volume averaged speed of sound. This is based on the results obtained in isotropic turbulence.

Extracted wavenumbers are plotted at four different times in Figs. 6.16-6.19 for all Da_v cases. The collapse of the values appears to fluctuate in time, and differ between streamwise and spanwise quantities. In the spanwise direction, the higher wavenumbers collapse better than the lower ones do. At $t/\tau_{vib} = 630$ and 780 the peaks collapse

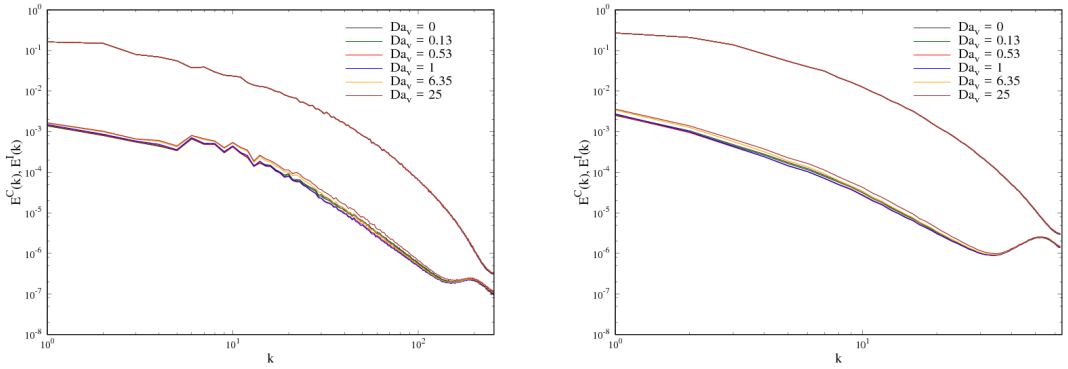

(a) Streamwise Spectra. (b) Spanwise Spectra.

Figure 6.14: Decomposed kinetic energy spectra in streamwise and spanwise directions at $t/\tau_\theta = 570$ for $M_c = 1.1$.

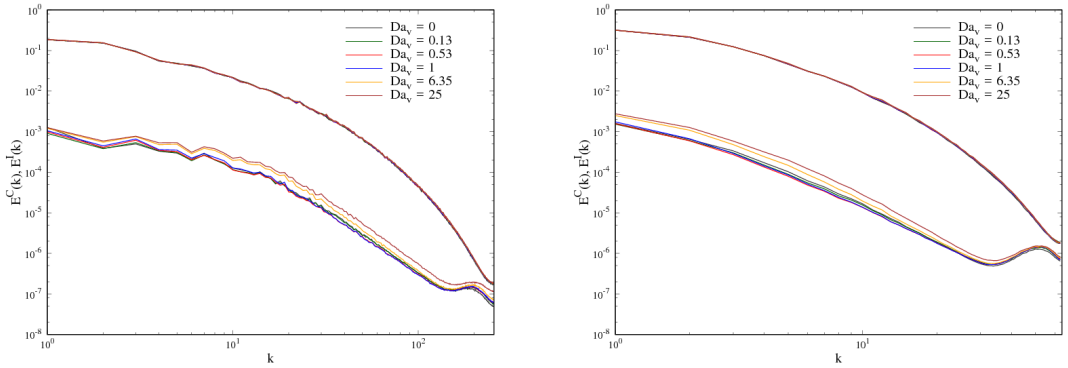

(a) Streamwise Spectra. (b) Spanwise Spectra.

Figure 6.15: Decomposed kinetic energy spectra in streamwise and spanwise directions at $t/\tau_\theta = 780$ for $M_c = 1.1$.

moderately well, whereas at the other two times the low wavenumbers are shifted to the left. The spanwise peaks display a shift in peaks from left to right with increasing k. The reasons behind this trend are not yet fully understood.

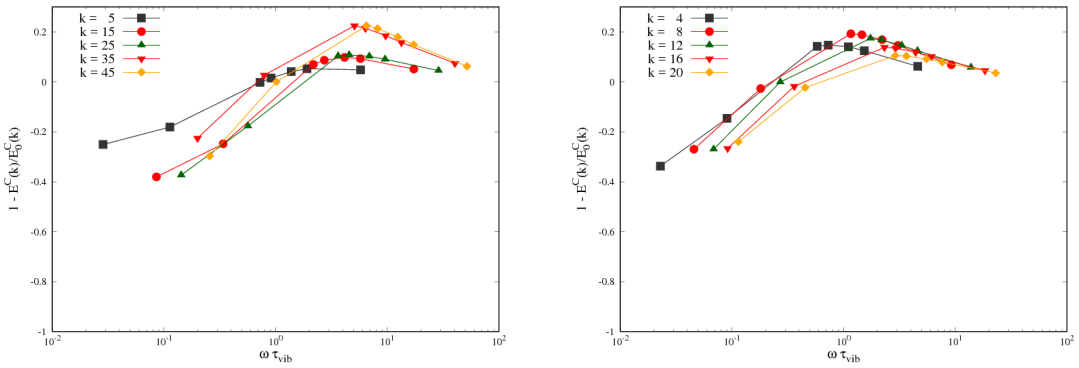

(a) Streamwise.

(b) Spanwise.

Figure 6.16: Decomposed compressible energy spectra at specific non-dimensional wavenumbers in streamwise and spanwise directions at $t/\tau_\theta = 570$ and $M_c = 1.1$.

6.5 M_c Effects

The effects of compressibility are examined by lowering M_c. Increasing values of M_c beyond 1.1 require significant amounts of dissipation, and are not necessary for understanding compressibility effects in the context of this work. Fluctuating temperatures are plotted in in Fig. 6.20 for two different times. The trends in the fluctuations are similar to the $M_c = 1.1$ case. Thermal nonequilibrium is greatest near the center of the shear layer, and translational temperatures are damped.

The momentum thickness, shown in Fig. 6.21, is virtually unaltered by Da_v, as in the higher compressible case. This trend is again reflected in the turbulent kinetic energies (not shown), which also show no observable difference. We expect these conclusions, since the compressibility is reduced, and this is consistent with lowering the M_t in the isotropic simulations.

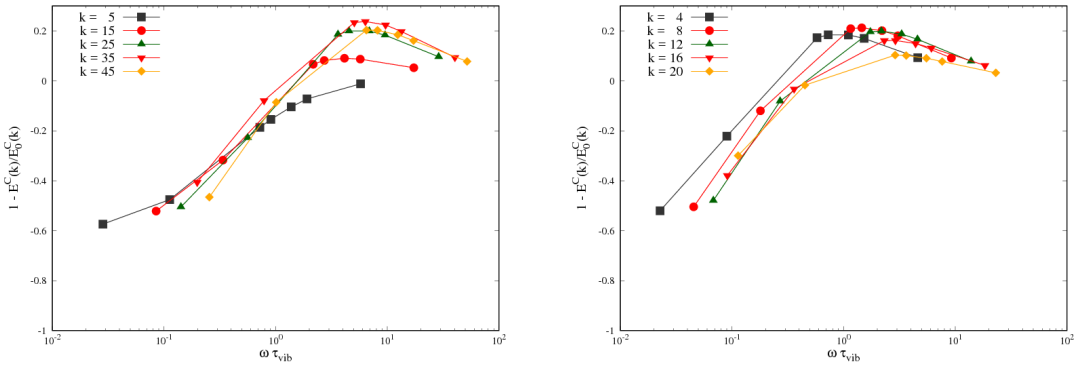

(a) Streamwise. (b) Spanwise.

Figure 6.17: Decomposed compressible energy spectra at specific non-dimensional wavenumbers in streamwise and spanwise directions at $t/\tau_\theta = 630$ and $M_c = 1.1$.

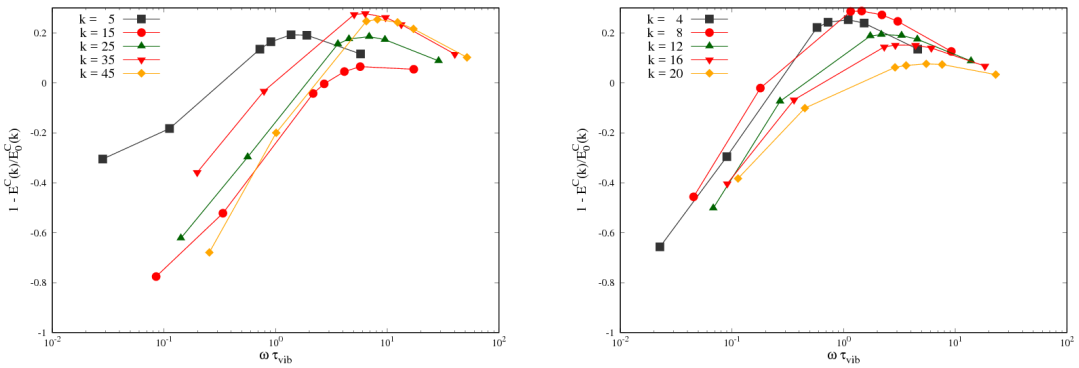

(a) Streamwise. (b) Spanwise.

Figure 6.18: Decomposed compressible energy spectra at specific non-dimensional wavenumbers in streamwise and spanwise directions at $t/\tau_\theta = 690$ and $M_c = 1.1$.

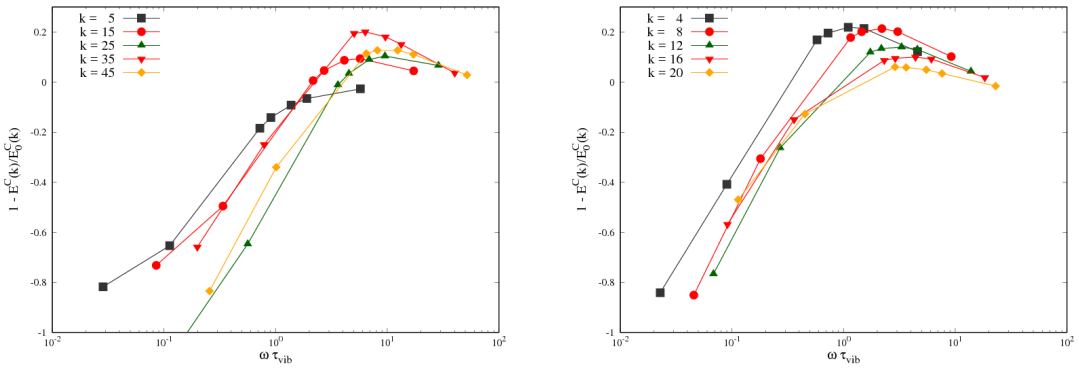

(a) Streamwise.

(b) Spanwise.

Figure 6.19: Decomposed compressible energy spectra at specific non-dimensional wavenumbers in streamwise and spanwise directions at $t/\tau_\theta = 780$ and $M_c = 1.1$.

So far, in both isotropic and shear flows, optimal damping has been observed regardless of the compressibility. In lower compressibility flows, the damping was small, but still observable. However, for $M_c = 0.7$, no damping is observed in the volume averaged dilatational fluctuations in Fig. 6.22. The volume averaging was calculated as discussed in the previous section, by averaging over the volume bounded by the momentum thickness. The dilatational fluctuations in all cases increase from the reference $Da_v = 0$ case. An initial increase proportional to Da_v of the fluctuations is followed by a reduction in time which is constant across all cases. This initial increase may be a function of the initialization, but has not been quantified. Regardless, the constant decay of dilatational fluctuations in time across all Da_v indicates very little absorption of compressible energy by the vibrational mode.

The decomposed spectra given in Fig. 6.23 provide further evidence of the importance of compressibility. Almost no observable effect on the compressible energy mode is observed by varying Da_v. The compressible energy represents a much smaller proportion of the total kinetic energy than in the $M_c = 1.1$ case.

Further comparison can be made by extracting wavenumbers and scaling the values in the same way we did in the previous section. These values are plotted for two times in Figs. 6.24 and 6.25, with the same axes as in Figs. 6.16 - 6.19. At both times shown, the

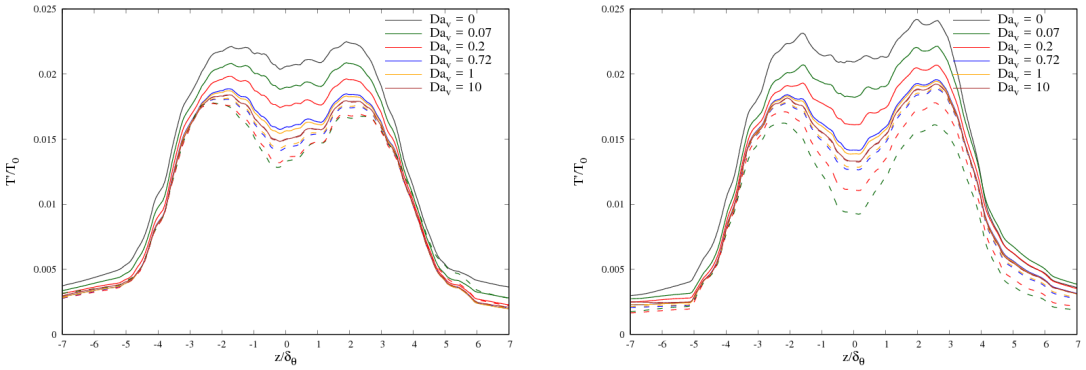

(a) $t/\tau_\theta = 510$. (b) $t/\tau_\theta = 630$.

Figure 6.20: Rms fluctuating temperature profiles at two different times for $M_c = 0.7$ and varying Da_v. Solid lines represent T', and dashed T'_v.

scaled spanwise spectra are virtually zero, meaning they are equivalent to the $Da_v = 0$ case. For the scaled streamwise spectra, the higher values of $\omega\tau_{vib}$ are unchanged from the reference case. These values represent slower relaxation rates (smaller Da_v). The lower values of $\omega\tau_{vib}$ and faster relaxation cases in the streamwise direction, and to a much smaller extent in the spanwise case, are modified. However, these wavenumbers are all modified by the same amount, consistent with the previous observations regarding the volume averaged fluctuating dilatation. Comparing these values with those obtained in the higher compressibility case makes clear that vibrational relaxation effects are highly dependent on compressibility.

6.6 Conclusion

Vibrational energy relaxation effects in temporally evolving turbulent shear layers were studied using DNS. Initial conditions were outlined, and numerical requirements, particularly the addition of constant numerical dissipation into the fluxes for the $M_c = 1.1$ case, were discussed. The tuning of the vibrational relaxation rate to the turbulent motion was examined by varying Da_v. The relevant turbulent time scale used to define Da_v was determined to be the large-structure acoustic time scale. Compressibility

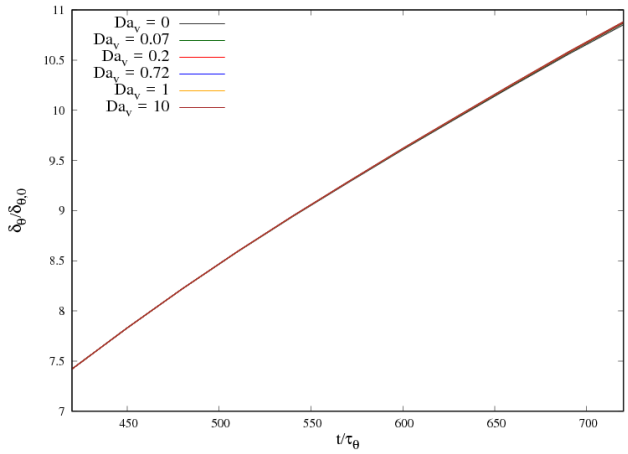

Figure 6.21: Time history of the evolution of momentum thickness for various Da_v and $M_c = 0.7$.

effects were also studied by considering two M_c cases, 0.7 and 1.1.

Comparisons are made with isotropic turbulence, with the primary exchange of energy between kinetic and vibrational modes occurring through the compressible modes. This was observed in averaged flow quantities and decomposed velocity spectra. Similar to the isotropic conclusions, the incompressible energies were much larger in magnitude than the compressible modes, and were unaffected by vibrational energy relaxation. This large disparity in energies yielded no effect on averaged turbulent kinetic energies or shear layer growth rates.

Optimal damping was defined by volume averaging quantities in the turbulent core bounded by the momentum thickness. Damping of acoustic fluctuations and shifts in peak values across Da_v cases can adversely influence interpretations of optimal damping. The gas was optimally damped when the vibrational relaxation rate was on the order of the large-scale acoustic rate, and is consistent with the tuning parameter in isotropic turbulent simulations. However, the clear wavenumber specific damping observed in isotropic flows was not observed in turbulent shear flows. The compressible spectra were altered by Da_v, but not as significantly. An attempt at collapsing the peaks in a

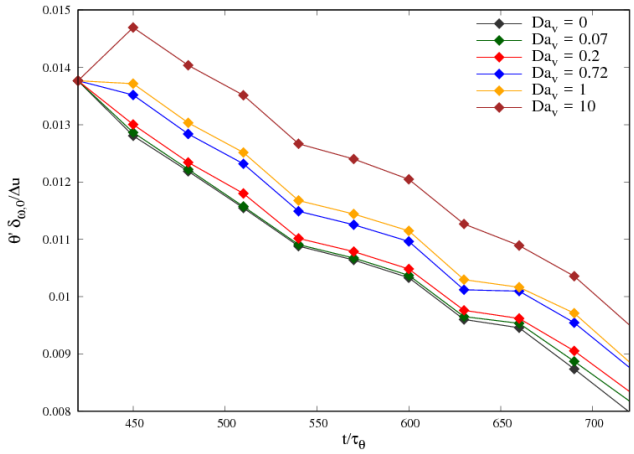

Figure 6.22: Evolution of fluctuating dilatation averaged in volume bounded by δ_θ in time, for various Da_v and $M_c = 0.7$.

similar way to the isotropic flows was mostly inconclusive. The peaks in compressible energy damping at a given wave number were near $\omega\tau_{vib}$ of one, and were moderately collapsed for the streamwise direction. The spanwise direction, while the peaks were also order $\omega\tau_{vib}$ of one, displayed a trend with increasing wavenumber.

The effects of compressibility were evaluated by considering two M_c. The lower compressible $M_c = 0.7$ was virtually unaffected by vibrational energy relaxation. Dilatational fluctuations were not damped, and the compressible energy was revealed to be significantly lower than the incompressible energy. These effects highlight the compressible coupling of the interaction between turbulent flows and vibrational energy relaxation, and is consistent with the conclusions from isotropic turbulent flows.

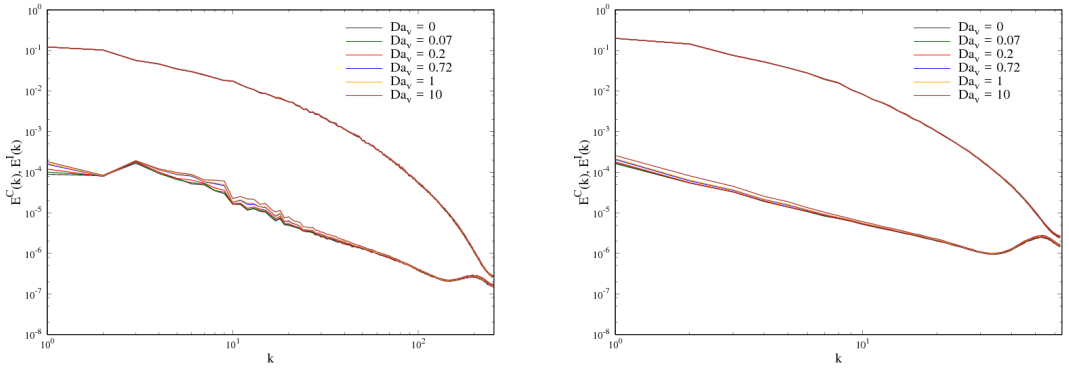

(a) Streamwise Spectra. (b) Spanwise Spectra.

Figure 6.23: Decomposed kinetic energy spectra in streamwise and spanwise directions at $t/\tau_\theta = 630$ for $M_c = 0.7$.

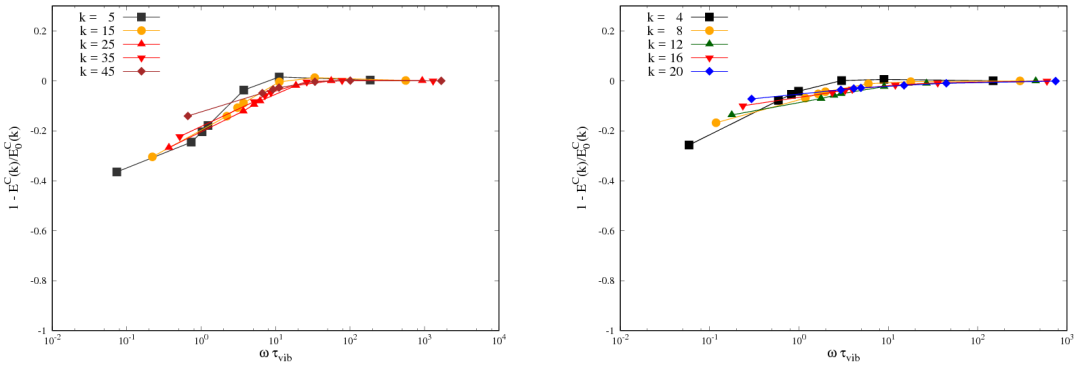

(a) Streamwise. (b) Spanwise.

Figure 6.24: Decomposed compressible energy spectra at specific non-dimensional wavenumbers in streamwise and spanwise directions at $t/\tau_\theta = 510$ and $M_c = 0.7$.

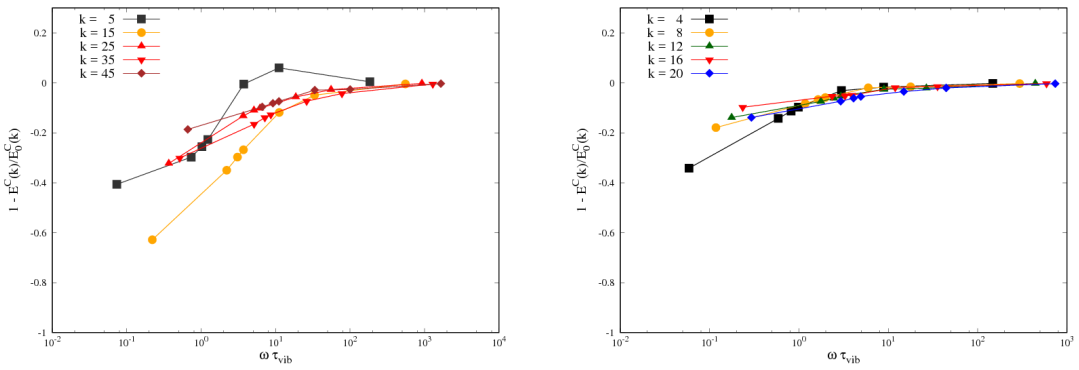

(a) Streamwise.

(b) Spanwise.

Figure 6.25: Decomposed compressible energy spectra at specific non-dimensional wavenumbers in streamwise and spanwise directions at $t/\tau_\theta = 630$ and $M_c = 0.7$.

Chapter 7

Summary and Conclusions

In this thesis, the effects of vibrational energy relaxation on turbulent flows are studied. Fundamental turbulent flows were considered to gain an understanding of the energy exchange mechanisms, and how the vibrational relaxation rate tunes to the turbulent flow. Here, tuning occurs when the turbulent fluctuations are optimally suppressed. The flows were compressible isotropic turbulence, and temporally evolving shear layers. A vibrational Dahmköhler number was defined using a turbulent time scale and the vibrational relaxation time. For both flows, the vibrational relaxation rate was tuned to the large-scale acoustic rate of the turbulence.

In the first part of this thesis, the governing equations, assumptions, and models were outlined. The flows in this work used a single-species formulation with a finite-rate conservation equation for vibrational energy. Vibrational energy is modelled using a simple harmonic oscillator assumption, and the transfer of energy is governed by a Landau-Teller form. The finite-volume methodology is used, with high-order convective fluxes and explicit time integration necessary for the simulations in this work. High-fidelity direct numerical simulations (DNS) were necessary to gain a fundamental understanding of the flow physics. No turbulent modelling is used, and all length and time scales are resolved.

A brief discussion on the properties of acoustic damping by internal energy relaxation is then presented in chapter 4. The conclusions help lay the foundation for understanding how energy relaxation effects turbulent flows. Theory has shown that acoustic waves are optimally damped when the frequency of the wave is on the order of the inverse

relaxation time. The ability of a gas to absorb acoustic energy is dependent on how much energy can be transferred and stored. Damping also requires excitation of the energy mode. These results are verified by DNS of acoustic wave propagation. DNS results are also used to demonstrate the physics of acoustic wave propagation.

The remaining chapters of the thesis present the results of the interaction between turbulent flows and vibrational energy relaxation. Compressible isotropic turbulence results are presented showing the energy exchange mechanisms and how the vibrational relaxation rate tunes to the turbulent motion. Vibrational energy relaxation has a damping effect on turbulent flow quantities. However, very little effect on the turbulent kinetic energy was observed. This was supported by decomposing the velocity field into compressible and incompressible components. The incompressible energy is unaffected by vibrational energy, and is significantly greater in magnitude than the compressible component. This energy disparity results in a weak effect on turbulent kinetic energy by vibrational energy relaxation.

The results of the compressible isotropic turbulent study were generalized to a more complex flow by considering temporally evolving shear layers. In these cases, the temperature fluctuations were damped in a similar manned to the isotropic fluctuations. The damping was greatest near the center of the shear layer, where the turbulence is the most intense. Dilatational fluctuations were also moderately damped, but showed significant increase as the relaxation rate increased. This significant increase was not observed in isotropic flows, where all dilatational fluctuations were damped from the reference case.

In both sets of turbulent flows, the effects of compressibility were examined by varying the relevant Mach number. The effect of vibrational energy on turbulent flow was observed to be strongly dependent on the compressibility of the flow. Additionally, the compressible energy spectra revealed that the vibrational energy is coupled to the turbulence through the acoustic modes. In isotropic flows, wavenumber specific damping was shown when the vibrational relaxation rate was similar to the acoustic frequency. This was less obvious in the shear results.

The turbulent flows considered in this work were shown to be tuned to the vibrational relaxation rate when the relaxation time was on the order of the large scale acoustic motion. For isotropic turbulence, this was defined using the integral length scale and

the acoustic wave speed, and for shear turbulence the momentum thickness was the relevant length scale. While these effects are weak on the turbulence, temperature fluctuations and specific portions of the compressible energy spectra can be damped when the relaxation rate is tuned to the turbulent flow. This tuning has potential use in flow control, such as modifying a turbulent boundary layers thermal properties by gas injection.

In the simulations considered in this work, the flows were initialized in thermal equilibrium. Previous studies[4] have shown that in chemically reacting flows, heat release can strongly effect the turbulence. These effects are strongest when the compressible energy of the flow is of the same order or greater than the incompressible energy. Significant thermal nonequilibrium, where the vibrational and translational-rotational temperatures are vastly different, can have similar effects to heat release in chemically reacting flows. This occurs as significant amounts of energy are released or transferred from the vibrational mode. The effects of these vibrationally hot or cold flows on turbulence is a potential area for future research. Understanding and quantifying how these effects impact turbulent motion is relevant to flow control.

References

[1] T. J. Horvath, B. M. Tomek, K. T. Berger, S. C. Splinter, J. N. Zalameda, P. W. Krasa, S. Tack, R. J. Schwartz, D. M. Gibson, and A. Tietjen. The hythirm project: Flight thermography of the space shuttle during hypersonic re-entry. January 2010.

[2] John D. Anderson Jr. *Hypersonic and High Temperature Gas Dynamics*. McGraw-Hill, Inc., 1989.

[3] J. F. Clarke and M. McChesney. *The Dynamics of Real Gases*. Butterworths, 1964.

[4] M. Pino Martín and G. V. Candler. Effect of chemical reactions on decaying isotropic turbulence. *Physics of Fluids*, 10(7):1715–1724, 1998.

[5] Philippe H Adam and Hans G Hornung. Enthalpy effects on hypervelocity boundary-layer transition: ground test and flight data. *Journal of Spacecraft and Rockets*, 34:614–619, 1997.

[6] Ivett A Leyva, Stuart Laurence, A War-Kei Beierholm, Hans G Hornung, Ross Wagnild, and Graham Candler. Transition delay in hypervelocity boundary layers by means of co2/acoustic instability interactions. January 2009.

[7] Keisuke Fujii and Hans G Hornung. Experimental investigation of high-enthalpy effects on attachment-line boundary-layer transition. *AIAA journal*, 41(7):1282–1291, 2003.

[8] R. Wagnild and G. V. Candler. Computational verification of acoustic damping in high-enthalpy environments. *AIAA Journal*, 52(11):2615–2618, 2014.

[9] A. I. Osipov, A. V. Uvarov, and N. A. Vinnichenko. Influence of the initial vibrationally nonequilibrium state of a medium on the structure of von karman vortex street. *Physics of Fluids*, 18(10), 2006.

[10] Diego A. Donzis and Agustin F. Maqui. Statistically steady states of forced isotropic turbulence in thermal equilibrium and non-equilibrium. *Journal of Fluid Mechanics*, 797:181–200, 2016.

[11] Lian Duan and M. Pino Martín. Effect of finite-rate chemical reactions on turbulence in hypersonic turbulent boundary layers. January 2009.

[12] Lian Duan and M. Pino Martín. Assessment of turbulence-chemistry interaction in hypersonic turbulent boundary layers. *AIAA Journal*, 49(1):172–184, 2011.

[13] Lian Duan and M. Pino Martín. Study of turbulence-chemistry interaction in hypersonic turbulent boundary layers. June 2011.

[14] T. J. Fuller. *Experimental Analysis of the Effect of Vibrational Non-Equilibrium on the Decay of Grid-Generated Turbulence*. PhD thesis, Texas A&M University, August 2009.

[15] T. J. Fuller, Aandrea Hsu, Rodney D. W. Bowersox, and Simon W. North. The effect of vibrational non-equilibrium on the decay of grid generated turbulence. January 2009.

[16] Timothy J. Fuller, Andrea G. Hsu, Rodrigo Sanchez-Gonzalez, Jacob C. Dean, Simon W. North, and Rodney D. W. Bowersox. Radiofrequency plasma stabilization of a low-reynolds-number channel flow. *Journal of Fluid Mechanics*, 748:663–691, 2014.

[17] K. Fujii and H. G. Hornung. A procedure to estimate the absorption rate of sound propagating through high temperature gas. Technical report, GALCIT TR FM 2001-004, California Institute of Technology, Pasadena, CA, August 2001.

[18] Ross Martin Wagnild. *High Enthalpy Effects on Two Boundary Layer Disturbances in Supersonic and Hypersonic Flow*. PhD thesis, University of Minnesota, May 2012.

[19] W. G. Vincenti and C. H. Kruger. *Introduction to Physical Gas Dynamics*. Krieger Publishing Company, 1982.

[20] Graham V Candler, Heath B Johnson, Ioannis Nompelis, Vladimyr M Gidzak, Pramod K Subbareddy, and Michael Barnhardt. Development of the us3d code for advanced compressible and reacting flow simulations. January 2015.

[21] F. G. Blottner, M. Johnson, and M. Ellis. Chemically reacting viscous flow program for multi-component gas mixtures. Sc-rr-70-754, Sandia Labs., Albuquerque, NM, 1971.

[22] L Landau and E Teller. Theory of sound dispersion. *Physikalische Zeitschrift der Sowjeturtion*, 10:34, 1936.

[23] R. C. Millikan and D. R. White. Systematics of vibrational relaxation. *Journal of Chemical Physics*, 39(12):3209–3213, 1963.

[24] C. Park. *Nonequilibrium Hypersonic Aerodynamics*. Wiley, 1990.

[25] M. Camac. CO2 relaxation processes in shock waves. In J. G. Hall, editor, *Fundamental Phenomena in Hypersonic Flow*, pages 195–215. Cornell University Press, Ithaca, NY, 1966.

[26] Robert W MacCormack and Graham V Candler. The solution of the navier-stokes equations using gauss-seidel line relaxation. *Computers & fluids*, 17(1):135–150, 1989.

[27] F. Ducros, V. Ferrand, F. Nicoud, C. Weber, D. Darracq, C. Gacherieu, and T. Poinsot. Large-eddy simulation of the shock/turbulence interaction. *Journal of Computational Physics*, 152:517–549, 1999.

[28] Pramod K. Subbareddy and Graham V. Candler. A fully discrete, kinetic energy consistent finite-volume scheme for compressible flows. *Journal of Computational Physics*, 228:1347–1364, 2009.

[29] Sigal Gottlieb and Chi-Wang Shu. Total variation diminishing runge-kutta schemes. *Mathematics of Computation*, 67(221):73–85, 1998.

[30] JS Jewell, IA Leyva, Nicholaus J Parziale, and Joseph E Shepherd. Effect of gas injection on transition in hypervelocity boundary layers. pages 735–740. Springer, Berlin, Heidelberg, 2012.

[31] MR Malik and EC Anderson. Real gas effects on hypersonic boundary-layer stability. *Physics of Fluids A: Fluid Dynamics*, 3:803–821, 1991.

[32] Heath B Johnson, Trevor G Seipp, and Graham V Candler. Numerical study of hypersonic reacting boundary layer transition on cones. *Physics of Fluids*, 10:2676–2685, 1998.

[33] CS Wang Chang and GE Uhlenbeck. Transport phenomena in polyatomic molecules. *University of Michigan Publication, CM-661*, 1951.

[34] L Monchick, KS Yun, and EA Mason. Formal kinetic theory of transport phenomena in polyatomic gas mixtures. *The Journal of Chemical Physics*, 39(3):654–669, 1963.

[35] Michael James Lighthill. Viscosity effects in sound waves of finite amplitude. In G.K. Batchelor and R.M. Davies, editors, *Surveys in mechanics*, pages 250–351. Cambridge University Press, 1956.

[36] W. E. Meador, G. A. Miner, and L. W. Townsend. Bulk viscosity as a relaxation parameter: Fact or fiction? *Physics of Fluids*, 8(1), 1996.

[37] P Balakumar. Receptivity of a supersonic boundary layer to acoustic disturbances. *AIAA journal*, 47, 2009.

[38] Robert Sugden Rogallo. Numerical experiments in homogeneous turbulence. Tech. rep. tm-81315, NASA, 1981.

[39] J. R. Ristorcelli and G. A. Blaisdell. Consistent initial conditions for the dns of compressible turbulence. *Physics of Fluids*, 9(4), 1997.

[40] S Tavoularis, JC Bennett, and S Corrsin. Velocity-derivative skewness in small reynolds number, nearly isotropic turbulence. *Journal of Fluid Mechanics*, 88(1):63–69, 1978.

[41] Steven A Orszag and GS Patterson Jr. Numerical simulation of three-dimensional homogeneous isotropic turbulence. *Physical Review Letters*, 28(2):76, 1972.

[42] Ravi Samtaney, D. I. Pullin, and Branko Kosović. Direct numerical simulation of decaying compressible turbulence and shocklet statistics. *Physics of Fluids*, 13(5):1415–1430, 2001.

[43] J. E. Moyal. The spectra of turbulence in a compressible fluid; eddy turbulence and random noise. *Mathematical Proceedings of the Cambridge Philosophical Society*, 42(02):329–344, 1952.

[44] C. Pantano and S. Sarkar. A study of compressibility effects in the high-speed turbulent shear layer using direct simulation. *Journal of Fluid Mechanics*, 451:329–371, 2002.

[45] DW Bogdanoff. Compressibility effects in turbulent shear layers. *AIAA journal*, 21(6):926–927, 1983.

[46] Dimitri Papamoschou and Anatol Roshko. The compressible turbulent shear layer: an experimental study. *Journal of fluid Mechanics*, 197:453–477, 1988.

[47] Gordon Erlebacher, MY Hussaini, HO Kreiss, and S Sarkar. The analysis and simulation of compressible turbulence. *Theoretical and Computational Fluid Dynamics*, 2:73–95, 1990.

[48] GS Elliott and M Samimy. Compressibility effects in free shear layers. *Physics of Fluids A: Fluid Dynamics*, 2:1231–1240, 1990.

[49] S Barre, C Quine, and JP Dussauge. Compressibility effects on the structure of supersonic mixing layers: experimental results. *Journal of Fluid Mechanics*, 259:47–78, 1994.

[50] Albertus Willem Vreman, ND Sandham, and KH Luo. Compressible mixing layer growth rate and turbulence characteristics. *Journal of Fluid Mechanics*, 320:235–258, 1996.

[51] Jonathan B Freund, Sanjiva K Lele, and Parviz Moin. Compressibility effects in a turbulent annular mixing layer. part 1. turbulence and growth rate. *Journal of Fluid Mechanics*, 421:229–267, 2000.

[52] J. R. Ristorcelli. A pseudo-sound constitutive relationship for the dilatational covariances in compressible turbulence. *Journal of Fluid Mechanics*, 347:37–70, 1997.

[53] JR Debisschop and JP Bonnet. Mean and fluctuating velocity measurements in supersonic mixing layers. 1993.

[54] Mo Samimy and GS Elliott. Effects of compressibility on the characteristics of free shear layers. *AIAA journal*, 28:439–445, 1990.

[55] O Chambres, S Barre, and J Bonnet. Detailed turbulence characteristics of a highly compressible supersonic turbulent plane mixing layer. submitted, 1998.

[56] NT Clemens and MG Mungal. Large-scale structure and entrainment in the supersonic mixing layer. *Journal of Fluid Mechanics*, 284:171–216, 1995.

[57] JL Hall, PE Dimotakis, and H Rosemann. Experiments in nonreacting compressible shear layers. *AIAA journal*, 31:2247–2254, 1993.

[58] H Foysi and S Sarkar. The compressible mixing layer: an les study. *Theoretical and Computational Fluid Dynamics*, 24:565–588, 2010.

[59] Inga Mahle. *Direct and large-eddy simulation of inert and reacting compressible turbulent shear layers*. PhD thesis, Technische Universität München, 2007.

[60] Matteo Frigo and Steven G. Johnson. The design and implementation of FFTW3, 2005. Special issue on "Program Generation, Optimization, and Platform Adaptation".

[61] Satish Balay, Shrirang Abhyankar, Mark F. Adams, Jed Brown, Peter Brune, Kris Buschelman, Lisandro Dalcin, Victor Eijkhout, William D. Gropp, Dinesh Kaushik, Matthew G. Knepley, Dave A. May, Lois Curfman McInnes, Karl Rupp, Patrick Sanan, Barry F. Smith, Stefano Zampini, Hong Zhang, and Hong Zhang. PETSc users manual, 2017.

Appendix A

Compressible Isotropic Initial Conditions

A.1 Incompressible Velocities

Velocity fuctuations are obtained from a given energy spectrum with zero divergence are generated using the method developed by Rogallo[38]. The velocity components are calculated in frequency space by

$$\begin{aligned} \hat{u} &= \frac{\alpha k k_2 + \beta k_1 k_3}{k\sqrt{k_1 k_1 + k_2 k_2}}, \\ \hat{v} &= \frac{\beta k_2 k_3 - \alpha k k_1}{k\sqrt{k_1 k_1 + k_2 k_2}}, \\ \hat{w} &= -\frac{\beta\sqrt{(k_1 k_1 + k_2 k_2)}}{k}, \end{aligned} \tag{A.1}$$

where k is the magnitude of the wave vector, and α and β are defined as

$$\begin{aligned} \alpha &= \sqrt{\frac{E}{2\pi k^2}}\exp(i\theta_1)\cos(\phi), \\ \beta &= \sqrt{\frac{E}{2\pi k^2}}\exp(i\theta_2)\sin(\phi). \end{aligned} \tag{A.2}$$

In the definitions above, E is the energy obtained from the given spectrum, and θ_1, θ_2, and ϕ are random phases. For $k_1 k_1 + k_2 k_2 = 0$, $\hat{u} = \alpha$, $\hat{v} = \beta$, and $\hat{w} = 0$. The mean is

set to zero, and symmetry is imposed to obtain an entirely real field when transforming to physical space.

A.2 Thermodynamic Fluctuations

Thermodynamic fluctuations are calculated using the methodology developed by Ristorcelli and Blaisdell[39]. The general procedure is given here; details on the derivation can be found in Riscorcelli and Blaisdell[39] and Ristorcelli[52]. The non-dimensional thermodynamic fluctuations are calculated by first relating the fluctuating pressure field to the velocity field in frequency space.

$$\hat{p}_1 = -\frac{k_i k_j}{k^2}\hat{u}_i\hat{u}_j \tag{A.3}$$

In deriving this equation, an assumption was made that the incompressible pressure fluctuations dominate the acoustic pressure fluctuations. This assumption requires low M_t; in the applications used here, this limit was found to be around $M_t \sim 0.55$.

The pressure fluctuations are transformed to physical space, the density fluctuations are found from

$$\rho_1 = \frac{1}{\gamma}p_1. \tag{A.4}$$

The temperature fluctuations are then calculated using

$$T_1 = \frac{\gamma - 1}{\gamma}p_1. \tag{A.5}$$

The dimensional thermodynamic fluctuations are then related by, for example,

$$p = P_0(1 + \gamma M_t^2 p_1) \tag{A.6}$$

Dimensional values of density are obtained using this same form. Rather than compute the fluctuating temperatures in Eq. A.5, the dimensional temperatures are simply obtained from the ideal gas law after the pressure and densitiy are calculated.

A.3 Compressible Velocities

A compressible component of velocity is added to the incompressible velocity computed from Eq. A.1. The methodology used is also given by Riscorcelli an Blaisdell[39]. The non-dimensional dilatation is related to the pressure and velocity field in frequency space using

$$-\gamma \hat{d} = \hat{p}_{1,t} + \hat{v}_k \hat{p}_{1,k}. \tag{A.7}$$

The time derivative of the fluctuating pressure, $\hat{p}_{1,t}$, is obtained from

$$\hat{p}_{1,t} = \frac{2}{k^2}[(\hat{v}_k \hat{v}_{i,k} + \hat{p}_{1,i})\hat{v}_j]k_i k_j. \tag{A.8}$$

The dilatational velocity is then computed as

$$\hat{w}_j = -i\left(\frac{k_j}{k^2}\right)\hat{d}. \tag{A.9}$$

The full velocity field is obtained by adding the dilatational and incompressible velocities together.

Appendix B

Compressible Temporal Shear Initial Conditions

B.1 Incompressible Velocities

Incompressible velocities for the shear layer are initialized using the following methodology. The initial mean velocity field is set to

$$\overline{u}(z) = \frac{\Delta u}{2} \tanh\left(\frac{z}{2\delta_\theta}\right), \quad \overline{v} = \overline{w} = 0. \tag{B.1}$$

The mean velocity field is incompressible, verified by evaluating $\nabla \cdot \overline{u_i} = 0$.

Velocity fluctuations are obtained by generating random numbers in a triply periodic cube. The random numbers are set to have zero mean and a uniform distribution. These numbers are transformed to frequency space, where an isotropic energy distribution is imposed from

$$E(k) = \left(\frac{k}{k_0}\right)^4 \exp\left[-2\left(\frac{k}{k_0}\right)^2\right] \tag{B.2}$$

This energy spectrum is imposed on the field in frequency space by

$$\hat{u}_i^{iso} = \hat{u}_i^{ran} \sqrt{\frac{E(k)}{E^{ran}(k)}}, \tag{B.3}$$

where the superscript ran refers to the random field quantities.

The extent of the fluctuations are limited to the shear layer using a shape function in physical space. An exponential decay of the form,

$$f(z) = \exp\left(-\frac{z}{2\delta_\theta}\right), \tag{B.4}$$

is used to limit the vorticity fluctuations,

$$\omega_i = \omega_i^{iso} f(z). \tag{B.5}$$

By limiting the fluctuations with an exponential decay, compressibility is added to the field. The compressible component of the velocity is removed by decomposing the field with a Helmholtz decomposition which solves three Poisson equations. This method of velocity decomposition is described in Appendix C. Eighth-order methods are used to calculate the incompressible velocity field. The incompressible velocity fluctuations are then added to the mean field to obtain the full incompressible velocity field.

B.2 Thermodynamics

The thermodynamic quantities are linked to the incompressible velocity field through the Poisson equation,

$$-\nabla p' = \frac{\partial^2 u_i u_j}{\partial x_i \partial x_j}. \tag{B.6}$$

The Poisson equation for pressure is solved using the same methodology provided in Appendix C.3.1. The pressure fluctuations are then added to the mean pressure field.

The density field is set through the isentropic flow equation,

$$\rho = \overline{\rho}\left(\frac{p}{p_0}\right)^{1/\gamma}. \tag{B.7}$$

The temperature field is found from the ideal gas law.

B.3 Validation

The initial conditions and numerics were validated using data from Pantano and Sarkar[44]. Results were obtained using US3D and perfect gas air, with the same solution methodology and flow domain presented in Chapter 6. Additional comparisons of the momentum thickness growth rate are given in Fig. B.1[53, 54, 55, 46, 56, 57, 58, 59]. Figure B.1 also shows the 'Langley Experimental Curve,' obtained from compiling several experiments of air shear layers. The experimental growth-rates may be modified by density ratio effects, and these effects are usually attributed to differences in numerical and experimental results[44]. US3D simulations compare well with both the data from Pantano and Sarkar and the Langley experimental curve across all M_c. The difference between US3D and Pantano and Sarkar for $M_c = 0.7$ is most likely due to different domain sizes; the simulation used for this case was twice the size of the domain used by Pantano and Sarkar.

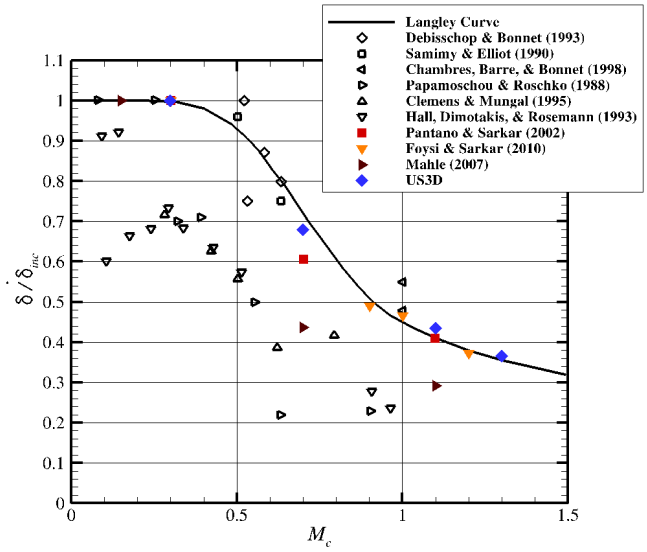

Figure B.1: Comparison of momentum thickness growth rate from simulations using US3D (blue diamonds) with the Langley Curve (solid line), experimental values (open symbols), and DNS values (closed symbols). The growth rate is normalized using the incompressible growth rate.

Appendix C

Velocity Decomposition

C.1 Helmholtz Decomposition

The interaction of internal energy modes with kinetic energy modes is studied by decomposing the velocity field. This decomposition is also used to remove the compressible component of the velocity field for the initialization of shear flows described in Appendix B. A Helmholtz decomposition is used to decompose the kinetic energy into incompressible (solenoidal) and compressible (dilatational) velocities. The compressible component, u^C, is curl-free and contains compressions and expansions. The incompressible component, u^I is the remaining content of the kinetic energy mode, such as vortical motion, and is divergence-free. Kinetic energy spectra of each component can then be computed to examine the broadband effects of relaxation on turbulence.

$$\nabla \times u^C = 0 \tag{C.1}$$

$$\nabla \cdot u^I = 0 \tag{C.2}$$

The Helmholtz decomposition is computed using two separate methods. Moyal[43] introduced a decomposition of the velocity field in Fourier space which is equivalent to a Helmholtz decomposition. While this method gives spectral accuracy in the decomposition, periodic boundary conditions are also requires in each direction. For the compressible isotropic simulations studied in Chapter 5, this condition is satisfied. However,

the mixing layer simulations in Chapter 6 have non-periodic directions, and therefore cannot use the spectral method. The second method uses Poisson equations to decompose the velocity into incompressible and compressible components. Both methods are described below, and comments are made on order of accuracy requirements when using the Poisson equations.

C.2 Spectral Equations

Moyal[43] introduced a decomposition of the velocity field in wave space in his study on isotropic flows. This decomposition is equivalent to a Helmholtz decomposition. In wave space, the velocity can be described with a component parallel to the wave vector, and a component which is perpendicular. Transforming Eq. C.2 to wave space, $k_i \hat{u}_i^I = 0$, requires that the perpendicular component be the incompressible velocity. This leaves the parallel component as the compressible velocity. The equations used for the spectral decomposition of velocity are given below. Given a Fourier transformation of velocity (the FFTW package is used in this work[60]), the decomposition is extremely simple and highly accurate.

$$\hat{u}_i^C = \frac{k_j \hat{u}_j}{k^2} k_i \tag{C.3}$$

$$\hat{u}_i^I = \hat{u}_i - \hat{u}_i^C \tag{C.4}$$

C.3 Poisson Equations

While the method described in the previous section is simple and accurate, periodic boundary conditions in every direction are required. When non-periodic boundary conditions are used, such as in the shear flows considered in this work, a different method is required. The decomposition method used in this work for these cases solves Poisson equations to obtain the incompressible velocity. The Poisson equations are derived by first recalling the following vector identity:

$$\nabla(\nabla \times \vec{A}) = \nabla(\nabla \cdot \vec{A}) - \nabla^2 \vec{A} \tag{C.5}$$

The first term on the right hand side contains the divergence of A. Applying this equation to the velocity field and setting the divergence to zero, the Poisson equations for the incompressible component of velocity are:

$$\nabla(\nabla \times \vec{u}) = -\nabla^2 \vec{u}^I \tag{C.6}$$

This formulation actually represents three independent Poisson equations for u^I. The compressible component of the velocity is then found by subtracting $\vec{u}^I$ from $\vec{u}$.

$$\vec{u}^C = \vec{u} - \vec{u}^I \tag{C.7}$$

Alternatively, $\vec{u}^C$ could be obtained from C.5 by setting the curl to zero, and then computing $\vec{u}^I$ from Eq. C.7. However, the three equations for $\vec{u}^C$ are coupled through the divergence term and much more difficult to solve.

C.3.1 Numerics

Three separate Poisson equations are needed to calculate u^I. The solutions to these equations can be difficult and time consuming. Central-based finite-difference schemes are used to discretize each velocity component of Eq. C.6. Various orders of accuracy are evaluated, with the cell-centered data used in the scheme. The order of accuracy required to accurately decomposed the velocity to a desired level is covered in the next section. Periodic boundary conditions are applied in the two homogeneous directions. In the transverse direction, the sponge layer at the top and bottom of the domain is removed, and Neumann boundary conditions are used at $\pm L_z/2$. A single Dirichlet point was set at the bottom corner ($x = 0, y = L_y/2$) of the domain to anchor the solution. The value of the Dirichlet point was set to the velocity of the cell.

The Poisson discretized equations are solved in matrix form, using a parallel GMRes method contained within the PETSc library[61]. Using a GMRes method allowed for faster convergence times than standard iterative methods, such as Jacobi point relaxation or Gauss-Seidel. In most cases examined in this work, the three Poisson equations were solved simultaneously. Each solution used 96 cores, with approximately 10-20 minutes of wall-clock time to reach convergence.

C.3.2 Verification and Order of Accuracy

Verification of the method described above was performed using decompositions of isotropic turbulence from the spectral equations. The velocity field is obtained from a simulation with $Re_\lambda = 175$, $M_t = 0.5$, $Da_v = 8$. A case with vibrational relaxation was used to determine how well the method captured the change in shape of the spectra. The order of accuracy of the derivatives in Eq. C.6 and the Poisson solutions was also examined with 2nd, 4th, 6th, and 8th order central-based schemes. Figure C.1 shows the results of this verification and the comparison between order of accuracies.

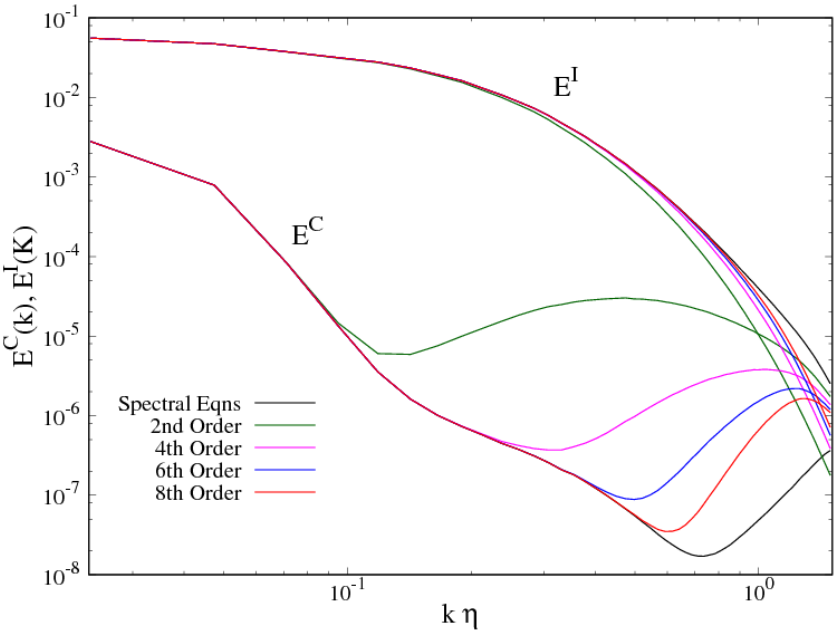

Figure C.1: The Poisson equations are solved using various order of accuracy central-based schemes and verified against the solution from the spectral equations. The velocity field is obtained from Isotropic turbulent simulation with vibrational relaxation ($Re_\lambda = 175$, $M_t = 0.5$, $Da_v = 8$).

As seen in Fig. C.1, the Poisson method does a reasonably good job of matching the spectral method, especially as the order of accuracy is increased. The incompressible component, with larger energetic content, is matched very well between all cases.

Some difference is observed at higher wave numbers, with the difference decreasing as order of accuracy increases. This is expected, as numerical error results in increased energy at the highest wavenumbers. Significant difference is seen in the compressible component for the second order method as the wavenumber increases. As the order of accuracy increases, the Poisson method matches the spectral method for higher and higher wavenumbers. The second and fourth order methods contain increased energy in regions where the shape of the compressible spectrum is changed, while the sixth and eighth order methods resolve this trend with acceptable accuracy. The computational cost between orders of accuracy is negligible; eighth order schemes are therefor used to solve the Poisson equations in this work.

Appendix D

Model Constants

D.1 CO_2 Properties

MW	44.0095
NVM	4
Blottner Coefficients	
A	-0.041372
B	1.3293
C	-15.016
$\theta_{v,m}$(K)	
Two Bending Modes	959.66
Symmetric Mode	1918.7
Asymetric Mode	3382.1
MW Constants	
A	36.5
B	-0.0193

Table D.1: Gas properties for CO_2. Note that CO_2 is a linear polyatomic molecule.

D.2 Vibrational Relaxation Rate Properties

D.2.1 Procedure to Modify Relaxation Rate

The vibrational relaxation times are varied by altering the constants in the Millikan and White (MW) semi-empirical curve fits (Eq. 2.21), and shown again,

$$\tau_m = \frac{1}{P} \exp[A_m(T^{-1/3} - B_m) - 18.42], \tag{D.1}$$

where the pressure is in atmospheric units, and m is the vibrational mode. All vibrational modes are assumed to relax at the same τ_m, so that the constants A_m and B_m are the same for each mode. This is the case for standard unmodified CO_2, and reduces the complexity of modifying τ_{vib} significantly.

The constants are modified by specifying a desired τ_{vib}, usually by providing a desired Da_v and corresponding definition. A range of A values are considered, usually $[-100 : 100]$, and B is calculated to match τ_{vib}. The constants are selected such that the distance, evaluated as,

$$D = (\frac{A}{A_0} - 1)^2 + (\frac{B}{B_0} - 1)^2 \tag{D.2}$$

is minimized. A_0 and B_0 are the original unmodified constants. The original constants are given in Table D.1, and the modified constants are provided below.

D.2.2 Modified Vibrational Relaxation Rate Constants

$M_t = 0.1$, $Re_\lambda = 72$		
Da_v	A	B
0	100.0	-1.0
1	51.4	-0.02092
7.2	36.5	-0.01930
10	34.0	-0.01903
20	28.6	-0.01873
30	25.4	-0.01870

$M_t = 0.3$, $Re_\lambda = 72$		
Da_v	A	B
0	100.0	-1.0
0.5	41.7	-0.01966
0.98	36.5	-0.01930
3.3	27.0	-0.01876
7	21.2	-0.01829
15	15.1	-0.01870

$M_t = 0.5$, $Re_\lambda = 72$		
Da_v	A	B
0	100.0	-1.0
0.125	43.9	-0.01996
0.25	36.5	-0.01930
0.5	33.3	-0.01896
1	27.9	-0.01862
2	22.4	-0.01868
4	16.9	-0.01879
8	11.4	-0.01899
16	5.9	-0.01958
32	0.5	-0.00753
64	-5.0	-0.01945

$M_t = 0.5$, $Re_\lambda = 175$		
Da_v	A	B
0	100.0	-1.0
0.1	52.7	-0.02109
0.5	40.6	-0.01982
0.86	36.5	-0.01930
2	30.0	-0.01866
4	24.5	-0.01873
8	19.0	-0.01883
16	13.5	-0.01902
32	8.0	-0.01947
64	2.6	-0.01694

Table D.2: Millikan and White modified constants for isotropic cases.

$M_c = 0.7$			$M_c = 1.1$		
Da_v	A	B	Da_v	A	B
0	100.0	-1.0	0	100.0	-1.0
0.004	65.5	-0.02334	0.13	36.5	-0.01930
0.07	44.9	-0.02011	0.38	27.7	-0.01874
0.2	36.5	-0.01930	0.53	25.1	-0.01852
0.6	27.8	-0.01876	0.8	21.7	-0.01860
0.7	26.3	-0.01888	1	19.9	-0.01828
1	23.7	-0.01860	6.35	4.7	-0.01927
10	5.3	-0.01842	25	-6.4	-0.02002

Table D.3: Millikan and White modified constants for shear cases.